

# **Regions of Massive Star Formation – Structure and Stellar Populations**

**Dissertation**

**zur Erlangung des akademischen Grades  
*doctor rerum naturalium* (Dr. rer. nat.)**

**vorgelegt dem Rat der Physikalisch–Astronomischen Fakultät  
der Friedrich–Schiller–Universität Jena**

**von Diplom–Physiker *Hendrik Linz*  
geboren am 10. Januar 1975 in Suhl**

## **Gutachter**

**1. Prof. Dr. rer. nat. habil. Thomas Henning**

(Max-Planck-Institut für Astronomie Heidelberg & Friedrich-Schiller-Universität Jena)

**2. Prof. Dr. rer. nat. Peter Hofner**

(New Mexico Tech University & National Radio Astronomy Observatory Socorro)

**3. Prof. Dr. rer. nat. Artie Hatzes**

(Thüringer Landessternwarte Tautenburg & Friedrich-Schiller-Universität Jena)

**Tag der letzten Rigorosumsprüfung : 25. Juni 2005**

**Tag der öffentlichen Verteidigung : 5. Juli 2005**

## Zusammenfassung der Dissertationsschrift

# Entstehungsgebiete massereicher Sterne: Struktur und stellare Populationen

vorgelegt von Diplom-Physiker Hendrik Linz

Diese Dissertation beschäftigt sich mit der Untersuchung massereicher Sternentstehungsgebiete. Ziel ist es vor allem, die jüngsten massereichen Objekte in diesen Gebieten ausfindig zu machen und umfassend zu charakterisieren. Grundlage dieses Unterfangens sind Beobachtungsdaten im nahen ( $1 - 3 \mu\text{m}$  Wellenlänge) und thermischen ( $3 - 20 \mu\text{m}$  Wellenlänge) Infrarot. Diese Daten wurden vornehmlich an Teleskopen der Europäischen Südsternwarte (ESO) in Chile erhalten. Die Quellen für detaillierte Studien wurden einer Liste von sogenannten massereichen protostellaren Objekten (HMPOs) entnommen, für die vor kurzem die Existenz von 44-GHz Methanol-Masern nachgewiesen werden konnte und die im Rahmen einer internationalen Kooperation schließlich mit dem Radiointerferometer VLA bei einer Wellenlänge von 7 mm beobachtet werden sollen. Die beiden ausgewählten Regionen weisen jeweils eine interessante Besonderheit auf: Die Existenz eines extrem kollimierten Radio-Jets im Falle von GGD 27 sowie die anscheinende Assoziation eines sogenannten "Heißen Molekülwolkenkerns" mit Nah-Infrarotstrahlung im Falle von G9.62+0.19. Unsere Beobachtungen ergeben folgende Schlüsse für diese Objekte:

Unsere hochauflösenden Nahinfrarot-Beobachtungen mit deutlich besserer räumlicher Auflösung als in der bisherigen Literatur vermerkt, enthüllen eine Substruktur von mindestens drei Quellen im Bereich des heißen Molekülwolkenkerns G9.62+0.19-F. Das hellste dieser Objekte stimmt positionsmäßig nicht mit der Zentralposition des heißen Kerns überein, im Gegensatz zu früheren Ergebnissen von Testi und Mitarbeitern (1998). Bei längeren Wellenlängen ( $\lambda \geq 3.8 \mu\text{m}$ ) findet man Emission eines vierten Objektes, welches das eigentliche Infrarot-Gegenstück des im Radiobereich sichtbaren Molekülwolkenkerns ist. Dieses Objekt ist identisch mit der schon bekannten kompakten Emission bei  $11.7 \mu\text{m}$ , was die Resultate von De Buizer und Mitarbeitern (2003, 2005) relativiert. Die Tatsache, daß dieser Molekülwolkenkern überhaupt im Infraroten sichtbar ist, läßt sich nach unserer Analyse durch das Wirken eines von G9.62+0.19-F ausgehenden molekularen Ausflusses erklären, der entlang der Sichtlinie zu uns das ursprünglich sehr dichte Material des heißen Kerns teilweise entfernt bzw. verdünnt hat.

Im Fall von GGD 27-ILL konnte dieses Zentralobjekt zum ersten Mal bei einer relativ kurzen Wellenlänge von 3.8 Mikrometern mit bisher nicht erreichbarer Detailschärfe abgebildet werden, wobei es Anzeichen für eine innere Struktur gibt. Die besondere Form des 8–13  $\mu\text{m}$  Spektrums des Zentralobjektes GGD 27-ILL und die erfolgreiche Angleichung eines speziellen synthetischen Staubmodells auf Basis der Arbeiten von Weingartner & Draine (2001) an diese Daten indiziert die Existenz eines beträchtlichen Anteils an relativ großen Staubteilchen ( $a \geq 0,25 \mu\text{m}$ ) im zirkumstellaren Material um GGD 27-ILL, solange keine fraktalen oder porösen Staubmodelle in Betracht gezogen werden.

Bei beiden Zentralobjekten (G9.62+0.19–F4 and GGD 27–ILL) kann eine auf einem sphärisch-symmetrischen Modell beruhende selbstkonsistente Strahlungstransport-Rechnung nicht alle Beobachtungsbefunde befriedigend reproduzieren. Eine abgeplattete, axialsymmetrische Materieverteilung ist in beiden Fällen zu erwarten.

Bei GGD 27–ILL existierten bereits Vermutungen in dieser Richtung. Unsere Beobachtungen im thermischen Infrarot sowie unseren hochaufgelösten VLA 7-mm Messungen lassen die Existenz einer zirkumstellaren Scheibe um GGD 27–ILL weiterhin zu. Allerdings wird der Durchmesser dieser Konfiguration weniger als 400 Astronomische Einheiten betragen.

Aus den Ergebnissen unserer umfassenden Infrarotbeobachtungen lassen sich weitreichende Schlußfolgerungen ziehen:

Die Struktur massereicher Sternentstehungsgebiete erscheint vor allem im Infraroten oft sehr komplex. Dies ist aber nicht nur durch die intrinsische Energieverteilung der eingebetteten jungen stellaren Objekte bestimmt. Vielmehr tragen auf den verschiedenen Größenskalen auch die Verteilung und die Asymmetrien des durch seine Extinktionswirkung offensichtlich werdenden zirkumstellaren Materials zu dieser Komplexität bei. Dies muß bei der Interpretation von Bildern und Flußdichte-Daten berücksichtigt werden.

Die Astrometrie der Infrarot-Beobachtungen massereicher Sternentstehungsgebiete kann einen entscheidenden Einfluß auf die Interpretation dieser Daten haben, v.a. wenn sie mit hochauflösenden interferometrischen Messungen in Einklang gebracht werden müssen. Eine ungenaue Astrometrie kann zu grundsätzlich falschen Aussagen über die Natur der gefundenen Objekte führen.

Die frühen Phasen bei der Entstehung massereicher Sterne, vor der Ausbildung eines ultrakompakten HII-Gebietes, sind entscheidend für die Ausbildung nicht-sphärischer Geometrien. Auf diese Stadien muß sich zukünftig die verstärkte Aufmerksamkeit richten.

Solange nicht besondere Geometrie- und Sichtlinienverhältnisse herrschen, sind diese frühen Stadien nicht im nahen Infrarot beobachtbar. Deshalb muß v.a. die in dieser Arbeit erfolgreich eingesetzte Methode der Beobachtungen im thermischen Infrarot weiter ausgebaut werden.

Als ergänzende Technik verspricht die Beobachtung der jungen massereichen Objekte mit dem VLA 7-mm-Interferometriesystem Erfolg. Auch zu diesem Ansatz hat diese Dissertation beigetragen. Erstmals konnte die Machbarkeit von interferometrischen VLA 7-mm-Beobachtungen mittels der Maser-Kreuzkalibrationsmethode unter Verwendung von 44-GHz Methanolmasern erfolgreich demonstriert werden. Diese Art der Kalibration interferometrischer Messungen wird bei zukünftigen Interferometrie-Projekten vor allem im Submillimeter-Bereich entscheidend an Bedeutung gewinnen.

*So erzählt man sich von Thales, er sei, während er sich mit dem Himmelsgewölbe beschäftigte und nach oben blickte, in einen Brunnen gefallen. Darüber habe ihn eine junge und hübsche thrakische Dienstmagd ausgelacht und gesagt, er wolle da mit aller Leidenschaft die Dinge am Himmel zu wissen bekommen, während ihm doch schon das, was ihm vor der Nase und den Füßen läge, verborgen bleibe.*

*(Platon, Theaitetos)*

*Am Himmel bescheid wissen, nicht aber auf der Erde, das erscheint als unauflösbare Gegensätzlichkeit. Erst spät empfahl Francis Bacon die methodische Weisheit, die Sterne doch im Spiegel jenes Brunnens zu betrachten, in den sonst der Astronom zu fallen droht. Man hat nun schon die ersten Spiegel mit Transportern in den Orbit geschossen, um atmosphärisch ungestört die Sterne zu erforschen. Dazu kann der Astronom zu Hause bleiben und auf die Bilder warten.*

*(Hans Blumenberg, Die Vollzähligkeit der Sterne)*

# Contents

<b>1</b>	<b>Introduction</b>	<b>1</b>
1.1	High-mass star formation	2
1.1.1	Specific problems in understanding massive star formation	2
1.1.2	Setting the stage	4
1.2	Goals of the presented work	6
<b>2</b>	<b>Source Selection and Observations</b>	<b>8</b>
2.1	Objects for detailed studies	8
2.1.1	G9.62+0.19	8
2.1.2	GGD 27	9
2.2	Infrared and Millimetre Telescopes and Cameras	11
2.2.1	J, H, and Ks band observations	11
2.2.2	Br $\gamma$ and H <sub>2</sub> observations and K narrow-band polarimetry	12
2.2.3	L' and nb_M band observations	12
2.2.4	N and Q band observations	13
2.2.5	1.2-mm continuum observations	14
2.3	Interferometry with the VLA 7-mm system	15
2.3.1	The VLA – A very short introduction	15
2.3.2	Our B-array observations	15
<b>3</b>	<b>G9.62+0.19 – An HMC puzzles the IR observers</b>	<b>17</b>
3.1	Near-infrared broad-band data	17
3.2	L' and nb_M band data	22
3.3	N and Q band data	23
3.4	H <sub>2</sub> and Br $\gamma$ narrow-band imaging data	25
3.5	K narrow-band imaging polarimetry	27
3.6	What is the nature of the IR objects in the HMC region?	31
3.6.1	Hints from the polarimetry	34
3.6.2	Ordinary stars within the HMC vicinity?	35
3.7	Comparison with other HMCs	37
3.8	Why can't we see the D and E components in the infrared?	38
3.9	Conclusions	41

<b>4</b>	<b>GGD 27 – A splendid IR reflection nebula with a pumping heart</b>	<b>43</b>
4.1	Infrared results . . . . .	44
4.1.1	K narrow-band imaging . . . . .	44
4.1.2	Thermal infrared imaging . . . . .	46
4.1.3	N-band spectrum . . . . .	50
4.2	Results of the VLA 7-mm imaging . . . . .	53
4.3	Additional sources in the GGD 27 vicinity . . . . .	57
4.3.1	The X-ray sources in GGD 27 and their IR counterparts . . . . .	57
4.3.2	New millimeter continuum clumps . . . . .	61
4.4	Discussion . . . . .	64
4.4.1	The central source . . . . .	64
4.4.2	A complex environment . . . . .	70
4.5	Conclusions . . . . .	71
<b>5</b>	<b>Sources for VLA-7mm observations</b>	<b>74</b>
5.1	Infrared colour criteria . . . . .	74
5.2	Molinari 45 – An exemplary case? . . . . .	77
<b>6</b>	<b>General Conclusions and Outlook</b>	<b>81</b>
	<b>Bibliography</b>	<b>84</b>
<b>A</b>	<b>NIR Astrometry for G9.62+0.19</b>	<b>97</b>
<b>B</b>	<b>Correct position of the compact MIR source in G9.62+0.19-F</b>	<b>99</b>
<b>C</b>	<b>MIR image restoration</b>	<b>101</b>
<b>D</b>	<b>Maser Cross Calibration for VLA data</b>	<b>103</b>
<b>E</b>	<b>Used Acronyms</b>	<b>105</b>
	<b>Thanksgiving</b>	<b>106</b>
	<b>Tabellarischer Lebenslauf</b>	<b>108</b>
	<b>Ehrenwörtliche Erklärungen</b>	<b>110</b>

# **Chapter 1**

## **Introduction**

Stars are the most obvious units of luminous matter in the universe, and some of them not too distant from our solar system can even be seen with the naked eye. However, in order to reveal the stars' secrets the contemporary astronomer tries to catch as much information as possible from these stars (mostly in form of photons of a large variety of wavelengths) and has to feed them into a whole conglomeration of sophisticated instruments. Such an approach is probably indispensable since mother nature is sometimes not generous with her answers, but has to be outwit to give them away.

One of the secrets is how stars form. For thousands of years stars were thought to be eternal entities. This was succeeded by the hypothesis that almost all stars had formed roughly at the same time in an era of chaos. It is a remarkable fact that the idea of recent and ongoing star formation is a concept that emerged only in the 20th century. It is generally agreed that (at least the present day) star formation occurs in dense condensations of molecular clouds. Such cores eventually collapse under the influence of gravity and form one or more so-called protostars in their centres that further accumulate mass from the surrounding envelope (e.g., Larson 2003 and references therein). During the process of accretion the formation of flattened axisymmetric structures (e.g., Terebey et al. 1984, Yorke & Bodenheimer 1999) and the generation of jets and outflows (e.g., Richer et al. 2000) are expected in general in order to transport excess angular momentum away from the forming star. In the case of low- and intermediate-mass star formation (for stars in the mass range between 0.1 – 8.10  $M_{\odot}$ ) there has been considerable progress over the last 25 years in understanding the related processes. These ideas were incorporated into a kind of standard model of (low-mass) star formation (Shu, Adams & Lizano 1987, André et al. 1993) that acts as the current paradigm. However, the model contains idealised assumptions and might just be a comfortable starting point to develop new ideas. In particular, during the last five year, several authors have tried to modify crucial aspects in order to bring the theory in accordance with the more realistic circumstances. This concerns for instance the general time scales for star formation (e.g., Elmegreen 2000, Hartmann 2002) or the role of binarity/multiplicity in star formation (see Zinnecker & Mathieu (2000) for a whole IAU Symposium devoted to this topic).



## 1.1 High-mass star formation

The formation process of massive stars ( $M > 8..10 M_{\odot}$ ) remains a key problem in stellar astrophysics. In the following we want to give some motivation why the investigation of massive star formation actually represents a distinct field of research, and we want to shortly outline the specifics of this branch of research. As we will see, the low-mass case often serves as a guideline along which one can emphasise the differences and peculiarities of massive star formation.

### 1.1.1 Specific problems in understanding massive star formation

**Challenges for the theoreticians :** One general problem is to decide about the global mode of massive star formation. What are the most important factors that rule the formation of high-mass stars (nurture or nature, see Bonnell et al. 2004)? Is the massive star's mass already determined by the mass in the collapsing molecular core, or do we have to take environmental processes like competitive accretion in cluster environments into account? In the first scenario, the stellar cluster environment is only of minor importance, and high-mass clumps in molecular clouds can lead directly to high-mass stars after the clumps have won their struggle against turbulent, thermal, or magnetic support (e.g., Padoan & Nordlund 2002, McKee & Tan 2003). In the other scenario, the star's mass is strongly influenced or even determined by interaction of the forming massive star with the surrounding stellar cluster. Here, the cluster stars compete for the gas reservoir, and this complex interaction is thought to explain the range and distribution of stellar masses (e.g., Bonnell et al. 2001a, 2001b, 2004).

In both cases, the massive star grows through accretion onto a protostellar core. However, in contrast to the formation of low-mass stars, the Kelvin-Helmholtz time scale,  $t_{\text{KH}} = GM_*^2/R_*L_*$ , for the onset of nuclear fusion is shorter than the accretion time scale,  $t_{\text{acc}} = M_*/\dot{M}_{\text{acc}}$ , in case of a massive protostar ( $M \geq 8..10 M_{\odot}$ )<sup>1</sup>. Therefore, such a star arrives at the Zero Age Main Sequence (ZAMS) of the Hertzsprung-Russell diagram and starts radiating with high luminosity while still deeply embedded in its accreting envelope. Thus, it is often argued that a further spherical mass build-up beyond  $\sim 10 M_{\odot}$  is hindered or even stopped due to the influence of the radiation pressure (e.g., Larson & Starrfield 1971, Wolfire & Cassinelli 1987), contrary to the obvious existence of stars with masses up to  $100 M_{\odot}$  (e.g., Kudritzki et al. 1992). A number of mechanisms has been proposed to circumvent this problem, among them:

- mass build-up through disk accretion (e.g., Yorke & Sonnhalter 2002),
- accretion with extremely large (e.g., Osorio et al. 1999, Nakano et al. 2000) or increasing (e.g., McLaughlin & Pudritz 1997, Behrend & Maeder 2001) infall rates,

or – as a completely different approach –

---

<sup>1</sup>This mass value where the time scale reversal occurs is often used to discriminate between low-mass and high-mass star formation (e.g., Cesaroni 2005)

- collisions of protostellar cores (Price & Podsiadlowski 1995) or coalescence of less massive stars in young and dense cluster environments (Bonnell et al. 1998, Stahler, Palla & Ho 2000, Bonnell & Bate 2002).

All these models make specific predictions which can in principle be tested observationally (for instance existence of accretion disks, relations in the infall–outflow dynamics, enhanced binarity/multiplicity).

**Challenges for the observers :** On the observational side, however, our gain of knowledge about young massive stars has been hampered in previous years mostly because of the lack of a sufficient number of high–resolution observations covering the early evolutionary stages of massive stars. When investigating the details of the formation of high–mass stars, the observer is faced with several complications.

First, sites of massive star formation are found, in average, at clearly larger distances from the Sun than the closest sites of low–mass star formation. In addition, massive stars mostly do not form isolated but often in clusters and associations whereby the forming stars show more intensive interaction with the natal environment which further increases the complexity of the problem. Thus, high resolution and sensitivity are not only accessories but are of pivotal importance in order to disentangle the typically crowded regions of massive star formation and to clarify the energetics and physical processes associated with them.

Second, the very deep embedding of very young massive stars within their natal dust and gas cocoon causes tens to hundreds of magnitudes of visual extinction. Hence, the direct detection of the central objects often lies beyond the limit of conventional, ground–based near–infrared (NIR,  $0.9 - 3 \mu\text{m}$ ) imaging techniques. The emission during these early phases of star formation (see Fig. 1.1) is expected to peak in the far–infrared (FIR,  $30 - 100 \mu\text{m}$ ), a wavelength range where the earth atmosphere is fully opaque. Thus, a severe “dilemma” of the present–day astronomer is that the existent FIR information has been obtained exclusively with small–aperture satellites (e.g., *IRAS*<sup>2</sup>, *ISO*<sup>3</sup>) and airborne (e.g., *KAO*<sup>4</sup>) missions, which provide only very low spatial resolution and only upper limits on the luminosity. Also the currently operating IR satellite *Spitzer* (85 cm aperture) is limited in this regard. The majority of high–resolution data, which allow to discern these close and deeply embedded massive YSOs (e.g., distinguish between Hot Molecular Cores and the adjacent UCHIRs, see next section), come from interferometric observations in the radio, i.e., only from the long–wave part of the spectral energy distribution.

This very brief survey of principle problems may already demonstrate that the requirements to study massive star formation are severe for both, the observer and the theoretician (Garay & Lizano 1999, Henning et al. 2002b).

---

<sup>2</sup>*InfraRed Astronomical Satellite*, 60 cm aperture, time of operation 01/1983 – 11/1983

<sup>3</sup>*Infrared Space Observatory*, 60 cm aperture, time of operation 11/1995 – 05/1998

<sup>4</sup>*Kuiper Airborne Observatory*, 91 cm aperture, time of operation 1975 – 1995

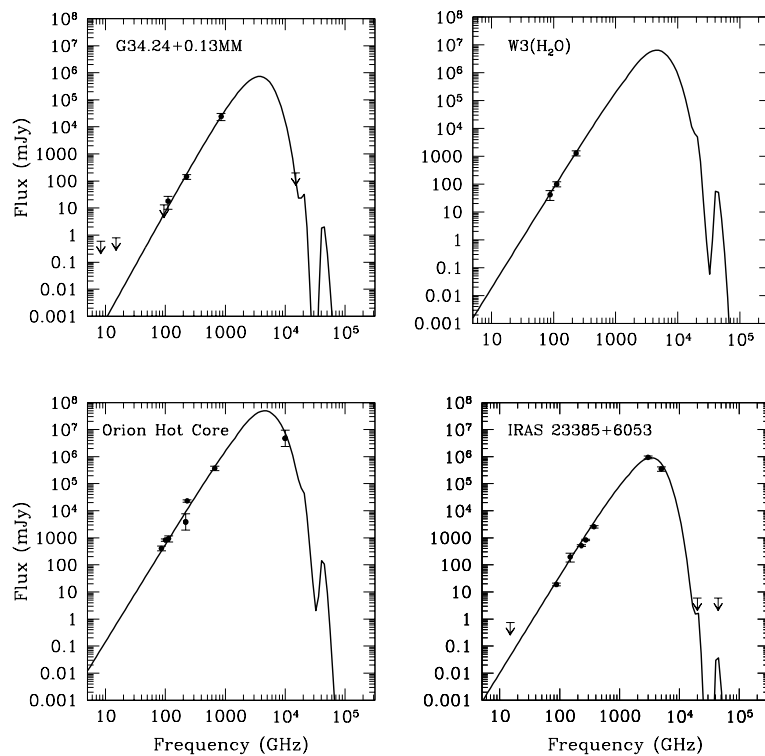


**Figure 1.1:** Examples of predicted spectral energy distributions of deeply embedded massive (proto)stars (taken from Osorio et al 1999). Characteristic for these 1-dimensional models is the lack of strong emission in the near-infrared ( $\nu > 10^5$  GHz), a steep increase of flux in the thermal and mid-infrared ( $\nu \sim 10^4$  GHz), and the peak of the SED in the far-infrared between 60 to 80 micron ( $\nu \sim 3...6 \times 10^3$  GHz).

### 1.1.2 Setting the stage

It appears to be a common fashion that most publications about high-mass star formation started with a variation of the phrase “Our present knowledge of high-mass star formation is still very poor.” If we make the comparison with details of low-mass star formation this seems to be indeed a fair statement. However, during recent years a considerable development<sup>5</sup> is perceivable for some aspects. It is an established fact that also high-mass star-forming regions are associated with powerful molecular outflows (e.g., Shepherd & Churchwell 1996, Henning et al. 2000). Recent interferometric work provides more and more evidence that such outflows can be as well-collimated as in low-mass star-forming regions (Beuther et al 2002a, 2002b, 2003, Su et al. 2004a). These points strengthen a general accretion scenario.

Bonnell & Bate (2002) end with the conclusion that stellar cluster densities have to be very high ( $\sim 10^8 \text{pc}^{-3}$ ) to make the coalescence mechanism work. Such conditions are probably not fulfilled in Galactic clusters, but maybe in starburst galaxies. Investigations of radiative feedback in case of Bondi-Hoyle accretion (an important mechanism for further mass gain

<sup>5</sup>However, keep in mind that “sometimes, development is not equal to progress.” (Derek Ward-Thompson at the IAU Symposium 221 in Sydney in 2003)

in clusters in the context of the coalescence scenario) by Edgar & Clarke (2003, 2004) show that this feedback mechanism poses similar problems to the build-up of massive stars than in the accretion scenario. Hence, the original coalescence scenario has encountered several problems.

What can the observers actually observe? The earliest stages of massive star formation are very difficult to trace, and research on it is still in its infancy. These objects are sometimes called pre-protocluster cores (PPcICs, Evans et al. 2002) or high-mass starless cores (HM-SCs, e.g., Beuther & Shepherd 2005). An insight gathered during the last few years is that so-called InfraRed Dark Clouds (IRDCs, see Egan et al. 1996) and objects found in the ISO Serendipity Survey (Bogun et al. 1996) might be great hunting grounds to look for this class of objects, and several large-scale (sub)mm and FIR surveys are in progress or provided first results already (e.g., Krause et al. 2003).

As a next stage it is expected that high-mass protostellar or protoclusters objects form in the above-mentioned cores. For such objects in the precursor stage to an UCHII region, the abbreviation HMPO has been coined (e.g., Sridharan et al. 2002). Special attention has been directed in recent years to the so-called Hot Molecular Cores (HMCs) which are considered to belong to the HMPO stage.

### What are Hot Molecular Cores?

The majority of studies in high-mass star formation in the 1990's has been aimed at ultra-compact HII regions (UCHIIs). These objects mark a stage, when the embedded star (or the cluster of stars, respectively) has already ionised a substantial amount of the surrounding gas (e.g., Wood & Churchwell 1989a, Kurtz et al. 1994). Over the last decade, it has become possible to explore earlier stages in the evolution of massive young stellar objects (mYSOs). Recent studies have revealed that warm ( $T \geq 100$  K), dense ( $n_{\text{H}_2} = 10^6 \dots 10^8 \text{ cm}^{-3}$ ) and compact (size  $\leq 0.1$  pc) condensations within the molecular clouds, christened "Hot Molecular Cores", can provide insights into even earlier phases of the formation of high-mass stars (Cesaroni et al. 1994, Kurtz et al. 2000).

It was found that HMCs are close to, but often not coincident with, the adjacent UCHII regions (Cesaroni et al. 1994). Due to the fact that the relatively high HMC temperature has to be maintained, a high energy input is required which gives rise to the assumption that one (or several) very young high-mass star(s) can act as the heating source. One crucial question is to decide whether internal or external heating is responsible for the hot core phenomenon. The analysis of individual cases confirms the possibility that a young massive star could indeed be present inside the HMC warming the molecular gas (Olmí et al. 1996, Cesaroni et al. 1998, Testi et al. 2000). Because of their special physical conditions, the HMCs provide a very interesting chemistry (e.g., Ohishi 1997, Millar 1997, Rodgers & Charnley 2003), a fact that could be verified in several ambitious molecular line surveys (e.g., Hatchell et al. 1998). Several authors have proposed an evolutionary scenario leading from HMCs to so-called hypercompact HII regions and, eventually, to UCHII regions (Cesaroni et al. 1994, Kurtz et al. 2000, Keto 2002, Keto 2003).

As a general feature of HMPO, it is expected that massive circumstellar extinction interferes with the observations of such objects. Therefore, as we mentioned above, mainly centimetre and millimetre radio observations have contributed to our understanding of HMPOs. However, we need to gain information in the Wien part of the spectral energy distribution of these young stellar objects.

## 1.2 Goals of the presented work

Gathering such information is not an easy task. Though NIR observation techniques have matured immensely over the years, this wavelength range is not the best-suited one for studying HMPOs, since the extinction can still be overwhelmingly large. In this respect, imaging and spectroscopy at mid-infrared (MIR, 3 – 20  $\mu\text{m}$ , also called thermal infrared) wavelengths provides a powerful tool in order to enlarge our knowledge about deeply embedded high-mass sources. Compared to the near-infrared, the optical depth is much lower in the MIR, which provides a deeper view into the dense and dusty YSO envelopes. The number of such investigations that are explicitly targetted towards HMPOs is constantly rising during the last three years (e.g., Stecklum et al. 2002a, 2002b, De Buizer et al. 2002, 2003, Pascucci et al. 2004), but the total number is still low.

Hence, in this thesis we want to explore the possibilities of thermal infrared observations with high spatial resolution in connection with the new generation of instruments that got available around the time when this thesis project started.

The high spatial resolution is important not only to resolve the confusion due to the multiplicity of sources in the region of interest. A fundamentally important issue is how exactly the transformation from the HMPO stage into the more evolved UCH<sub>IR</sub> stage occurs and how these changes are reflected in the appearance of the central object and of vicinity regions (for instance changes in morphology, conversion into non-spherical structures).

We chose to deeply scrutinise two prominent HMPOs in the regions G9.62+0.19 and GGD 27 to tackle these questions. As a side effect of our thorough investigation of two unique sources that are already well investigated, we can strengthen but also revise previous knowledge about our sources of interest.

Although our emphasis lies on thermal infrared observations, we follow a clear multi-wavelength approach in this thesis! We will demonstrate the success of this policy and we will highlight potential pitfalls, especially when previously existing information is not critically reassessed.

In Chapter 2 we introduce the two main sources we have analysed based on a multitude of observations. Technical details of these observations are also given in several subsections. The two main parts of this thesis (Chapter 3 and Chapter 4) are devoted to the presentation and discussion of our observational results for the Hot Core region G9.62+0.19-F and the massive young stellar object GGD 27-ILL, respectively.

In Chapter 5 we set some important findings for these two objects into context and look for a general trend in the properties of a larger sample of HMPOs that we plan to analyse by means of VLA 7-mm imaging.

Finally, in the summary Chapter 6 we re-iterate the most important results of the presented investigations. Based on this, we draw general conclusions and address the prospects for future work in the field of HMPO observations.

## **Chapter 2**

# **Source Selection and Observations**

## **2.1 Objects for detailed studies**

For detailed infrared (IR) investigations of HMPO candidates, we decided to choose the targets from a sample of sources for which a common effort is ongoing to map these young high-mass sources with the *VLA* at 7 mm. In Chapter 5 we will briefly introduce the whole sample and discuss some global IR properties of these regions based on the commonly available IR source catalogues. In this chapter we introduce in more detail the two region for our detailed studies – G9.62+0.19 and GGD 27. Since for our project the availability of ESO telescopes and instrumentation was one of the boundary conditions, mainly the southern sources of the *VLA* sample came into focus. Among these targets, G9.62+0.19 and GGD 27 stand out because each of them shows a unique feature as we will see below. Our interest in G9.62+0.19 increased even more due to the fact that near-infrared VLT observations with *ISAAC* were already available in the ESO data archive.

### **2.1.1 G9.62+0.19**

The well-studied galactic region G9.62+0.19 (Garay et al. 1993, Hofner et al. 1996) at a distance of  $\sim 5.7$  kpc (Hofner et al. 1994) contains a number of massive YSOs in different evolutionary stages located close to each other. In this respect, there are indications that there is an age gradient from western (older) regions to eastern (younger) ones (Hofner et al. 1994, 1996, Testi et al. 1998). One of the most interesting objects of the region (source F) has been confirmed to be an HMC (Cesaroni et al. 1994, Hofner et al. 1994, 1996) by means of interferometric observations of the dense gas tracers  $\text{NH}_3$  and  $\text{CH}_3\text{CN}$ . From high-sensitive *VLA* measurements (Testi et al. 2000) weak cm-continuum radiation was found recently for component F, which is situated between two UCHIIs (radio components D and E).

Another feature, which makes this HMC a unique target, is the fact that very close to the location of G9.62+0.19–F emission in the  $2.2 \mu\text{m}$  continuum (K band) was detected (Testi et al. 1998). According to the standard models of HMCs, in which these are described as spherically symmetric and extremely dense dust and gas spheres (Kaufman et al. 1998, Osorio et al. 1999, Nomura & Millar 2004), the optical depth is so high that the HMC should

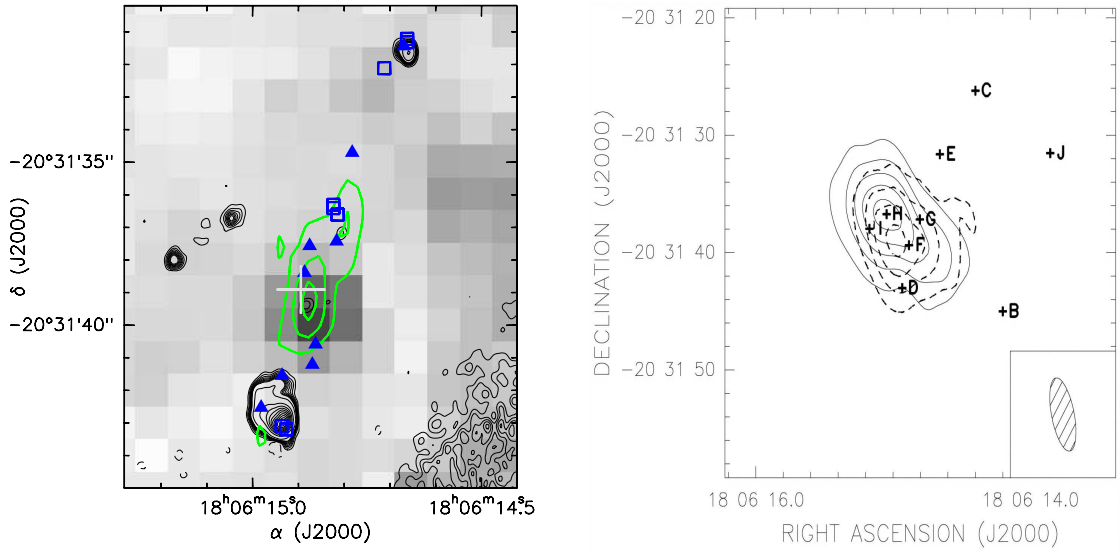


**Figure 2.1:** Collection of features for G9.62+0.19 as they were known in the year 2001. **Left panel:** The 3.6 cm continuum (thin black contours, Testi et al. 2000) and the thermal NH<sub>3</sub>(5,5) emission (thick green contours, Hofner et al. 1994) maps are overlaid on the 2.2  $\mu$ m near-infrared image of Testi et al. (1998) of the G9.62+0.19 D–F region. Filled triangles are H<sub>2</sub>O masers (Hofner & Churchwell 1996), open squares denote previously known OH masers, the cross marks the position of the mm continuum source F (Hofner et al. 1996). **Right panel:** Contour plot of HCO<sup>+</sup>(1–0) red (solid lines) and blue (dashed lines) outflow lobes according to Hofner, Wiesemeyer & Henning (2001). The outflow is seen almost pole-on and seems to be associated with the HMC component F.

remain undetectable at near- and mid-infrared wavelengths (see Fig. 1.1). This raises the question what the actual origin of the K band emission is. In this respect it is important to mention that Hofner et al. (2001) have detected a molecular outflow in G9.62+0.19 with the flow orientation very close to the line of sight, for which they favour component F as the most likely driving source. The working hypothesis of Hofner et al. (2001) was that the outflow forms a cavity of strongly decreased density roughly along the line of sight through which the infrared emission from the HMC can escape (cf. Gibb et al. 2004b).

### 2.1.2 GGD 27

Originally (mis)classified as an optical candidate for a Herbig–Haro object (Gyulbudaghian et al. 1978), GGD 27 turned out to be a highly active star-forming region in the light of radio and infrared observations. OH and H<sub>2</sub>O masers as well as a radio continuum source were found at the location of GGD 27 (Rodríguez et al. 1980). This radio emission could later be associated with the deeply embedded IRAS source 18162–2048, that (placed at a distance of 1.7 kpc) implies the presence of a massive luminous object ( $1.7 - 2.0 \times 10^4 L_{\odot}$ ). Martí et al. (1993) revealed a bipolar radio jet system with a total projected extent of  $\sim 5.3$  pc, emanating from the radio continuum source. The flow gives rise to some of the most luminous Herbig–Haro objects yet discovered, namely HH 80, HH 81, and HH 80–North, all located at a distance of more than 2 pc from their energy source. But even more remarkable is the



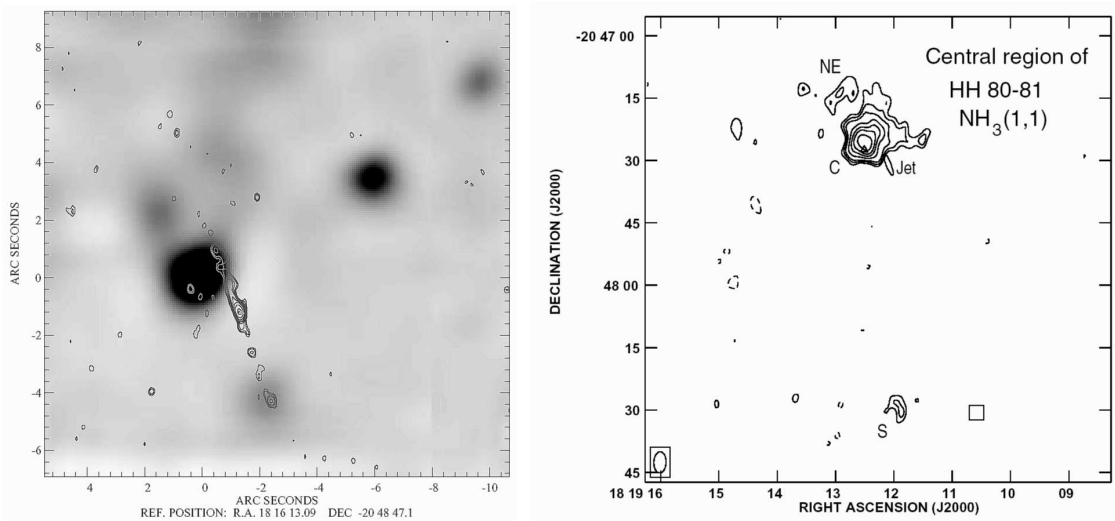


**Figure 2.2:** Overview over some important observational facts about GGD 27 as they were known in the year 2003. **Left panel:** The contours mark the inner part of the large GGD 27 radio jet, seen with the VLA at 3.6 cm (Martí et al. 1993). The central source (offset coordinates  $-2.8, -1.2$ ) shows the strongest emission. The underlying  $2.2 \mu\text{m}$  speckle image of the GGD 27 centre region (Stecklum et al. 1997, mind the B1950 coordinates in this case) with a spatial resolution of 0.7 arcseconds shows previously known NIR sources and convincingly demonstrates the fact that GGD 27–ILL, the IR counterpart of the jet–driving source, is not visible at  $2.2 \mu\text{m}$ . **Right panel:** The VLA ammonia observations of Gómez et al. (2003) revealed several ammonia cores with different physical properties. Note that the jet–driving source is displaced from the centre of the strongest molecular core denoted C.

high degree of collimation the jet possesses. The jet opening angle implied by the size and location of the HH objects is only  $\sim 1^\circ$  which suggests an extraordinarily well collimated jet (Martí et al. 1995, 1998).

Many efforts were undertaken to identify the central radio source at higher frequencies. Near–infrared studies showed an IR reflection nebula and several point sources in the central region of GGD 27. By means of subsequent polarimetric and spectroscopic studies the potential illuminator of that area was estimated to be an embedded object GGD 27–ILL, hidden from direct view even in the near–infrared and located in the proximity of the NIR source IRS2 (Tamura et al. 1991, Aspin et al. 1991). This proposed object would be coincident with the jet–driving radio continuum source. Finally, Aspin et al. (1994) and Stecklum et al. (1997) could directly image the embedded object (with a limited resolution of  $1''.5$ ) in the thermal infrared at  $4.7$ ,  $8.5$  and  $11 \mu\text{m}$ . However, these previous IR observations did not resolve GGD 27–ILL and hence could not clarify questions about a potential substructure. Nevertheless, GGD 27–ILL remained a promising candidate for a circumstellar disk around a very young and massive star based on circumstantial evidence.

Gómez et al. (2003) showed first results to approach GGD 27–ILL by means of VLA 7–mm observations, but their data (taken in the early days of the VLA 7–mm system) just showed an unresolved object coincident with the jet–driving source. Furthermore, a quite complex molecular environment with several clumps has been presented by means of BIMA observations.

## 2.2 Infrared and Millimetre Telescopes and Cameras

**Table 2.1:** Summary of single-telescope observations discussed in this thesis

Date	Objects <sup>a</sup>	Filter and $\lambda_c$	Telescope / Camera	FOV <sup>b</sup>	PSF FWHM	Calibrator
1999 Sep	(1)	J 1.25 $\mu\text{m}$	ANTU / ISAAC	151''	0'55	S234-E, S071-D
1999 Sep	(1)	H 1.65 $\mu\text{m}$	"	151''	0'65	S234-E, S071-D
1999 Sep	(1)	Ks 2.16 $\mu\text{m}$	"	151''	0'55	S234-E, S071-D
2001 May	(1)	nb_K 2.09 $\mu\text{m}$	"	<sup>c</sup> 151''	0'65	–
2001 May	(1),(2)	H <sub>2</sub> (1–0)S1 2.122 $\mu\text{m}$	"	151''	0'48	–
2001 May	(1),(2)	Br $\gamma$ 2.166 $\mu\text{m}$	"	151''	0'44	–
2001 Jun	(1),(2)	L' 3.78 $\mu\text{m}$	"	79''	0'55 $\times$ 0'42	HR 6070
2001 Jun	(1),(2)	nb_M 4.66 $\mu\text{m}$	"	79''	0'47 $\times$ 0'40	HR 6070
2003 May	(2)	N band spectrum	ESO 3.6-m / TIMM12	1'2 $\times$ 70''	–	HD 178524
2003 Jul	(3)	M 4.70 $\mu\text{m}$	"	95'' $\times$ 71''	1'08	HD 169916
2003 Jul	(1),(2)	N1 8.70 $\mu\text{m}$	"	64'' $\times$ 48''	0'86	HD 169916
2003 Jul	(2)	N2 9.80 $\mu\text{m}$	"	64'' $\times$ 48''	0'90	HD 169916
2003 Jul	(1),(2), (3)	N4 11.66 $\mu\text{m}$	"	64'' $\times$ 48''	0'86	HD 169916
2003 Jul	(1),(2), (3)	Q2 18.75 $\mu\text{m}$	"	64'' $\times$ 48''	1'60	HD 187642
1999 Jun	(1)	N4 11.70 $\mu\text{m}$	5-m Hale / SC-10	16''	0'76	$\delta$ Oph
2004 Jun	(2)	[NeII] 12.81 $\mu\text{m}$	VLT / MIDI	2''	0'39	HD 169916
2003 Jul	(1),(2), (3)	mm 1.2 mm	SEST / SIMBA	560'' $\times$ 900''	24''	Uranus

<sup>a</sup> Object code for the observations: (1) – G9.62+0.19, (2) – GGD 27, (3) – Mol 45

<sup>b</sup> Field of view for single frames, respectively

<sup>c</sup> Imaging polarimetry with Wollaston prism and slit mask in the optical path

### 2.2.1 J, H, and Ks band observations

The broad-band near-infrared data for G9.62+0.19 were obtained in September 1999 with the infrared camera ISAAC (Moorwood 1997) at the VLT ANTU telescope within the programme ID 63.I-0329. We used the opportunity to utilize these archived data for our purposes.

The following NIR broad-band filters were used: J ( $\lambda_c = 1.25 \mu\text{m}$ , FWHM = 0.29  $\mu\text{m}$ ), H ( $\lambda_c = 1.65 \mu\text{m}$ , FWHM = 0.30  $\mu\text{m}$ ), K<sub>s</sub> ( $\lambda_c = 2.16 \mu\text{m}$ , FWHM = 0.27  $\mu\text{m}$ ). The seeing conditions were between 0.65 arcsec (H-band) and 0.55 arcsec (J- and K<sub>s</sub>-band), respectively. The pixel scale is 0'147/px which results in a field of approximately 2'5  $\times$  2'5. Within the overlap area of the 5 offset images per wavelength, the total integration time on source for each filter was 266 s. After the standard procedure (dark-field and flat-field reduction, bad pixel removal and sky subtraction), utilizing our own IDL<sup>1</sup>-based reduction pipeline for the ISAAC data (see also Stecklum et al. 2003, Apai et al. 2005), we corrected for the field distortion by applying the correction terms recently provided by ESO. Then the 5 dithered

<sup>1</sup>Interactive Data Language

frames were combined to a larger mosaic image achieving subpixel accuracy. As standards for photometric calibration, the stars S234–E and S071–D (from the list of faint NIR standard stars by Persson et al. 1998) were observed before and after the observation of G9.62+0.19, respectively.

### 2.2.2 Br $\gamma$ and H<sub>2</sub> observations and K narrow-band polarimetry

Images of G9.62+0.19 and GGD 27 in the Br  $\gamma$  ( $\lambda_c = 2.16 \mu\text{m}$ , FWHM =  $0.02 \mu\text{m}$ ) and in the H<sub>2</sub>(1–0)S1 ( $\lambda_c = 2.12 \mu\text{m}$ , FWHM =  $0.02 \mu\text{m}$ ) narrow-band filters were obtained in May, 2001, again with *ISAAC* at the *VLT ANTU* telescope. Pixel scale and field of view are the same as for the JHK<sub>s</sub> broadband imaging. The total integration times on source for both filters were 500 s within the overlap area of the 5 offset images per wavelength.

The imaging polarimetry system of *ISAAC* was used to obtain complementary NIR data for the G9.62+0.19 region. The camera is equipped with a Wollaston prism which divides the infalling light into two perpendicular polarised beams having a separation of  $\sim 22''$ . The prism is used with a special slot mask (3 opaque stripes, each being  $20''$  wide) to keep the two fully polarised copies of the imaged area separated on the detector. The first step is to simultaneously obtain the  $0^\circ$  and  $90^\circ$  data. Then, the reference plane is rotated by  $45^\circ$  by offsetting the image de-rotator of the alt-az mounting control system of the telescope accordingly. In this way, the  $45^\circ$  and  $135^\circ$  data can be obtained. To ensure a seamless coverage of the entire star-forming region, we used a 3-point dither pattern perpendicular to the stripe orientation. A narrow-band K filter was used ( $\lambda_c = 2.09 \mu\text{m}$ , FWHM =  $0.02 \mu\text{m}$ ), which does not contain strong spectral lines.

### 2.2.3 L' and nb\_M band observations

*ISAAC* is also capable of imaging in the L' ( $\lambda_c = 3.78 \mu\text{m}$ , FWHM =  $0.58 \mu\text{m}$ ) and nb\_M ( $\lambda_c = 4.66 \mu\text{m}$ , FWHM =  $0.10 \mu\text{m}$ ) thermal infrared narrow bands. Within our programme 67.C-0264, service time observations were performed in June, 2001, thus, very shortly after the repair of the *ISAAC* chopping secondary mirror in April and May, 2001. The fact that during the first weeks after recommission of the chopping mode the data were taken without field stabilisation resulted in a slightly degraded image quality, recognizable by means of slightly elongated star shapes. The pixel scale in connection with the *ALADDIN* detector array is  $0'.071/\text{px}$ , the field of view is then  $73'' \times 73''$ . Since the L' and M bands lie within the thermal infrared, on-source/off-source chopping is required to remove the thermal background in the images. Therefore, we have the positive and the negative beam in the images, separated by 15 arcsec. In addition, a 5 point dither pattern was applied. The standard star HR 6070 (van der Bliik et al. 1996) was used to calibrate the data.

### 2.2.4 N and Q band observations

We used the *TIMMI2* camera (Reimann et al. 2000) at the ESO 3.6-m telescope for observations in several medium-band filters in July 2003. Equipped with a  $320 \times 240$  px<sup>2</sup> Si:As BIB *Raytheon* array, the FOV in the high-resolution mode is  $64'' \times 48''$ . Hereby the N1, N2 (only for GGD 27), N4 (ESO terminology:  $11.9 \mu\text{m}$  filter), and Q2 filters were applied (FWHM =  $1 \mu\text{m}$ ).

For G9.62+0.19, another MIR camera was utilised to perform imaging in the N4 filter. These data were obtained in June 1999 using *SpectroCam-10* (Hayward et al. 1993) at the 200-inch Hale Telescope of the Palomar Observatory<sup>2</sup>. The effective wavelength of this N4 filter was  $11.7 \mu\text{m}$  with a FWHM of  $1 \mu\text{m}$ . After applying a standard chop-and-nod reduction for the raw frames a 3 frame mosaic was combined into the final image. The average on-source integration time at each pixel is 500 s. The star  $\delta$  Oph (HD 146051) served as standard for the flux calibration.

With the *TIMMI2* data we tested a different (and perhaps more sophisticated) approach to create the final image, namely the so-called projected Landweber matrix restoration (Bertero et al. 2000 and references therein). We refer to appendix C for some comments about the restoration method itself and the modifications we applied.

Because of our modified chop/nod observational approach we have to deal with artifacts (see appendix C) in two orthogonal directions. We have undertaken the first steps to reduce these collateral effects (e.g., ghost images) by precisely aligning the array orientation along the chopping/nodding throws and by carefully registering the real values of the throws. A simple way to minimize the multiple artifacts would be, according to Bertero et al. (2000), to combine several restored images each having different throws. Since during the observations we used only two different throw values we were not able to completely avoid these perturbing effects. In this respect one has to remember that a part of the original signal is then still contained in the artefacts. The effects on photometric accuracy are under investigation. We will use the restored *TIMMI2* images only to reveal the MIR morphology of the regions. Concerning photometric information we will rely on the unrestored *TIMMI2* and *SpectroCam-10* data.

An N-band grism spectrum has been obtained for GGD 27-ILL with *TIMMI2* on May 31, 2003. A slit width of  $1''.2$  was used that resulted in an effective spectral resolution of  $R \sim 170$  at  $\lambda = 10 \mu\text{m}$ . A standard chopping/nodding technique was used (chopping parallel to nodding along the slit,  $10''$  throw). The source was observed at an airmass of  $\sim 1.015$  during almost photometric conditions. The standard star HD 178524 was observed roughly at the same airmass as the science target and was used to calibrate the spectrum. The data were reduced adapting an *IDL* pipeline kindly provided by R. Siebenmorgen (Siebenmorgen et al. 2004).

<sup>2</sup>Observations at the Palomar Observatory were made as part of a continuing collaborative agreement between the California Institute of Technology, Cornell University, and the Jet Propulsion Laboratory.

### 2.2.5 1.2-mm continuum observations

The 1.2-mm continuum observations of G9.62+0.19, GGD 27, and Mol 45 were carried out with the 37-channel bolometer array *SIMBA* (Nyman et al. 2001) at the *SEST* on La Silla, Chile, in July 2003. *SIMBA* is a hexagonal array in which the HPBW of a single element is about 24'' and the separation between elements on the sky is 44''. Maps of Uranus were taken to check the flux calibration of the resulting data. To correct for the atmospheric opacity, skydips were performed every 2–3 hours. Despite the occurrence of some thin clouds, the observing conditions turned out to be quite good which is reflected in zenith opacity values of 0.16 – 0.18. The pointing was checked roughly every two hours and appeared to be better than 6'' rms. However, when comparing the positions of 1.2-mm sources in our data with recognised features at other wavelengths (see for instance Sect. 4.3.2), often a systematic offset mainly in right ascension seems to exist. Hereupon, we compared our result for one source taken during the observing campaign (IRAS 09002–4732, see Apai et al. 2005) with *SIMBA* maps obtained by other groups (Faúndez et al. 2004, Zinchenko 2005). We list here the B1950 peak positions for comparison.

Faúndez	09 00 12.07	–47 32 08.7
Zinchenko	09 00 11.80	–47 32 14.0
our peak	09 00 11.29	–47 32 17.7

Our shift relative to the Zinchenko results is (–5.0'', –3.7''), while it is (–7.9'', –9.0'') relative to the Faúndez results. The shifts are not that large (considering the beamsize of 24'') and the positional error bars probably overlap. However, at least a tendency to give lower values both in RA and Dec is obvious in our case, and we should keep this in mind when dealing with our *SIMBA* source positions.

The observations were made using a fast-scanning technique without a wobbling secondary (Reichert et al. 2001). The scans are done in azimuth with 80''/s, separated in elevation by 8''. The raw data were reduced with the *MOPSI* mapping software package developed by R. Zylka (*IRAM*, Grenoble, France), using a deconvolution algorithm to remove the contribution of the electronics arising from the fast-scanning observing mode (Weferling et al. 2002). Following the suggestions of the *SIMBA* manual, the reduction was done in three steps. First, a standard recipe was used to create an intensity map for defining proper baseline regions in order to avoid artifacts close to the source. In the next stage, a model of the source is created using the previous map. This model is used in the correlated sky noise filtering during the last step. The combination of 3–4 maps per source (size 560'' × 900'' each) resulted in a residual noise between 25 – 40 mJy/beam (rms).

## 2.3 Interferometry with the VLA 7-mm system

### 2.3.1 The VLA – A very short introduction

The Very Large Array (*VLA*) is a radio synthesis imaging interferometer, operated by the National Radio Astronomy Observatory (NRAO), that consists of  $27 \times 25$ -m dishes, arranged in the characteristic Y-shape and located in the plains of San Augustin near Socorro, New Mexico. The number of dishes results in up to 351 baselines. This ensures a good (instantaneous) uv-coverage which makes the *VLA* a very flexible instrument that is also well-suited for snapshot surveys. Four main array configurations are available within a 16-months cycle. The maximum baselines range from 1 km (D configuration) up to 36 km (A configuration). The *VLA* can operate at wavelengths between 4 m down to 7 mm, although the wavelength coverage is not yet continuous<sup>3</sup>. For our purposes we are most interested in the 7-mm capabilities of this interferometer. First, at this wavelength one can reach a spatial resolution from  $2''$  down to  $0''.05$  in the synthesized image. Sensitivities of down to  $40 \mu\text{Jy}$  are reachable for 8 hours on source at this wavelengths. Such values are still outstanding compared to other millimetre interferometers. The second reason for our interest in the *VLA* 7-mm system is a more astrophysical one. The actual HMPOs mostly do not possess a large volume of ionised circumstellar gas around that could cause strong centimetre emission. Small hypercompact HII regions might exist, but they can be quenched by accretion or other effects (Walmsley 1995, Keto 2002, 2003) and hence remain optically thick for free-free emission up to relatively high frequencies  $\geq 20$  GHz. It may be that the turn-over to the optically thin regime is shifted to the millimetre range (e.g., Tieftrunk et al. 1997), where the *VLA* could trace this behavior at 7 mm. Furthermore, star-forming regions are known to contain large amounts of dust. Its emissivity at 7 mm is much lower than at submillimetre wavelengths, indeed, but, given the performance of the *VLA*, dust emission is, in principle, detectable at 7 mm.

### 2.3.2 Our B-array observations

The high-resolution 7-mm continuum and  $\text{CH}_3\text{OH}$  maser observations toward GGD 27-ILL were made with the *VLA* in the B configuration on December 21, 2003 and January 6, 2004. These were daytime observations, and the atmospheric conditions were rather mediocre regarding the phase stability needed for millimeter interferometry. We therefore decided to apply a maser cross calibration technique (Reid & Menten 1990). In such a case, the radio continuum and a maser line are observed simultaneously by using a slightly advanced correlator setup. Thus, the strong maser(s) can be used to continuously monitor the behaviour of the atmosphere and to calibrate the continuum measurements. This approach was successfully used mainly for observations at 1.3 cm where strong  $\text{H}_2\text{O}$  masers are available in many star-forming regions (e.g., Torrelles et al. 1996, Martí et al. 1999). Application

---

<sup>3</sup>Continuous coverage is planned in the framework of the so-called expanded *VLA* (e*VLA*) project, that will bring major upgrades for the *VLA* up to the year 2010.

of this method in the 7-mm band is, as far as we know, only reported toward the Orion BN/KL region, where the investigators (Menten & Reid 1995, Chandler & Wood 1997) were fortunate to find strong 43.1 GHz SiO(1  $\rightarrow$  0)  $\nu = 1$  maser emission, an “exceedingly rare phenomenon in star-forming regions”. However, a recently completed VLA Methanol maser survey (Kurtz, Hofner & Vargas Álvarez 2004) established a considerable number of massive star-forming regions harbouring 44 GHz methanol masers, among them GGD 27. Thus, we tried the cross calibration with this maser at both observing dates. We observed simultaneously two different bandwidths of 3.125 MHz (63 channels of 48.8 kHz each) and 25 MHz (7 channels of 3.125 MHz each) in both circular polarisations, respectively. The narrow bandwidth was centered at the frequency of the CH<sub>3</sub>OH 7(0,7)–6(1,6) A+ maser line (44069.476 MHz) with  $v_{\text{LSR}} = +13.0 \text{ km s}^{-1}$ . The broad bandwidth was shifted by 50 MHz to avoid strong line contributions and centered at the frequency of 44119.476 MHz for continuum measurements. The absolute amplitude calibrator was 1331+305 (a.k.a. 3C286) and the phase calibrator was 1733–130, both names in the J2000 coordinate system. Alternating to the observations of GGD 27 itself, a three minute scan of 1733-130 was done every 45 minutes, a time span too long to reliably calibrate the weak continuum source, but sufficient to calibrate the strong masers in first order. Once the strongest CH<sub>3</sub>OH maser component was identified in a particular spectral channel of the narrow bandwidth (the channel at = 13.2 km/s), we self-calibrated its signal in phase and amplitude. The corrections collected in the herewith produced calibration tables were subsequently applied to the broadband continuum data (doing the cross calibration). A detailed discussion of algorithmic details of the maser cross calibration is given in Appendix D.

## **Chapter 3**

# **G9.62+0.19 – An HMC puzzles the IR observers**

While the G9.62+0.19 region was covered over the years by many radio observations with ever increasing resolution and sensitivity, detailed information about this star-forming region in the infrared is rather scarce. Utilising high-resolution near- and mid-infrared data, we have explored the IR properties of this region. In Sect. 3.1 – 3.5 we present the direct results of these measurements and discuss the global features of the region and the specific properties of the HMC zone on which the emphasis of our analysis will lie. Since accurate astrometry will be a crucial issue for the following interpretation of the data, we include a detailed description of the astrometric techniques we have applied in the appendices A and B. In combination with interferometric radio maps and a radiative transfer model, we discuss the implications of our infrared data for the interpretation of the objects in the HMC region in Sect. 3.6. Furthermore, we compare in Sect. 3.7 the HMC region to the UCHIIs nearby and to the HMC in W3(H<sub>2</sub>O). We also give some estimations for the distribution of local extinction in Sec. 3.8. Finally, in Sect. 3.9 we summarise our conclusions.

### **3.1 Near-infrared broad-band data**

In Figs. 3.1 and 3.3 we show 3-colour composites derived from the *VLT* J–H–K<sub>s</sub> data, where Fig. 3.3 shows the inner part of Fig. 3.1 in more detail and serves as a reference for the radio observation nomenclature we have adopted to indicate the various components.

Fig. 3.1 displays the global morphology of the star-forming complex G9.62+0.19. The extended diffuse region in the centre of the image dominates the near-infrared emission and can be related to the more evolved HII component B in Fig. 3.3. This region harbours a cluster of modestly embedded stars. Many of them show infrared excess. Recently, Persi et al. (2003) analysed in detail this population of stars in the G9.62+0.19 B and C regions.

Eastwards of this emission, one can notice an extinction gradient. Hence, the neighbouring area, beginning a few arcsec away from the eastern border of component B, appears darker and more obscured. The superimposed *MSX* contour lines which we derived from the



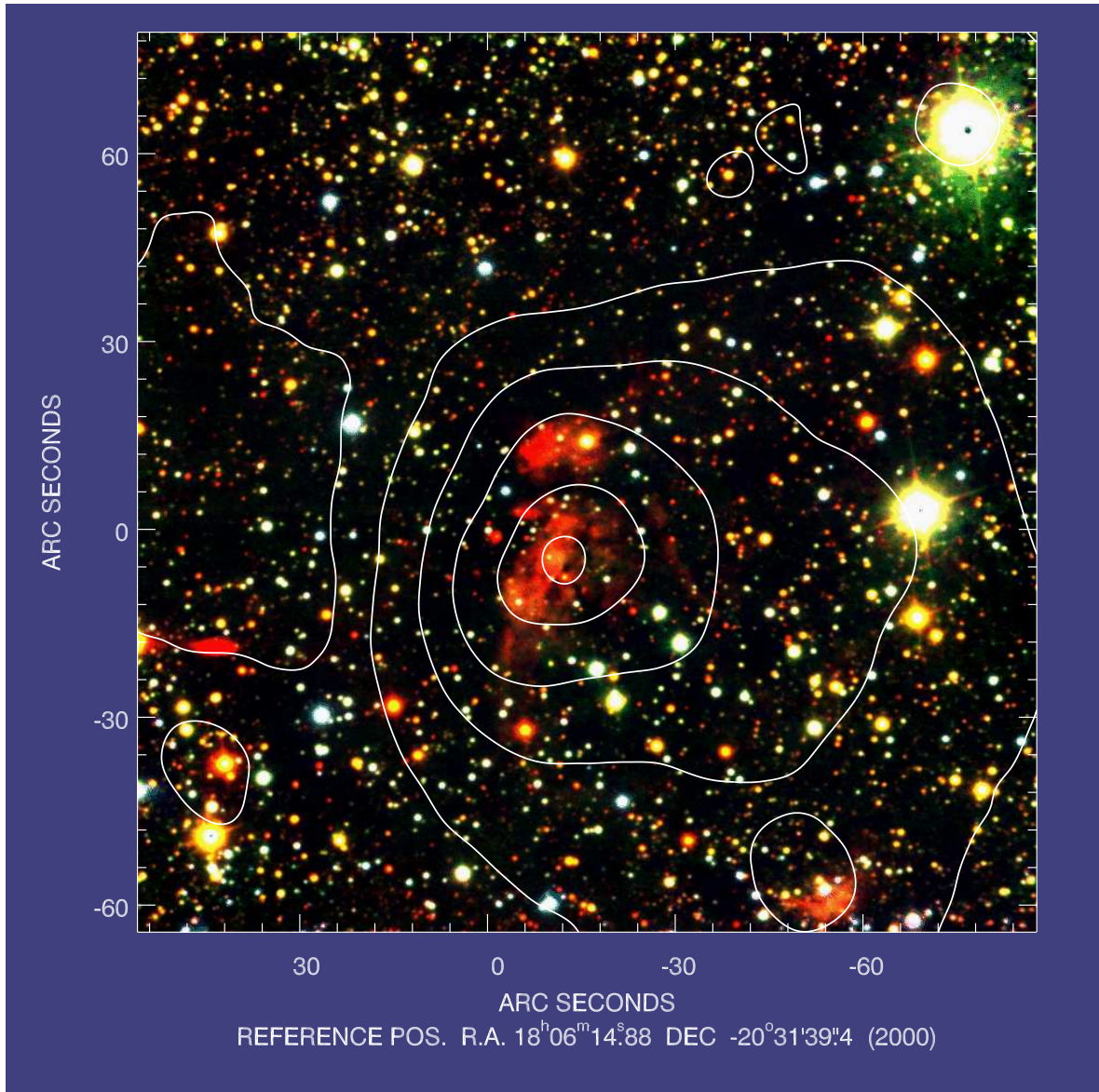


**Figure 3.1:** Colour-coded image of the entire G9.62+0.19 region taken in the three broad-band NIR filters J (blue), H (green), and K<sub>s</sub> (red). The large-scale contour lines denote the emission levels derived from the 8.28  $\mu\text{m}$  image of the related *MSX* source. The left-most large contour line indicates the position of the close-by Infrared Dark Cloud IRDC1 (see also Fig. 3.2).

8.28  $\mu\text{m}$  image of the related *MSX* source (Egan et al. 1996) experience the same decrease as the NIR emission towards the eastern darker region. This is a hint for a similar behaviour of the optical depth in the near- and mid-infrared. In fact, we categorise this eastern region as a so-called Infrared Dark Cloud (IRDC – see Egan et al. 1998). With our *SIMBA* mapping we covered the G9.62+0.19 region. We found that indeed this region (IRDC 1) is a source of millimetre emission (see Fig. 3.2). However, the HII complex G9.62+0.19 is nearby (considering the medium *SIMBA* resolution of 24'') and its millimetre emission overwhelms the relatively weak IRDC emission which nevertheless is detected as a bump to the left of the main emission. The 1.2-mm flux for the whole complex is  $(11.10 \pm 0.01)$  Jy, while the flux for IRDC 1 alone is around  $(0.21 \pm 0.04)$  Jy.

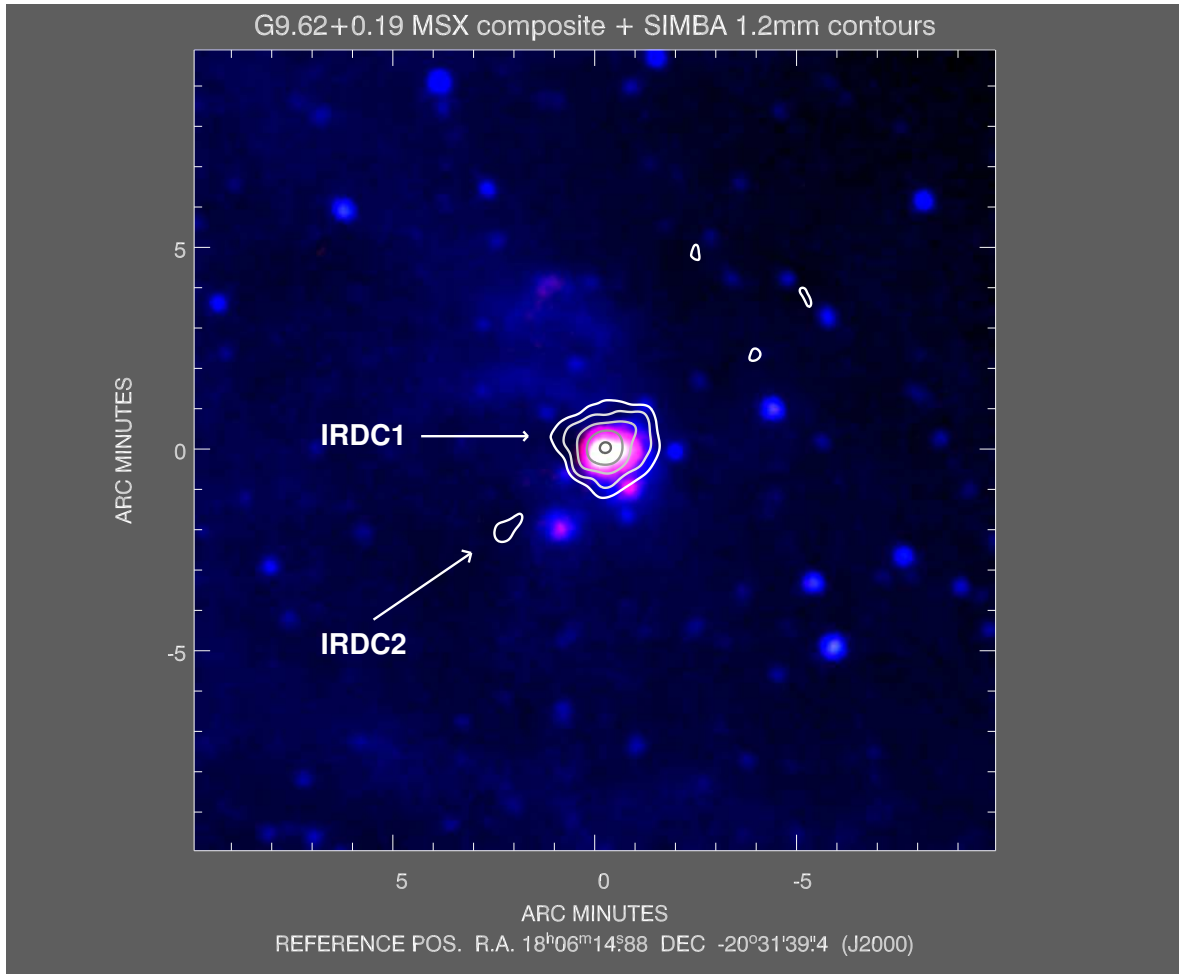


**Figure 3.2:** Large-scale view on the G9.62+0.19 region as seen by the MSX satellite. Blue colour indicates emission in the MSX A band ( $8.3 \mu\text{m}$ ), green is the average of C and D band ( $12 - 14 \mu\text{m}$ ), and red shows the E band signal ( $21.3 \mu\text{m}$ ). The 1.2 mm emission detected by *SIMBA* is overlaid as contours. The main millimetre emission arises from the UCH<sub>II</sub>/HMC complex G9.62+0.19; with IRDC1 we just denote the bump to the west of the main emission. The position of the hot core is at the reference coordinates.

The transition strip between IRDC 1 and the compact H<sub>II</sub> region component B is aligned roughly along the north–south direction and is populated with several more compact radio sources named C, D, E and F (Hofner et al. 1996, see also Fig. 3.3 for reference).

Mainly in the southwest of the radio component C we detect strong K band emission. The peak positions of the 3.6 cm and the NIR emission are clearly separated by almost 3 arcsec. This shift is obvious in Fig. 3.3, it is real and not an effect of an imprecise astrometry. The K narrow-band data and polarimetry data (Sects. 3.4 and 3.5) will throw light on this.

The components D and E are ultracompact H<sub>II</sub> regions (Hofner et al. 1996, Testi et al. 2000), where E might be associated either with an expanding ionised shell or with a wide-angle molecular outflow (Minier et al. 2001). Component D has a strong peak at 3.6 cm which can be recognized via the superimposed VLA contours in Fig. 3.3. Neither component shows a counterparts in our NIR data. We will discuss the consequences of these findings in Sect. 3.8.

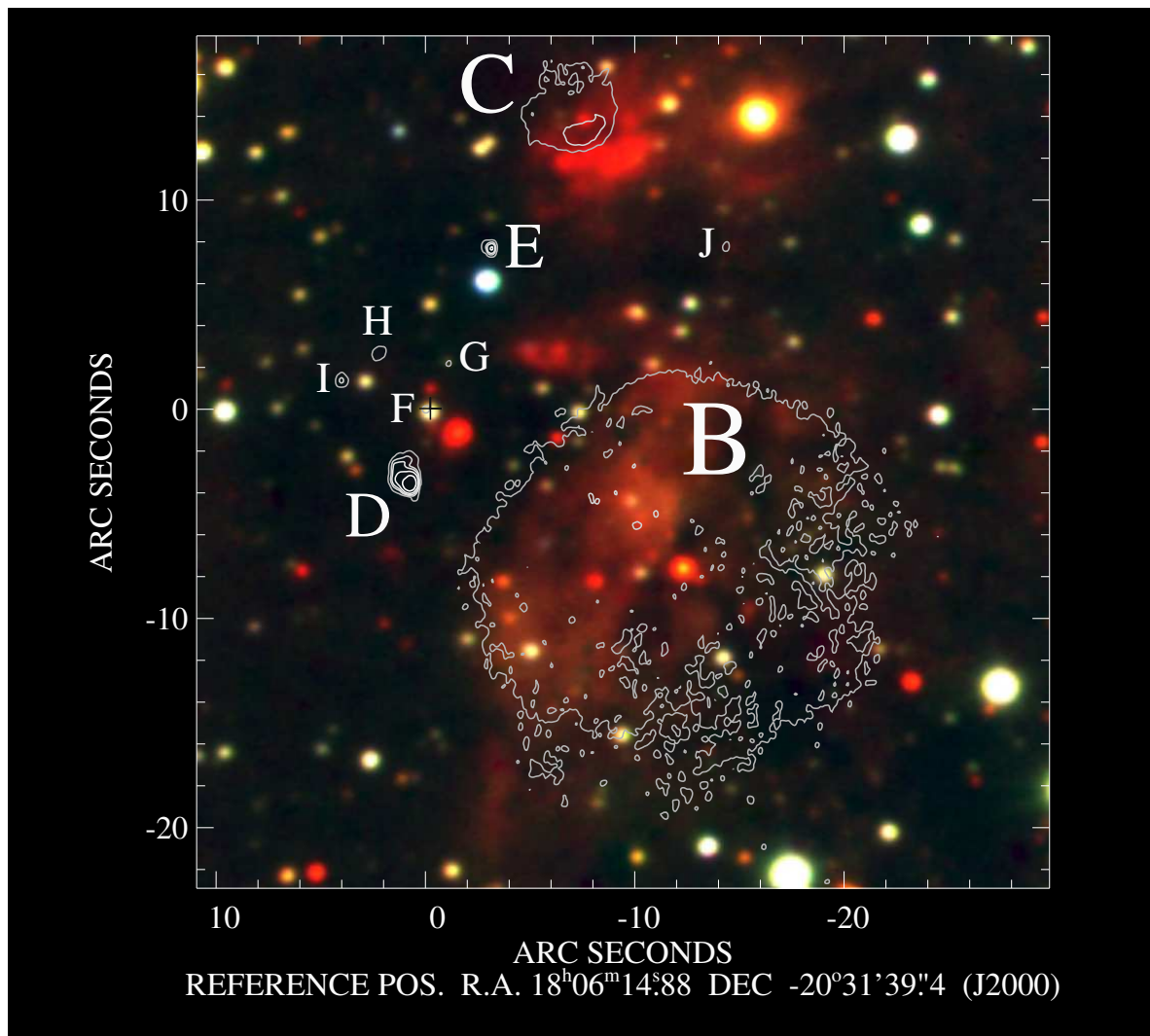


**Figure 3.3:** Cutout of the central region of Fig. 3.1. The overlaid contour lines denote the 3.6 cm emission of the ionized regions as measured by Testi et al. (2000). The source annotation follows their nomenclature. Note that also component F features weak 3.6 cm emission – the related contour line merges with the seeing disk of the yellow star. The black cross marks the peak of the  $\text{NH}_3(5,5)$  HMC emission (Hofner et al. 1994).

The HMC component F was originally defined as the peak in  $\text{NH}_3(5,5)$  and  $\text{NH}_3(4,4)$  transition measurements, conducted with the VLA (Hofner et al. 1994, Cesaroni et al. 1994). The black plus sign in Fig. 3.3 pinpoints the peak position of this molecular line emission. (In Fig. 3.4 we overlay the contours of the HMC  $\text{NH}_3(5,5)$  emission onto the NIR data for comparison.) Further radio–interferometric observations revealed emission peaks in the 2.7 mm dust continuum (Hofner et al. 1996) as well as in the cm free–free continuum (Testi et al. 2000) at the position of the HMC component F. Testi et al. (1998) reported a K–band detection at the coordinates of the HMC. Our near–infrared imaging reveals an intriguing structure in this HMC region which one can decompose into at least three distinct objects. We refer to Fig. 3.5 for the numbering we have chosen for the objects, which will be used in this thesis. On the basis of our high–resolution VLT data (pixel scale =  $0''.15/\text{px}$ , seeing  $0''.55$ ) one can presume that this previous K–band observation of Testi (pixel scale =  $0''.92/\text{px}$ )

was suffering from the lower resolution and confusion among the objects in that line of sight which can now be clearly separated. In Appendix A we discuss in detail our approach for deriving an accurate astrometry for our data.

Near the HMC peak coordinates, we find a “red” compact source according to the 3-colour-composite (object F1 in Fig. 3.5). However, F1 does not coincide with the hot core peak F, but is displaced by 1.7 arcsecs. Although this suggests that the compact NIR emission F1 is not a direct trace of the innermost HMC region but a distinct object we should note that according to Cesaroni et al. (1994) the warm ammonia emission is extended over several arcsec and a source size of 3 – 5 arcsec was derived. Since 1 arcsec translates to 0.028 pc (assuming a distance of 5.7 kpc) F1 might still be affected by warm and dense molecular gas of the actual HMC. Thus, we have derived the  $K_s$  band magnitude of object F1 using S234–E ( $K_s = 12.070$  mag) and S071–D ( $K_s = 11.839$  mag) (Persson et al. 1998) as photometric standards. By performing PSF photometry on the mosaicked science frame we derived a count rate for our object. To be in accordance with the 10'' aperture photometry applied by Persson et al. (1998) we also used this method (in form of the *MIDAS*<sup>1</sup> MAGNITUDE/CIRCLE routine) to derive the count rates for the standard stars. According to this procedure the F1 magnitude is  $K_s = 13.6$  mag with 0.1 mag as a conservative error limit. Testi et al. (1998) had derived  $K = 12.9 \pm 0.08$  mag, probably for all the 3 objects visible at 2.16  $\mu\text{m}$  in the F region in Fig. 3.5.

At the position of the HMC 3.6 cm radio peak we find another much fainter compact source (object F2 in Fig. 3.5). To evaluate this one should remember that this area near the IRDC is in general very extinguished. It is possible to derive a preliminary extinction estimation for this region from the data contained in Schlegel et al. (1998) which results in  $A_\lambda$  values between 31.2 mag (J band) and 12.7 mag (K band). Therefore, other objects in the F region appear to be strongly reddened, with (H–K) values clearly exceeding 1.5 mag. However, this object has a “yellow” colour index with (H–K) being only 0.72 mag. By inserting the data for F2 into a J–H– $K_s$  two-colour diagram we see that the F2 colours can be explained almost completely by interstellar reddening. Therefore, we conclude that F2 is a foreground star, not physically related to the star-forming region. A definitive answer cannot be given until high-resolution NIR spectroscopy is performed with an instrument capable of resolving the objects in the HMC region (e.g., NACO on the VLT).

A third very faint source (object F3) is visible less than 1'' to the north of the foreground star. This object appears very red because it is only detected in the  $K_s$  band and not in the J or H band. Note that, according to our astrometry, an  $\text{H}_2\text{O}$  maser (the first one in the  $\text{H}_2\text{O}$  maser list in Table 3.1) is only 0.25 arcsec apart from the position of this object.

The photometry of the objects in the HMC region is summarised in Table 3.2.

---

<sup>1</sup>Munich Image Data Analysis System

**Table 3.1:** Compilation of positions of features in the HMC region

Feature	RA(J2000)	DEC(J2000)	Telescope
NH <sub>3</sub> (4,4)	18 06 14.85	-20 31 38.91	VLA – D <sup>(1)</sup>
NH <sub>3</sub> (4,4)	18 06 14.81	-20 31 39.41	VLA – C <sup>(1)</sup>
NH <sub>3</sub> (5,5)	18 06 14.87	-20 31 39.41	VLA – C <sup>(2)</sup>
CH <sub>3</sub> CN(6-5)	18 06 14.89	-20 31 39.20	OVRO <sup>(3)</sup>
2.7 mm cont.	18 06 14.89	-20 31 38.90	OVRO <sup>(3)</sup>
3.6 cm cont.	18 06 14.88	-20 31 39.37	VLA – BnA <sup>(4)</sup>
H <sub>2</sub> O masers	18 06 14.88	-20 31 38.39	VLA – B <sup>(5)</sup>
	18 06 14.87	-20 31 41.21	
	18 06 14.81	-20 31 37.43	
	18 06 14.93	-20 31 41.55	
	18 06 14.86	-20 31 40.59	
	18 06 14.78	-20 31 34.71	
	18 06 14.87	-20 31 37.57	
	18 06 14.67	-20 31 31.44	
	18 06 14.98	-20 31 42.53	
object F1	18 06 14.78	-20 31 40.48	ISAAC <sup>(6)</sup>
object F2 (K <sub>s</sub> )	18 06 14.87	-20 31 39.50	ISAAC <sup>(6)</sup>
object F3	18 06 14.87	-20 31 38.39	ISAAC <sup>(6)</sup>
object F4 (nb_M)	18 06 14.85	-20 31 39.70	ISAAC <sup>(6)</sup>

References: (1) Cesaroni et al. (1994), (2) Hofner et al. (1994), (3) Hofner et al. (1996), (4) Testi et al. (2000), (5) Hofner & Churchwell (1996), (6) this thesis

### 3.2 L' and nb\_M band data

This wavelength range is interesting because it fills the gap between the K<sub>s</sub> and the N band. Naturally, the signals of most of the NIR–blue field stars strongly fade and finally disappear. Hence, they do not cause confusion anymore. Still, enough objects remain in the FOV of ISAAC to perform accurate astrometry. Here we want to direct the attention to an interesting detail (see Fig. 3.5).

In the K<sub>s</sub> band image one can clearly see the presence of three objects in the HMC region F. The “red” object F1, already mentioned in Sect. 3.1, is dominant. The object F2 which we estimated to be an unrelated foreground star is almost 1.7 arcsec away in the north–east direction. Above this we detect the third very red and weak source F3. Please note that the location of the foreground star is underlaid with weak and diffuse emission.

When we now switch to the L' band we notice that the point–like star F2 in the middle has almost totally disappeared. Instead, we now clearly see emission arising from a slightly different location, which reveals the presence of another object F4. This is evident, when we

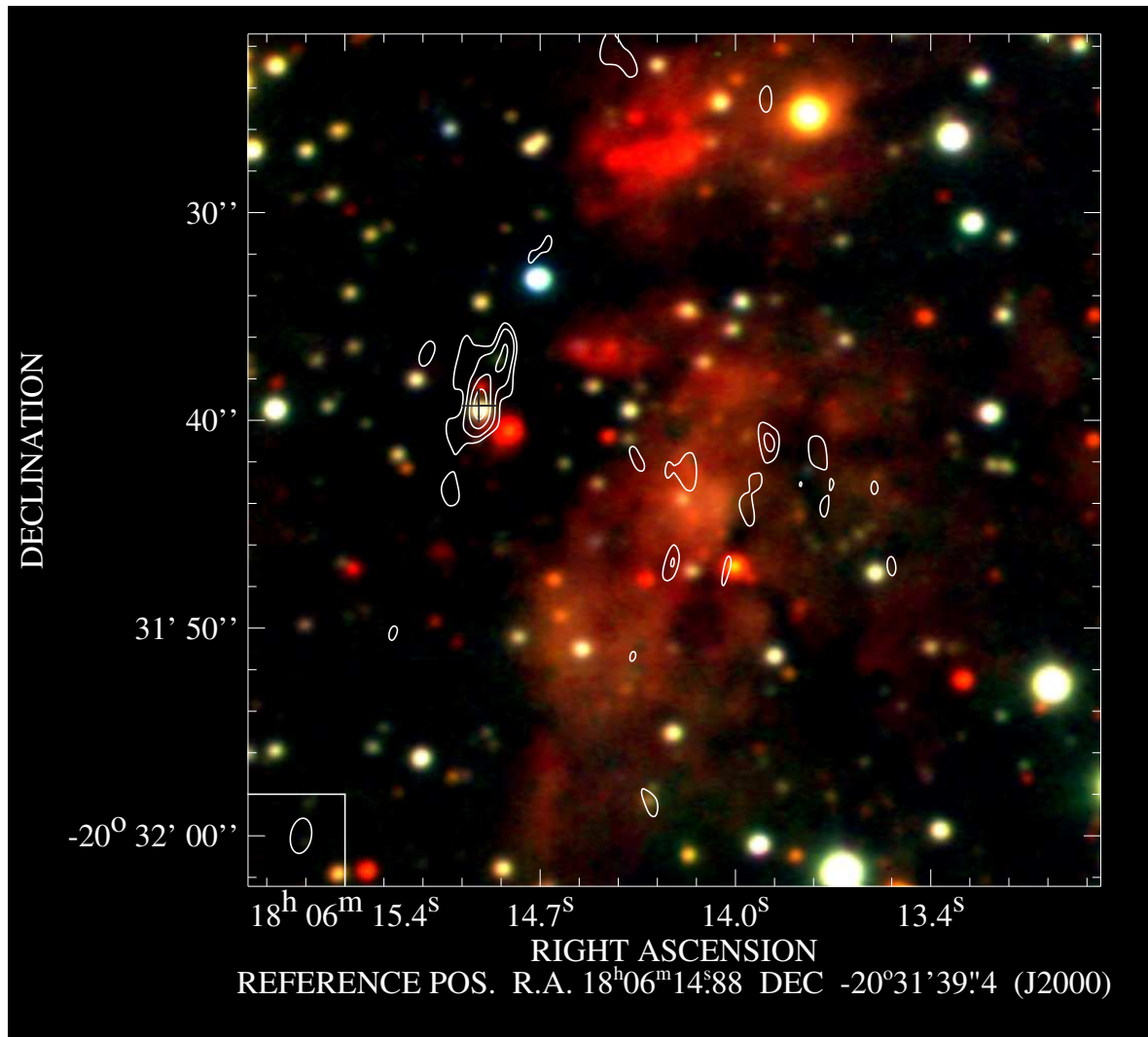


**Figure 3.4:** The same field of view as in Fig. 3.3, but now the overlaid contour lines trace the thermal  $\text{NH}_3(5,5)$  emission of the HMC as measured by Hofner et al. (1994). The ellipse in the lower left corner indicates the size of the synthesised VLA beam. The black cross at the reference position marks the faint peak of the 3.6-cm HMC emission (Testi et al. 2000).

compare the relative positions of the emission centres. We mentioned the distance of 1.7 arcsec between the point-like star F2 and the “red” object F1 in the  $K_s$  band. The centre of F4 in the L’ band image is clearly shifted compared to the F2 position; it is now only 1.3 arcsec away from object F1. This shift is persistent also in the nb\_M band image; it is a small effect, but noticeable. In the following, the nature of F4 will become clearer.

### 3.3 N and Q band data

Fig. 3.6 shows the central part of Fig. 3.1 but now at  $\lambda = 11.7 \mu\text{m}$  obtained with *SpectroCam-10*. To amplify the morphological structure, we applied 25 iterations of a modified Maximum Entropy Method for noise suppression, based on the wavelet transform and developed by

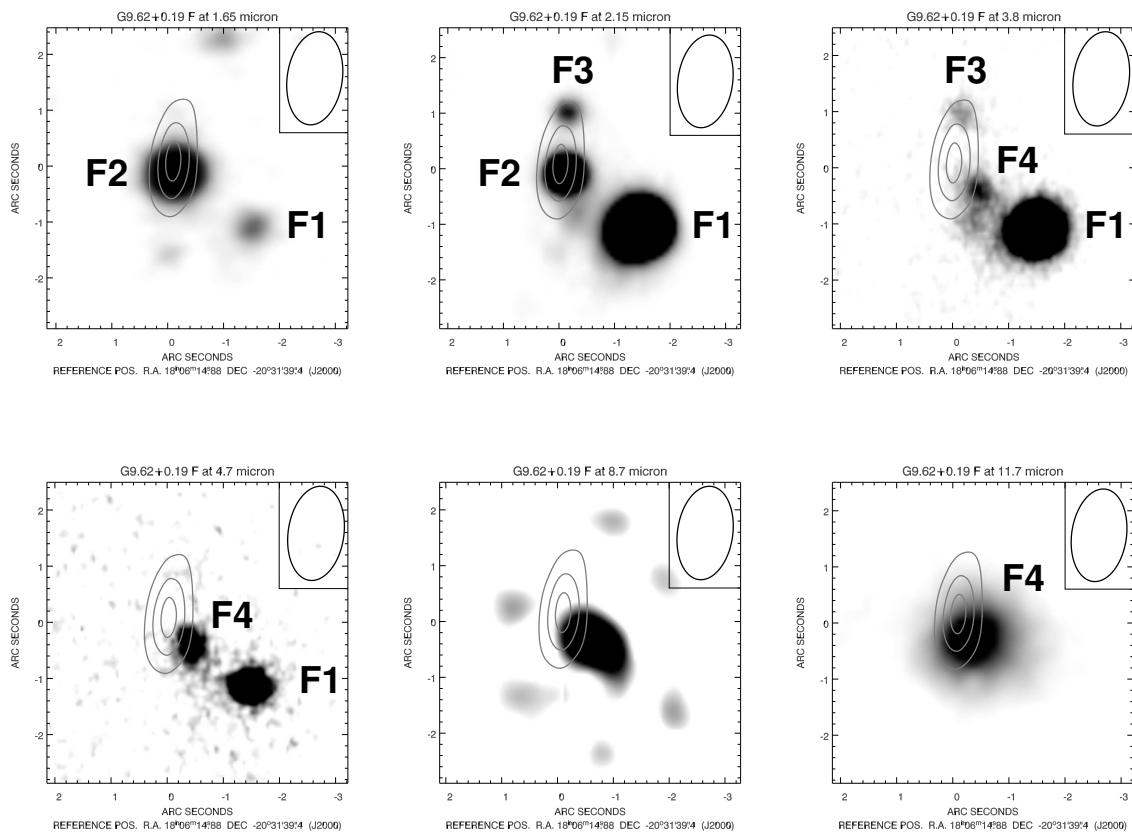


**Figure 3.5:** Cutout gallery showing the four objects of the HMC region G9.62+0.19–F. Upper row from left to right: H,  $K_s$ , L band. Lower row from left to right: nb\_M, N1,  $11.7 \mu\text{m}$ . The size of the cutout box is ca.  $5''.4 \times 5''.4$ . While the foreground star (F2) quickly fades towards longer wavelengths, another object very close to it (F4) gets stronger and finally dominates the region. We presume that it is a potential trace of the HMC whose location is here indicated by the upper contours of the  $\text{NH}_3(5,5)$  emission. While all the other images are taken from the plain imaging data, the N1 image at  $8.7 \mu\text{m}$  shows the *TIMM12* data after deconvolution with the standard star HD169916. Note that the smaller spots in that particular image are deconvolution artefacts that change their position and strength when the deconvolution parameters are varied.

Pantin & Starck (1996). The extended emission coming from component B is also dominant in the mid–infrared. A second, but compact source is found near the extended B component. The accurate position and hence the correct interpretation of this compact source has been a matter of debate during recent years (cf. De Buizer et al. 2000, 2003, Stecklum et al. 2002a, Persi et al. 2003). In Appendix B we describe the circumstances and explain the result of our new astrometry. We find that the compact MIR emission is coming from the HMC region, contrary to the results of De Buizer et al. (2003). We identify it with object F4 (see Fig. 3.5), i.e., with the HMC counterpart.<sup>2</sup> For a determination of the flux coming from the compact source F4, we observed the star  $\delta$  Oph just before we imaged the G9.62+0.19 region. This isolated star is a strong *IRAS* source with a  $12 \mu\text{m}$  flux of 149.7 Jy. Carrying out aperture

<sup>2</sup>Persi et al. (2003) also identified the MIR source with the HMC on the basis of low signal–to–noise data and related it to the K band emission found by Testi et al. (1998). However, they apparently underestimated the significance of the multiplicity of objects in the G9.62+0.19–F region and thus could not distinguish between F1 (dominant in the K band) and F4 (dominant in the N band).

photometry for the compact source (using a 3 arcsec diaphragm) and the photometric reference star, we derived a flux of  $(0.60 \pm 0.10)$  Jy for F4.

The  $8.7 \mu\text{m}$  N1 data proved their value especially for the MIR astrometry, as shown in Appendix B. We show these data in Fig. 3.7. To produce this image the matrix restoration method described in Appendix C was applied to the N1 band *TIMMI2* data. Thereafter, the restored data were overlaid as contours on the NIR colour composite. As can be easily seen, they comprise a much larger field of view than the *SpectroCam-10* data in Fig. 3.6. We also derived the flux of the compact MIR emission at this wavelength of  $8.7 \mu\text{m}$ . As is evident in Fig. 3.7 and Fig. 3.5, the emission is elongated; most of the flux stems from object F4, but object F1 might still contribute a small fraction to the total signal. We did not try to disentangle F4 and F1 and only measured the total flux with an adequately sized aperture for the photometry. One should keep in mind that the N1 filter covers a prominent PAH feature, the related emission also peaks around  $8.6 - 8.7 \mu\text{m}$  (e.g., Peeters et al. 2002b). In fact, such PAH emission seems to be a common feature of the majority of compact H II regions and their surroundings (Peeters et al. 2002a).<sup>3</sup> Thus, the measured N1 flux is probably affected by additional contributions from those small PAHs that are susceptible to transient heating and often attain a higher (non-equilibrium) temperature than the larger normal dust grains. Indeed, the N1 flux of  $(1.10 \pm 0.10)$  Jy is higher than the  $11.7 \mu\text{m}$  flux of F4.

Although the atmospheric conditions during the Q2 band observations at  $18.75 \mu\text{m}$  were not photometric we tentatively report the measured flux of  $(22.8 \pm 7.0)$  Jy for the compact emission blob we assume to be identical to F4 – no other reference objects appeared in the data except for the extended emission of component B. The quoted relatively high uncertainty of 30 % is mainly caused by the non-perfect sky.

All the MIR measurements are also included in the SED plot of object F4 in Fig. 3.10 and draw an enlightening picture of the energetics of the HMC. In Sect. 3.6 we will further elaborate on the consequences of our findings for object F4.

### 3.4 $H_2$ and $Br \gamma$ narrow-band imaging data

In Fig 3.8 we combined the  $Br \gamma$  data (blue channel) and the  $H_2$  data (red channel). The average of the signal of the two filters was put into the green channel. The  $Br \gamma$  emission of the compact HII region B clearly dominates the overall appearance of the star-forming complex. The ultra- and hypercompact HII regions D and E are not visible at all due to the large K band extinction towards these components (see Sect. 3.8 for a discussion). More interesting, the signal arising from the region of the radio C component appears almost white in this colour composite; thus, it represents just the contribution of the K band continuum without strong  $H_2$  or  $Br \gamma$  line emission. We find the same for the NIR objects around the HMC region F.

The  $H_2$  data reveal a compact emission region located between the components B and

<sup>3</sup> We mention our experience with another massive star-forming region (Apai et al. 2005) where PAH emission (also covered by the MSX A band) clearly affects the SED of the central object.



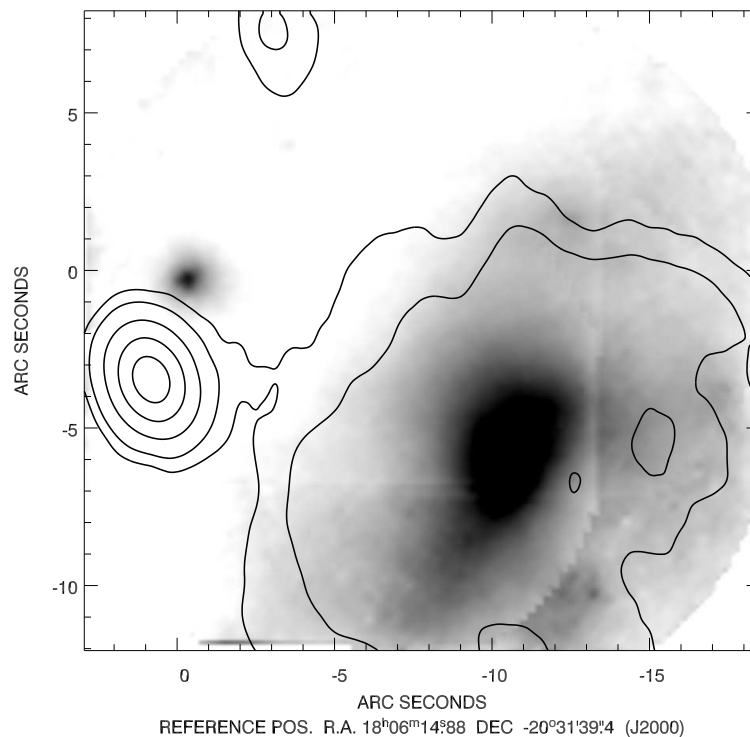


**Figure 3.6:** Inverse grey-scale representation of the 11.7  $\mu\text{m}$  *SpectroCam-10* image displaying a smaller cutout of the G9.62+0.19 region. The weaker but nevertheless clearly visible spot to the east represents emission from the region of the HMC component F and arises probably from object F4 (see also Fig. 3.5). Overlaid are the 1.3 cm continuum VLA contours from Cesaroni et al. (1994). The compact radio source to the south-east of the compact MIR emission is the UCHII region G9.62+0.19 D.

C. It appears as a flat ellipsoid with a large axis of about 5'', but it is broken up into several emission maxima and minima. This feature was also mentioned by Persi et al. (2003) and we report here the positions of the two main components according to our astrometry.<sup>4</sup> Component 1:  $\alpha_{2000} = 18^{\text{h}}06^{\text{m}}14^{\text{s}}.42$ ,  $\delta_{2000} = -20^{\circ}31'36''.8$ , Component 2:  $\alpha_{2000} = 18^{\text{h}}06^{\text{m}}14^{\text{s}}.34$ ,  $\delta_{2000} = -20^{\circ}31'36''.8$ . The projected distance to the hot core region F is roughly 7 arcsec (i.e. 0.2 pc if assuming  $d = 5.7$  kpc). In principle, such a distance would allow an association with the molecular outflow arising from component F (Hofner et al. 2001). One problem is that the outflow is well aligned along the line-of-sight. Thus, if the interpretation of shock excitation due to interaction with the outflow holds, then the outflow driving source and the H<sub>2</sub> emission region cannot be located in the same plane of the sky, implying that the latter might be detached from the actual star-forming complex G9.62+0.19. Another possibility is the existence of another outflow in this region that was not detected in previous studies (Hofner et al. 1996, 2001). An alternative consideration would be that a considerable fraction (if not all) of the detected H<sub>2</sub> emission is in fact fluorescence, excited by UV photons of the nearby HII regions (e.g., Black & van Dishoeck

<sup>4</sup> For the probable cause of the astrometric disagreement between our positions and the one of Persi et al. (2003) we refer to the end of Appendix A.

**Table 3.2:** Measured IR fluxes in Jy (corresponding magnitudes in parenthesis) for the objects in the HMC region

Band name	object F1	object F2	object F3	object F4
J	–	$2.21 \times 10^{-4}$ (17.15)	–	–
H	$6.19 \times 10^{-5}$ (18.00)	$5.25 \times 10^{-4}$ (15.72)	–	–
K <sub>s</sub>	$2.25 \times 10^{-3}$ (13.60)	$6.57 \times 10^{-4}$ (15.00)	$1.67 \times 10^{-4}$ (16.49)	–
L'	$2.43 \times 10^{-2}$ (10.04)	–	$1.00 \times 10^{-3}$ (13.50)	$2.95 \times 10^{-3}$ (12.33)
nb_M	$3.10 \times 10^{-2}$ (9.21)	–	–	$1.49 \times 10^{-2}$ (10.01)
N1	1.10 (3.90) <sup>a</sup>	–	–	1.10 (3.90) <sup>a</sup>
N4	–	–	–	$6.00 \times 10^{-1}$ (4.55)
Q2	–	–	–	$2.28 \times 10^1$ (–0.85) <sup>b</sup>

<sup>a</sup> In the undeconvolved N1 band data, the objects F1 and F4 merge into one entity, whose combined flux is reported.

<sup>b</sup> Note that the Q2 flux is affected by a relatively large uncertainty of around 30% due to non-photometric sky conditions (see text).

1987 and Draine & Bertoldi 1996 for a theoretical treatment; e.g., Fernandes et al. 1995 and McCartney et al. 1999 for observational evidence for other astronomical objects). The components B or C could act as UV photon donor. Only further spectral analysis, comprising several H<sub>2</sub> roto-vibrational transitions, can distinguish between the collisional shock model and the fluorescence model. However, we mention that the H<sub>2</sub> feature is not a pure emission line object, we also see diffuse continuum emission from this position in the L' and nb\_M band, as well as in the 2.09 μm filter used for the polarimetric imaging (see the next paragraph).

### 3.5 K narrow-band imaging polarimetry

The polarimetric data were combined to generate a map of the linear polarisation of G9.62+0.19. We chose the standard approach for obtaining the polarimetric quantities, using the four intensities measured with the Wollaston prism (see Sect. 2.2.2). The Stokes parameters can be defined as:

$$Q = I(0^\circ) - I(90^\circ), \quad (3.1 \text{ a})$$

$$U = I(45^\circ) - I(135^\circ), \quad (3.1 \text{ b})$$

$$I = (I(0^\circ) + I(90^\circ) + I(45^\circ) + I(135^\circ))/2. \quad (3.1 \text{ c})$$

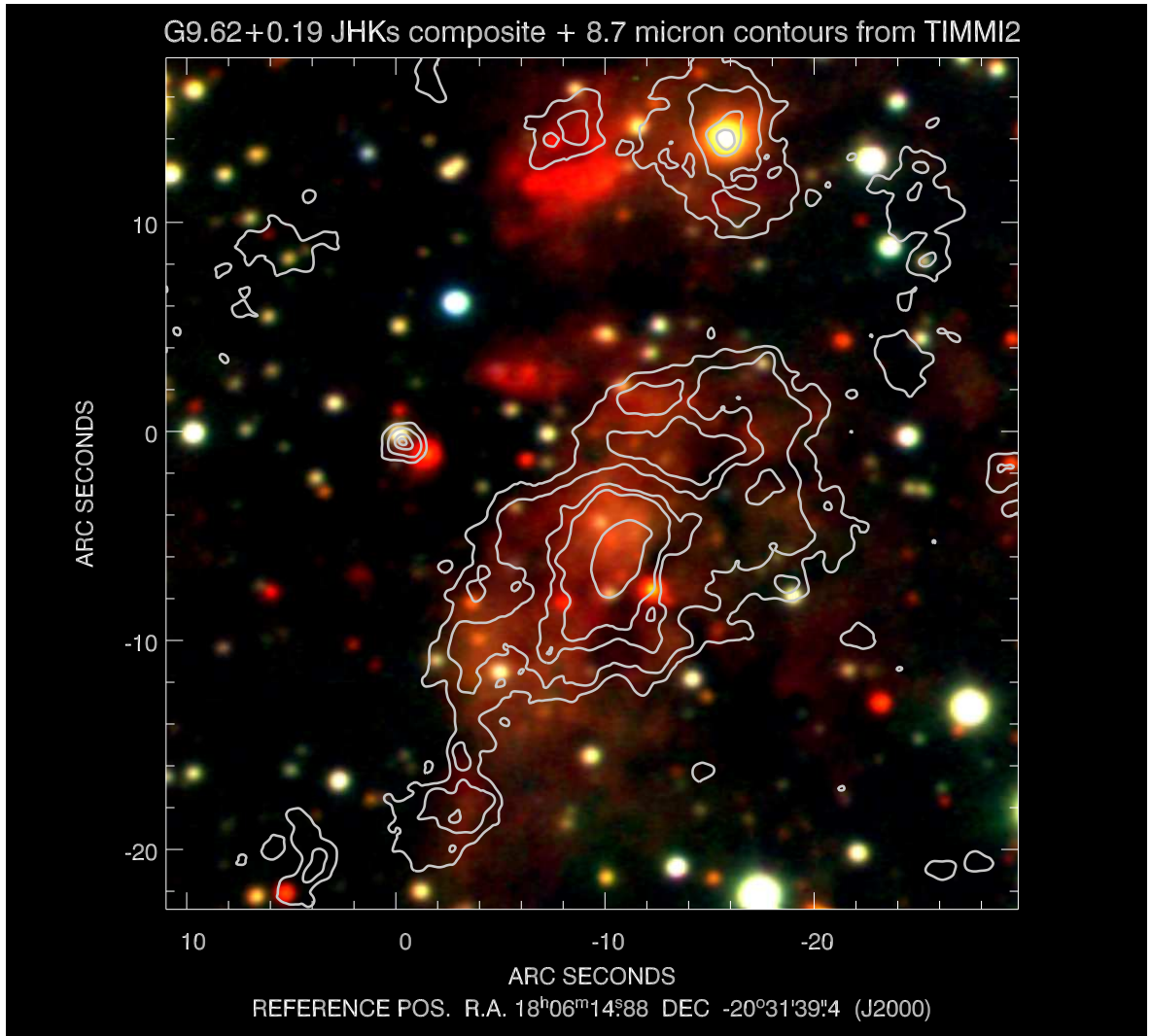


**Figure 3.7:** The JHK<sub>s</sub> colour composite, overlaid with the *TIMMI2* N1 band data as contours. The bright source at the offset coordinates (−16, 14) served as main astrometric reference for the *TIMMI2* data.

The degree of linear polarisation ( $p_{\text{lin}}$ ) and the respective polarisation angle ( $\Theta_{\text{lin}}$ ) can then be derived by using:

$$p_{\text{lin}} = \frac{\sqrt{Q^2 + U^2}}{I} \quad \Theta_{\text{lin}} = \frac{1}{2} \arctan \frac{U}{Q}. \quad (3.2)$$

In Fig. 3.9 we show the resulting polarisation map superimposed on the Stokes- $I$  image (see Eq. (3.1 c)) derived from the very same data set. We mention that the degree of linear polarisation as derived from Eq. (3.2) poses an upper limit for the true value of  $p_{\text{lin}}$  because of the non-standard error distribution of this quantity (e.g., Simmons & Stewart 1985). Thus, before plotting we debiased  $p_{\text{lin}}$  using the approach given in the appendix to the paper of Wardle & Kronberg (1974).

NIR imaging polarimetry of circumstellar matter proved to be a valuable tool for revealing the illuminating source, even in cases where it is hidden from the direct view due to enhanced extinction (e.g., Tamura et al. 1991, Yao et al. 2000, Henning et al. 2002a, Stecklum et al. 2003). In the north-west of Fig. 3.9, we find two adjacent regions of strongly enhanced lin-

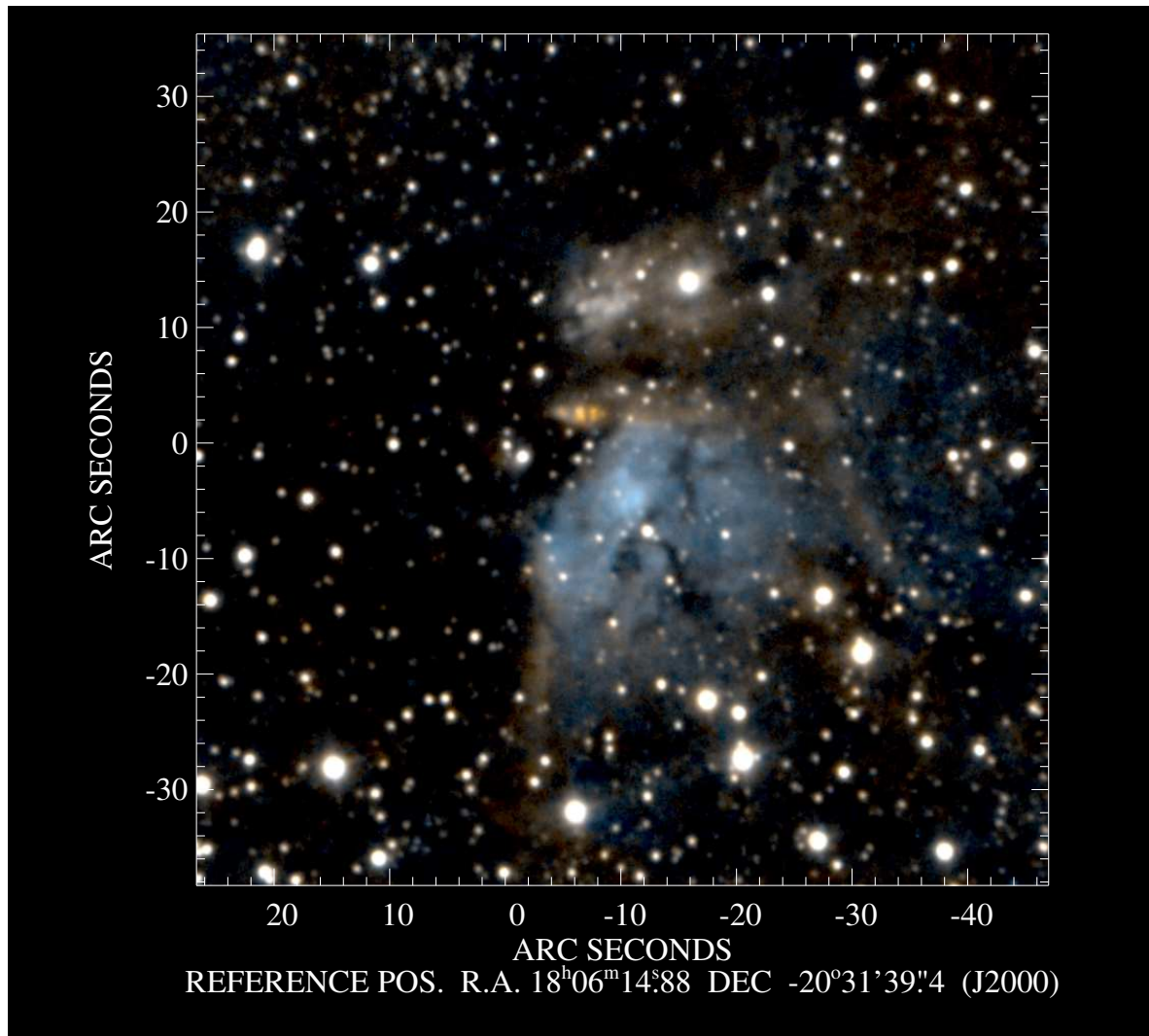


**Figure 3.8:** This image shows G9.62+0.19 in the K narrow-band filters: Br  $\gamma$  (blue), H<sub>2</sub> (red), (Br  $\gamma$  + H<sub>2</sub>)/2 (green). The Br  $\gamma$  emission arises mainly from the compact HII region G9.62+0.19 B. Note that the H<sub>2</sub> emission blob roughly in the image centre has its own substructure. The diffuse emission to the north of it (white) turns out to be mainly scattered light (see Fig. 3.9).

ear polarisation, covering the positions of component C (cf. Fig. 3.3) and of the H<sub>2</sub> emission feature (cf. Fig. 3.8). The debiased polarisation degree partly exceeds 50 %, indicative of single-scattering events. At first glance, the arrangement of the polarisation vectors implies a common illuminator for both regions which seems to be located south-east of them towards the more obscured region of the neighbouring IRDC (see Fig. 3.1). The ellipse in Fig. 3.9 indicates the  $1\sigma$  confidence region where the illuminator is probably located. It is derived by tracing the intersections of lines perpendicular to the polarisation vectors where we only took the vectors with  $p_{\text{lin}} > 20\%$  into account. The most probable location of the illuminator is the centre of mass (CoM) of the intersection points, whereas their distribution yields an error estimate. A 2-dimensional Gaussian is fitted to the distribution of intersection points; the computed  $\sigma$  parameters, which define the fitted Gaussian, are used as axes of the plotted ellipse (Weintraub & Kastner 1993, Stecklum et al. 2003). The ellipse is quite eccentric

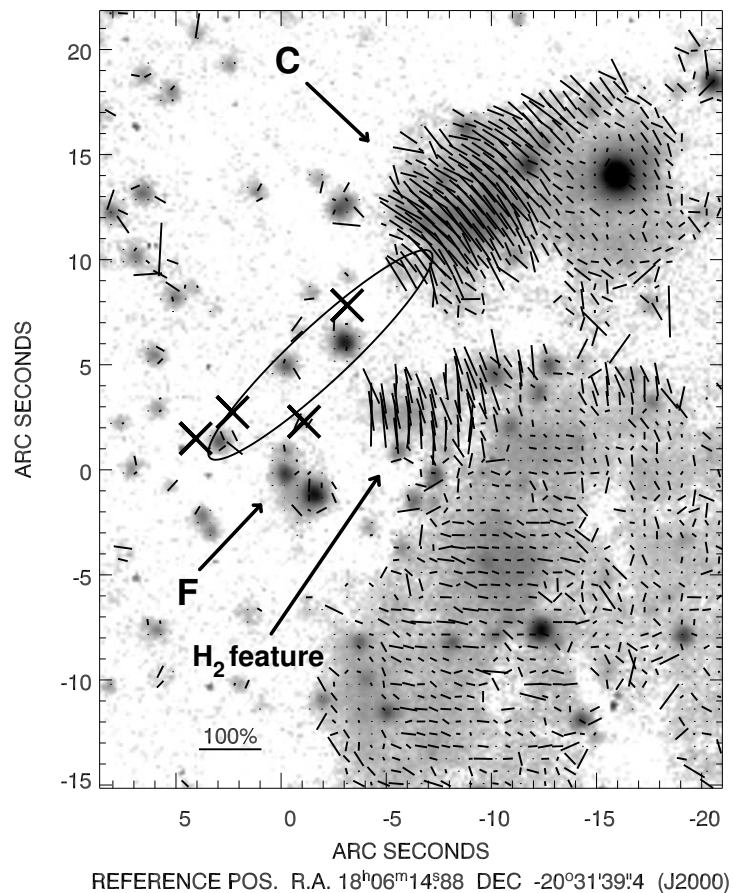


**Figure 3.9:** Polarisation map overlaid over an image of Stokes- $I$  (i.e. the intensity) of G9.62+0.19, both measured at  $2.09 \mu\text{m}$ . We binned the data to a pixel size of  $0''.6 \times 0''.6$  before deriving the polarisation. The ellipse is an indicator for the location of the illuminator whose scattered light causes the high degree of linear polarisation in some parts of the image (see Sect. 3.5 for details). The thick crosses mark the positions of the hypercompact HII regions E, G, H, and I (cf. Fig. 3.3).

because the available polarisation vectors lie in only 2 of the 4 image quadrants. When looking carefully at the polarisation pattern one sees that the polarisation vectors related to the H<sub>2</sub> feature are oriented more or less north–south. Hence, when judging by eye, one would expect the centre of mass of all intersection points to be located more to the south–east of the plotted ellipse. An explanation for the different location in the plot (Fig. 3.9) is that we can use some 180 polarisation vectors near region C for the CoM estimation. But there are only some 30 vectors from the H<sub>2</sub> feature region that fulfill the conditions of sufficiently high degree of polarisation and acceptable signal–to–noise ratio in the intensity image. Thus, the polarisation vectors around component C will contribute far more intersection points than the vectors of the H<sub>2</sub> feature and hence will simply “preponderate” in the CoM estimation. Is this a hint that there are several illuminating sources? We mention that the error  $\Delta p$  is still around 8 % in the high polarised regions. For ratios  $p/\Delta p > 3$  the typical error for the position angle can be approximated by  $28.65^\circ \times \Delta p/p$  (Serkowski 1962). This results in

an error of  $4^\circ - 9^\circ$  in our case. But this is of course a statistical error. It could not explain the coherent rotation of the whole polarisation pattern in one part of the image (i.e., the  $H_2$  feature region). The bottom line of these considerations is: The observed polarisation map does not fully correspond to one coherent circularly symmetric pattern as expected in the case of only one illuminating object, thus indicating the possibility of a second illuminator. The radio object E (Fig. 3.3) is situated inside the ellipse in Fig. 3.9 and is an illuminator candidate, at least for the scattered light near component C. However, the position of E does not really fit the polarisation pattern of the  $H_2$  feature. We mention that the hypercompact radio components G, H, and I (Fig. 3.3), whose nature is not yet clarified, are located very near the  $1\sigma$  confidence region for the illuminator position and their respective positions are in better agreement with the polarisation pattern of the  $H_2$  feature. Thus, one of these sources might be responsible at least for the illumination of the  $H_2$  feature. Since we do not see clearly corresponding NIR counterparts for these objects, they are probably deeply embedded. Should one of these objects turn out to be an illuminator, this would have implications for the distribution of its circumstellar material. A pronounced asymmetry of the ambient matter distribution would be necessary to explain how the object is able to illuminate the highly polarised regions in the K band, while we do not detect any K band emission from it in our line of sight.

The K narrow-band and polarisation data of component C prove their importance also regarding the general astrometry of the region. In Fig. 3.3 we see that for component C the overlaid VLA contours of the UCH<sub>II</sub> region are shifted from the NIR counterpart. One could suspect an error in the overall astrometry, if one interprets this K band emission either as arising from Br  $\gamma$  emission of the ionised gas and/or as thermal emission from hot dust, which usually is well mixed with the ionised gas of the outer parts of an UCH<sub>II</sub> region. (A dust-free cavity might exist in the inner part, though.) Our data show that the Br  $\gamma$  fraction of the K band signal of component C is marginal and that the dominant part of this radiation probably consists of scattered light. Under these circumstances, there is no reason why the cm continuum contours should match the near-infrared emission.

### 3.6 What is the nature of the IR objects in the HMC region?

In the previous sections we could establish the newly discovered object F4 as the actual HMC infrared counterpart by means of thermal and mid-infrared observations and careful astrometry. In this section we discuss the consequences that arise from this finding. Some more theoretical considerations will help to support our view.

#### Radiative transfer computations

To understand the properties and unusual features of the G9.62+0.19-F hot core we performed some basic continuum radiative transfer computations, utilising two self-consistent

radiative transfer codes (Manske & Henning 1998, Wolf et al. 1999). For this thesis we will only consider spherically symmetric models, in accordance with the standard description of hot molecular cores (e.g., Osorio et al. 1999), just to demonstrate the limitations of this concept in the case of our HMC. As input parameters we used data from Hofner et al. (1996). They had limited the spectral type of the central source to be B0.5 – B1. The luminosity was estimated to be  $\approx 1.8 \times 10^4 L_{\odot}$  (see also Cesaroni et al. 1994). The mass is not well constrained by other authors, but ranges between 55 and 160  $M_{\odot}$  (Hofner et al. 1996). Several power laws for the radial density gradient were applied ( $\rho \sim r^{-\alpha}$  with  $\alpha = 0.0 \dots 2.0$ ). As grain material a mixture of silicates (Dorschner et al. 1995) and carbonaceous materials (Preibisch et al. 1993) was used. The computed fluxes comprise the range of  $10^{-8} - 10^{-4}$  Jy for  $\lambda = 2.2 \mu\text{m}$  and  $10^{-4} - 5 \times 10^{-1}$  Jy for  $\lambda = 11.7 \mu\text{m}$ , respectively, and thus are at or below the detection limit of ISAAC, while the situation for *SpectroCam-10* at  $11.7 \mu\text{m}$  is more relaxed. While parameter combinations could be found that more or less fit the observational data points for F4 beyond  $10 \mu\text{m}$ , it was not possible to also fit the data up to  $5 \mu\text{m}$ .

In Fig. 3.10 we show the result of such a radiative transfer computation and compare it with the measured fluxes of the objects F1 and F4 mentioned in Sects. 3.1, 3.2, and 3.3. The particular parameter set used for Fig. 3.10 was chosen to produce preferably high fluxes in the  $2 - 5 \mu\text{m}$  range. However, the synthetic SED should still be in accordance with the data points at longer wavelengths. For these points, the best fit was reached with a constant density distribution, an outer radius of 2600 AU, a total luminosity of  $1.88 \times 10^4 L_{\odot}$ , and a dust mass of  $0.94 M_{\odot}$  inside the model space (see Fig. 3.10). The optical depth for this particular configuration was  $\tau_v = 673$ . It becomes evident that the F4 emission in the  $2 - 5 \mu\text{m}$  range is still more than an order of magnitude stronger than predicted by the model. We interpret this as support for the idea that spherical symmetry is not applicable in the case of G9.62+0.19–F. However, a comprehensive two-dimensional modelling of the observed fluxes would be beyond the scope of this investigation.

To guide the eye, we added in Fig. 3.10 a modified blackbody curve to the radiative model SED that also fits quite well the data points at longer wavelengths. The effective temperature of such a modified blackbody would be 90 K, the wavelength dependence of the opacity is described by  $\kappa_m \sim \lambda^{-1.0}$  in our case. However, the significance of such a temperature estimation is questionable for the object class of HMCs. As shown, e. g., by Yorke (1980) and Yorke & Shustov (1981), the concept of an effective temperature and an effective radius is not well defined for very dense dusty envelopes around protostellar objects, they can strongly deviate from the blackbody or greybody nature. Furthermore, we should note that such an effective temperature might be misleading in the following regard. It was shown by means of simple radiative transfer considerations, e. g., by Schreyer et al. (1996) that the mass-averaged dust temperature, i. e., the temperature averaged over density and particle size distribution, is always lower ( $\Delta T = 15..30$  K) than the theoretical colour temperature derived from the SED for dense shells around massive YSOs. Thus, most of the mass in such a shell will attain a clearly lower temperature than implied by the colour temperature. This is important when using a temperature to derive dust masses from infrared

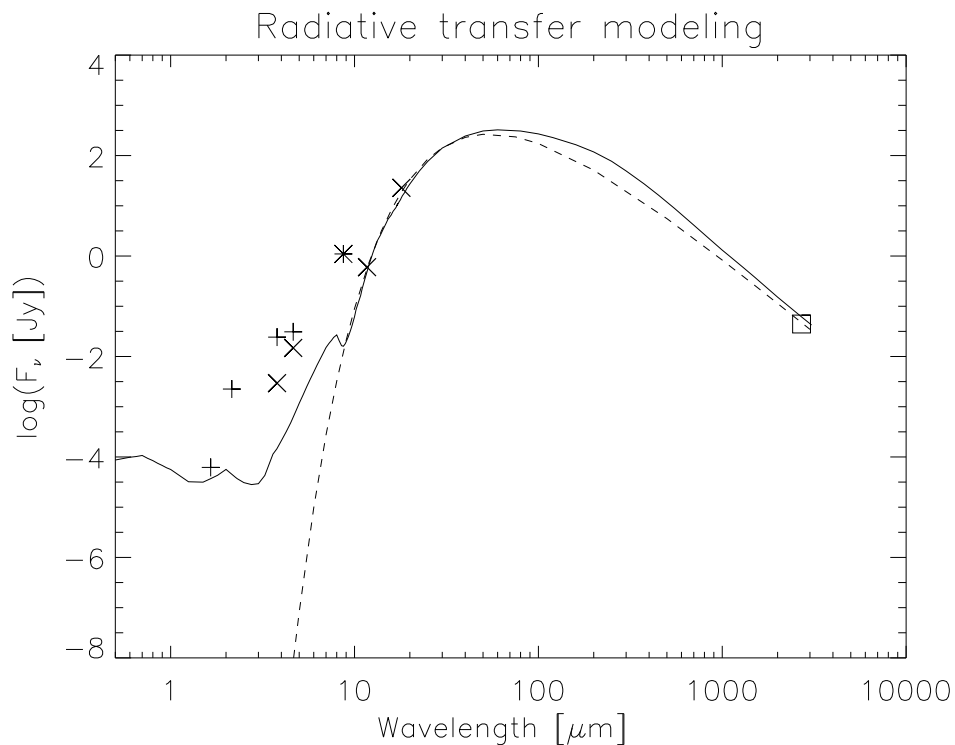


**Figure 3.10:** Example for the appearance of the SED of a hot molecular core, calculated with a radiative transfer model (solid line). For this graph we used a central heating source with  $T_{\text{eff}} = 22500$  K and a total luminosity of  $1.88 \times 10^4 L_{\odot}$ . The total mass contained in the model space was  $95 M_{\odot}$ . For this particular model we assumed a constant density distribution and an outer radius of 2600 AU. No accretion luminosity was added. The drawn-in symbols indicate the fluxes we measure for the objects F1 (plus-signs) and F4 (crosses), respectively. The asterisk at  $8.7 \mu\text{m}$  denotes the integrated flux from an area covering both F1 and F4. The 2.7 mm flux from Hofner et al. (1996) is marked by a small square. As comparison, a 90 K modified blackbody is plotted as a dashed line. However, the significance of such a temperature is put into perspective in Sect. 3.6.

or mm observations.<sup>5</sup>

The estimated luminosity of  $1.88 \times 10^4 L_{\odot}$  from our simple model is in good agreement with previous predictions (Cesaroni et al. 1994). When we also take into account the measured excess flux of F4 at shorter wavelengths (in comparison to the radiative transfer models and the modified blackbody approximation) we gain another  $1000 L_{\odot}$ , which is certainly a lower limit since we have not applied any extinction correction. Hence, the entire luminosity is approximately  $20\,000 L_{\odot}$ . This seems to prove that the HMC in G9.62+0.19-F indeed harbours a young high-mass star. However, caution is advisable, as we see in the case of the Orion Hot Core, where on a much smaller scale than in our case several infrared sources can be distinguished (Dougados et al. 1993), and the discussion about the energy budget of the individual sources has not settled yet (e.g., Gezari et al. 1998, 2003, Robberto et al. 2005).

<sup>5</sup>This result is recovered when dust temperature distribution functions are defined by integral relations and the dust mass is then derived by applying inversion methods (e.g., Li, Goldsmith & Xie 1999).



### 3.6.1 Hints from the polarimetry

The polarimetric data can provide additional information on the geometry of the observed regions. In a scenario where an outflow has opened the dense molecular shell of a molecular hot core, infrared radiation can escape through a channel of reduced density. The light will be scattered at the cavity walls (“dust mirroring”) which represent an increased column density of scatterers in the optically thin cavity environment (Yao et al. 1997, 2000). These single scattering events can lead to high degrees of linear polarisation (e.g., Fischer et al. 1996). Hence, we would expect to perceive a clear increase of NIR polarisation.

In contrast, the measured polarisation for object F1 is relatively low ( $10 \pm 5$  %), especially when it is compared to polarisation degrees in its immediate vicinity.<sup>6</sup> There, the polarisation increases up to ( $33 \pm 10$  %) in the small region of diffuse emission to the southwest of F2, but not including F2 or F1 (best to be seen in the  $2.16 \mu\text{m}$  image of Fig. 3.5 at the offset position  $(-0.3, -0.8)$ ). Based on the low-resolution NIR imaging of Testi et al. (1998), Hofner et al. (2001) suggested that object F1 itself represents infrared emission arising from the HMC region which might be cleared in parts by the molecular outflow. Taking our high-resolution infrared data, the improved astrometry and the results of the polarimetry into account, we no longer believe that this model can satisfactorily explain the properties of object F1.

However, this scenario is certainly a good interpretation for the diffuse emission behind the foreground star. It appears unlikely that this diffuse emission is just the result of the reflection of light coming from the foreground star F2. In such a case of backscattering the reflected light should more closely resemble the colour behaviour of the illuminating star. Moreover, there should be a tendency for a slightly more bluish SED of the backscattered light due to the decreasing scattering efficiency for increasing wavelengths. This is not observed. Instead, the diffuse emission is clearly redder than the star and seems to be associated with object F4 whose emission strongly increases in the L' and nb\_M band, while the star F2 strongly fades beyond  $2.2 \mu\text{m}$ . We therefore think that this star F2 is clearly detached from the actual star-forming region.

We should re-emphasise that both the weak cm continuum emission and the  $\text{NH}_3(5,5)$  emission associated with the HMC component F peak very close ( $\leq 0''.4$ , cf. Table 3.1) to F4 (see also Figs. 3.3 and 3.4) which suggests an intrinsic entanglement of the two components. Thus, we interpret F4 as arising from the inner parts of the HMC outflow cavity.

One detail is not yet clarified: Is the L' and nb\_M band signal of F4 caused by direct thermal dust emission of hot grains very near to the embedded power source of the HMC? Or can a considerable fraction of the overall emission be attributed to reprocessed light scattered on the cavity walls? In the latter case one has to assume the existence of larger dust grains in the HMC envelope to ensure a reasonably high scattering efficiency<sup>7</sup> for wavelengths of 3 –

<sup>6</sup> It is difficult to confirm this claim just by looking at Fig. 3.9. This kind of plot is well-suited for visualising the polarisation pattern for extended emission but is often misleading around compact sources with steep intensity gradients. In these cases the polarisation has to be derived by aperture photometry centred on the compact sources in all the polarimetric frames and then applying Eqs. (3.1) and (3.2).

<sup>7</sup> Usually, the scattering efficiency is strongly diminished at wavelengths beyond  $\approx 2-3 \mu\text{m}$  when only dust is considered

5  $\mu\text{m}$ .

These ideas about larger grains are more than a wild speculation. Grain growth is expected to occur in YSOs and their near vicinity, in particular in circumstellar disks (e.g., Beckwith & Sargent 1991, Beckwith, Henning, & Nakagawa 2000, D’Alessio, Calvet, & Hartmann 2001). Recent observations (e.g., McCabe et al. 2003, Shuping et al. 2003) seem to indicate – cum grano salis – the existence of a considerable amount of micron-sized particles in disks around low-mass YSOs. Systematic investigations of massive YSOs seem to be scarcer, especially regarding HMCs. However, for the best-known region of ongoing massive star formation, Orion, polarimetric observations at 2.2 and 3.8  $\mu\text{m}$  point to the existence of larger grains in the Orion Molecular Cloud in general (Rouan & Leger 1984) and in particular in the BN/KL region containing the Orion Hot Core (Minchin et al. 1991, Dougados et al. 1993).

Thus, a future task will be to conduct high-resolution polarimetric measurements in the K, L’, and nb\_M band. Adaptive optics systems like CONICA/NAOS at the VLT seem to be most suitable to ensure high resolution (0’’1) combined with high sensitivity – characteristics that are absolutely necessary for delivering meaningful polarimetric results in the case of G9.62+0.19–F.

### 3.6.2 Ordinary stars within the HMC vicinity?

We have already pointed out that object F2 very near the HMC is probably a foreground star. Is it also possible that object F1 is a normal star whose photospheric emission we see? We have several reasons for rejecting this possibility.

We start with the following estimate: We use the well-known correlation between the colours of a star and its colour excess due to additional reddening:

$$H - K = (H - K)_0 + E_{H-K} . \quad (3.3)$$

Herein,  $(H - K)_0$  is the unreddened intrinsic colour of the star and the colour excess  $E_{H-K}$  can be expressed as

$$E_{H-K} = A_H - A_K = \left( \frac{A_H}{A_K} - 1 \right) A_K . \quad (3.4)$$

According to Mathis (1990), the  $A_H/A_K$  ratio for the standard interstellar reddening law ( $R_V = 3.1$ ) is around 5/3. We can use the intrinsic stellar colours (e.g., Wegner 1994 for O and B stars, Bessell & Brett 1988 for stars of type A – M) and our measured value  $H - K = 4.4$  mag to derive the K band extinction  $A_K$ . O stars of all luminosity classes have  $(H - K)_0$  values between  $-0.08$  mag and  $-0.02$  mag. In combining Eqs. (3.3) and (3.4) we find that  $A_K$  is always larger than 6.6 mag for our case. Together with the distance modulus of 13.8 (assuming  $d = 5.7$  kpc) and the measured K band magnitude of 13.6 mag (see Table 3.2), the absolute K magnitude  $M_K$  would be  $-6.8$  mag. Moreover, if we take into account that all O stars have  $(V - K)_0$  values between  $-0.7$  mag and  $-0.9$  mag, the absolute

---

with the standard MRN size distribution (Mathis et al. 1977) typical for the interstellar medium, i.e., the overwhelming majority of the dust particles is sub-micrometer-sized with a typical diameter of  $\approx 0.1 \mu\text{m}$ .

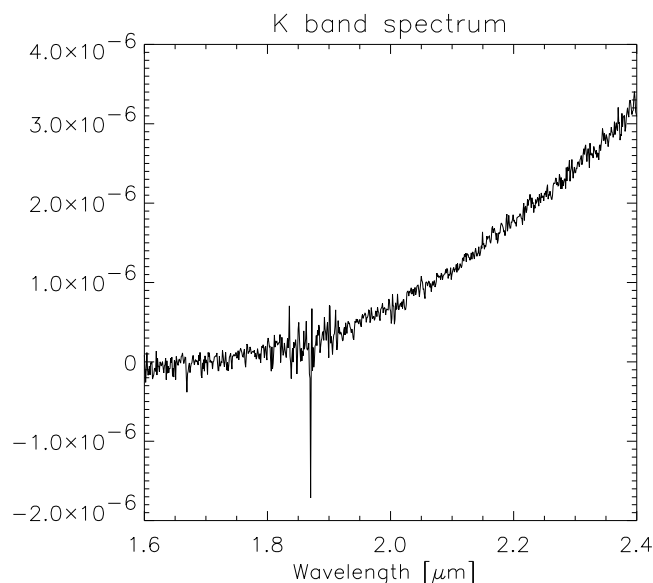


**Figure 3.11:** The K band medium-resolution spectrum of object F1 (in arbitrary units), taken with *SofI* at the ESO *NTT*.

visible magnitude  $M_V$  would be brighter than  $-7.5$  mag! O and B stars do not feature such bright  $M_V$  values, only very extreme supergiants (luminosity class 1a-0) would exhibit such a characteristic. Furthermore, if we considered late-type giants we would also have to deal with extreme luminosity classes which, in addition, would cause a severe dilemma in explaining the existence of a very old star almost in the centre of a young star-forming region.

Striking evidence against photospheric emission comes from the K band medium-resolution spectrum (Fig. 3.11) which was taken with *SofI* at the 3.5-m *NTT* on La Silla, Chile (Testi 2001). The slit was centred on the object F1, but the spectrum probably also covers some contribution from the foreground star F2. Around  $1.87 \mu\text{m}$  the transmission of the atmosphere strongly decreases due to strong  $\text{H}_2\text{O}$  absorption, separating the near-infrared H and K band. The strong feature around  $1.87 \mu\text{m}$  probably arises from the fact that this atmospheric imprint was not totally canceled out in the calibration. In the range between  $1.95$  and  $2.40 \mu\text{m}$  we see a spectrum without prominent features. Especially late-type stars with their relatively cool atmospheres should show many metallic lines and even molecular lines. A characteristic feature for such stars are more or less strong CO absorption features between  $2.29 \mu\text{m}$  and  $2.40 \mu\text{m}$  (Ramírez et al. 1997, Bieging et al. 2002), but we only see an almost featureless spectrum monotonically rising towards the K band edge, which is an imprint of continuum dust emission.

These points speak clearly against the “naked star” interpretation for the object F1. They rather indicate the presence of an embedded object within a dusty shell. In a way, this resembles the situation of the Orion BN/KL region where several IR objects are located in the vicinity of the Orion Hot Core. It might be tempting to see our object F1 as an analogue to the BN object with regard to the general appearance and the dusty shell nature

of both objects. However, this analogy does not hold. Fig. 3.10 indicates that F1 reaches its maximum emission at a wavelength around  $5 \mu\text{m}$  and then drops again and hence is not detected at  $11.7 \mu\text{m}$  anymore. This suggests an object of lower luminosity (a few tens  $L_{\odot}$ , if really located at  $d = 5.7 \text{ kpc}$ ). BN is 70 – 100 times more luminous than F1 (1500 – 2500  $L_{\odot}$ , Dougados et al. 1993, Gezari et al. 1998), it has probably a far more massive reservoir of dust around and is of course still strong at 10 and  $20 \mu\text{m}$ .

### 3.7 Comparison with other HMCs

To date, the number of firmly established HMC sources is still quite small. Apart from the well-investigated Orion BN–KL region, only a few HMCs have been studied by means of high-resolution infrared observations (cf. Stecklum et al. 2002a, 2002b, De Buizer et al. 2002, 2003, Pascucci et al. 2004).

In this respect, it is worth comparing the infrared properties of our region with a similar examination of the hot molecular core in W3(H<sub>2</sub>O). Both HMC regions seem to be related to outflow activity. But in the latter case no NIR/MIR emission could be detected in the direct vicinity of the HMC by Stecklum et al. (2002b) who derive an extinction at  $11.7 \mu\text{m}$  of still  $\gtrsim 12$  magnitudes. One explanation could be that the outflow is mainly in the plane of the sky, so that we cannot benefit from an outflow-related clearing effect.

Another possibility might be that the potential outflow material had not yet have time enough to sufficiently penetrate the very dense shell of the inner HMC region as is instead apparently the case for our HMC component F. In that case, we would rate the G9.62+0.19 hot molecular core to be in a more evolved state than the W3 one.

Support for this argumentation comes from recent 3-mm and 1.3-mm interferometric line observations of G9.62+0.19 with OVRO (Liu 2003). This author discusses the use of several molecules as chemical clocks. First, he uses H<sub>2</sub>S to re-confirm the age differentiation among the components D, E, and F, since H<sub>2</sub>S is eventually transformed into other species after it has been liberated from grain mantles into the warm molecular core environment. Among the three cores, component F shows the highest H<sub>2</sub>S abundance and would thus be younger than E and D both of which have already developed an ultracompact HII region. This finding is in accordance with our previous results of the NH<sub>3</sub>/CH<sub>3</sub>CN abundance comparison (Hofner et al. 1996). Furthermore, Liu (2003) compares the CH<sub>3</sub>OH and C<sub>2</sub>H<sub>5</sub>CN emission at 3 mm. While the observed methanol emission shows extended structure along the molecular ridge including D, E and F, ethyl cyanide is primarily detected toward core F. Since revised chemical HMC models usually produce significant amounts of N-bearing molecules only after O-bearing species have reached their peak abundances (e.g., Rodgers & Charnley 2001, 2003), the strong C<sub>2</sub>H<sub>5</sub>CN emission toward component F suggests that it is in a more advanced stage of HMC evolution.

This fits well to the scenario advocated by Kurtz et al. (2000) that HMCs can evolve first into hypercompact (Gaume et al. 1995, Tieftrunk et al. 1997, Kurtz 2000) and finally into ultracompact HII regions. The detection of weak emission at 1.3 and 3.6 cm, associated with

**Table 3.3:** Physical parameters of the radio components D and E

Physical parameter	component D	component E	extinction law <sup>b</sup>
$T_b$ [K] <sup>a</sup>	977	210	
$T_e$ [K]	8000	8000	
$N(\text{H})$ [ $\text{cm}^{-2}$ ]	$2.54 \times 10^{24}$	$1.84 \times 10^{24}$	
$S_{\text{Br}\gamma}$ [ $\text{W cm}^{-2}$ ]	$1.083 \times 10^{-19}$	$2.21 \times 10^{-20}$	
$A_{2.2\mu\text{m}}$ [mag]	125	90	$R_V = 3.1, CF(2.2\mu\text{m})=0.108$
$A_{12\mu\text{m}}$ [mag]	32	23	$R_V = 3.1, CF(12\mu\text{m})=0.028$
$A_{2.2\mu\text{m}}$ [mag]	232	168	$R_V = 5.0, CF(2.2\mu\text{m})=0.125$
$A_{12\mu\text{m}}$ [mag]	60	43	$R_V = 5.0, CF(12\mu\text{m})=0.032$

<sup>a</sup> The brightness temperatures were derived taking the emission in the inner  $0''.55$  of the components into account which corresponds to our  $K_s$  band resolution element (i.e. seeing).

<sup>b</sup> see Sect. 3.8 for details

a high emission measure of  $3 \times 10^8 \text{ pc cm}^{-6}$ , by Testi et al. (2000) implies that the HMC component F is on its way to cultivate a hypercompact HII region.

Furthermore, Cesaroni et al. (1998) analysed two other well-known hot molecular cores (G10.47+0.03 and G31.41+0.31) and found indications that the HMC stage marks the phase of transformation from spherically symmetric to flattened and non-spherical structures. Also in this regard, G9.62+0.19-F proves to be a typical example of an HMC.

### 3.8 Why can't we see the D and E components in the infrared?

Radio component F which is only a weak cm continuum source nevertheless shows infrared features in its immediate vicinity. Hence, at first glance it might be intriguing that the stronger radio sources D and E, which both are more massive and energetic than component F (Hofner et al. 1996), do not show an infrared counterpart. Without a further analysis one might come to a similar conclusion as De Buizer et al. (2000) who, for lack of exact astrometry, just shifted their mid-infrared source to the position of the radio D component. To clarify these circumstances, we reconsider radio data from previous papers about G9.62+0.19 to derive the expected Brackett  $\gamma$  fluxes from, as well as the extinction towards, D and E.

#### The expected Br $\gamma$ fluxes of D and E

The method to compute the expected flux in IR recombination lines on the basis of cm continuum data has been explained extensively by Watson et al. (1997) and has also been

applied in previous investigations of the Jena / Tautenburg group toward other massive star-forming regions (e.g., Feldt et al. 1998, 1999). We refer to these papers for details and start with their formula for the emission measure ( $EM$ ), which can basically be derived from the approximation of Altenhoff et al. (1960) for the optical depth of cm free-free emission:

$$EM = 4.72 a^{-1} T_e^{1.35} \nu^{2.1} \ln\left(\frac{T_e}{T_e - T_b}\right) \text{ cm}^{-5}. \quad (3.5)$$

Herein,  $T_e$  and  $T_b$  are the electron temperature and the brightness temperature, respectively, both in Kelvin. The parameter  $\nu$  is the frequency (in Hz) at which  $T_b$  was derived. Finally,  $a(\nu, T)$  is a correction factor of the order of 1, which is tabulated in Mezger & Henderson (1967) for various frequencies and electron temperatures.<sup>8</sup>

By adopting the approach of Osterbrock (1989) we can use the emission measure to compute the expected Br  $\gamma$  flux under the assumption that no extinction occurs:

$$S_{\text{Br}\gamma} = 0.9 h\nu_{\text{Br}\gamma} \alpha_{\text{Br}\gamma}^{\text{eff}} \frac{\Omega_{\text{Br}\gamma}}{4\pi} EM. \quad (3.6)$$

The factor 0.9 reflects the assumption that an UCHII region consists of  $\sim 10\%$  of singly ionised Helium, which contributes electrons *and* ions to the cm free-free emission but only electrons to the Br  $\gamma$  emission. For  $\alpha_{\text{Br}\gamma}^{\text{eff}}$ , which comprises the transition coefficients and the level populations via a temperature dependency, Hummer & Storey (1987) give:

$$\alpha_{\text{Br}\gamma}^{\text{eff}} = 6.48 \times 10^{-11} T_e^{-1.06}. \quad (3.7)$$

For our computations we derived the brightness temperatures of components D and E from the 1.3 cm map of Testi et al. (2000).<sup>9</sup> The electron temperatures of both regions were estimated by Hofner et al. (1996), using a thermal bremsstrahlung model to fit the cm continuum observations conducted up to that point. We list all the parameters in Table 3.3.

The expected Br  $\gamma$  flux is  $1.083 \times 10^{-19} \text{ W cm}^{-2}$  for component D and  $2.21 \times 10^{-20} \text{ W cm}^{-2}$  for component E for the theoretical limit of zero extinction. These values correspond to 5.75 mag and 7.48 mag in terms of K band magnitudes. If we use the ISAAC camera in combination with the Br  $\gamma$  filter, we would detect such fluxes with an SNR of 20 within less than 1 s of exposure time.

### The extinction towards D and E

To evaluate these numbers one has to estimate the extinction towards these regions. Hofner et al. (1996) derived  $\text{H}_2$  column densities, based on interferometric  $\text{C}^{18}\text{O}(1-0)$  observations, for the components D, E, and F. They report values of  $N(\text{H}_2) = 12.7 \times 10^{23} \text{ cm}^{-2}$  for component D and  $N(\text{H}_2) = 9.2 \times 10^{23} \text{ cm}^{-2}$  for component E. To transform these column densities into

<sup>8</sup>Beckert et al. (2000) demonstrate that this approximation (Altenhoff + Mezger&Henderson correction factor) is in very good agreement with non-approximative numerical solutions up to frequencies of  $\sim 100$  GHz.

<sup>9</sup>The 3.6 cm map of Testi et al. (2000) has a higher SNR, but Hofner et al. (1996) found that the behaviour of the components D and E already deviates from the optically thin regime at this wavelength.

extinction values we start with the empirical relation that links the total hydrogen column density  $N(\text{H})$  to the optical colour excess  $E_{\text{B-V}}$  (Ryter 1996):

$$N(\text{H}) = 6.83 \times 10^{21} E_{\text{B-V}} \text{ cm}^{-2} \text{ mag}^{-1} . \quad (3.8)$$

In order to substitute  $E_{\text{B-V}}$ , we use the ratio  $R_V$  of absolute to relative extinction:

$$R_V = A_V / E_{\text{B-V}} . \quad (3.9)$$

Combining Eqs. (3.8) and (3.9) we get an expression for the visible extinction  $A_V$ , based on column densities. Finally, we can introduce a conversion factor  $CF(\lambda)$  that represents the conversion from the visible extinction ( $A_V$ ) to extinction values at other wavelengths ( $A_\lambda$ ). We arrive at the following expression:

$$A_\lambda = \frac{R_V N(\text{H})}{6.83 \times 10^{21} \text{ cm}^{-2} \text{ mag}^{-1}} CF(\lambda) . \quad (3.10)$$

Mathis (1990) gives two sets of conversion factors, corresponding to two possible extinction laws: normal “diffuse interstellar dust” ( $R_V = 3.1$ ) or “outer-cloud dust” ( $R_V = 5.0$ ). For both possibilities, we compute extinction values at  $2.2 \mu\text{m}$  and  $12 \mu\text{m}$  using  $N(\text{H}) = 2 \times N(\text{H}_2)$ . The results are listed in Table 3.3. In any case, the extinction is  $\geq 90$  mag at  $2.2 \mu\text{m}$  and still  $\geq 23$  mag at  $12 \mu\text{m}$ . Such a large extinction would attenuate the fluxes down to an undetectable value. But one important restriction applies to this “naïve” interpretation of the extinction data. The  $\text{C}^{18}\text{O}$  line is optically thin; hence, it traces the column density of the whole molecular cloud and not just the column density up to the UCHII regions. Theoretically, the UCHII regions could even be located in front of the molecular clouds, which is obviously not the case.

### Relative positions of UCHII regions and the molecular gas

One approach for clarifying the situation is to compare the LSR velocities of radio recombination lines (RRLs) produced in the UCHII region with the LSR velocities of molecular lines seen in absorption against the radio continuum of the UCHII region. This idea has already been pursued by Downes et al. (1980) and was recently revived by Araya et al. (2002) who could show that in almost all of their UCHII region targets the ionised gas and the main absorbing molecular component have the same velocity within the uncertainties of the measurements. This demonstrates that a close association between the two classes of objects is very common.

1.) As far as we know, no radio recombination line studies exist for G9.62+0.19 that would provide high spatial resolution. Therefore, we go back to the seminal work of Downes et al. (1980) who conducted a combined survey of the  $\text{H}110\alpha$  RRL and  $\text{H}_2\text{CO}$  ( $1_{10} - 1_{11}$ ) absorption line with the Effelsberg 100 m telescope at 6 cm. Their observations for G9.62+0.19 were centred on component B and had a half-power beamwidth of  $\sim 2.6$  arcmin. The reported LSR velocities are  $(3.0 \pm 5.0) \text{ km s}^{-1}$  for the RRL and  $(2.0 \pm 0.5) \text{ km s}^{-1}$  for the  $\text{H}_2\text{CO}$

absorption line.<sup>10</sup> The velocities are almost equal which speaks for a close association also in the case of G9.62+0.19.

2.) The fact that we actually see absorption implies that a noticeable fraction of the molecular gas is located in front of the HII regions.

3.) The measured H<sub>2</sub>CO line temperature for G9.62+0.19 is smaller than the continuum temperature of the ionised sources (Downes et al. 1980). An opposite finding would imply that most of the H<sub>2</sub>CO absorption occurs just by absorbing photons of the Cosmic Microwave Background and would therefore not be related to the HII regions at all.

4.) In the HCO<sup>+</sup> data of G9.62+0.19 (Hofner et al. 2001), which were taken with the IRAM 30 m telescope and with the Plateau de Bure (PdB) interferometer, a strong absorption dip in this molecular line at the LSR velocity of the RRLs and the H<sub>2</sub>CO absorption is clearly visible. An interpretation mentioned in that paper is self-absorption due to a high optical depth. However, this feature can also be understood as absorption against the 89 GHz continuum of the (ultra)compact HII regions. Probably both effects contribute to the observed line absorption. Note that the PdB data provide sufficient spatial resolution to distinguish between components D and E and that component B is not dominant in these data.

5.) Regarding the morphology of the components D and E we do not see obvious features that could explain these UCHII regions within the scope of blister/champagne flow models (Tenorio-Tagle 1979, Yorke 1986) which would be the consequence of the location of the UCHII regions very near the border of the embedding molecular cloud.

These five points support the idea that both cm continuum components (D and E) are clearly embedded within their parental molecular cloud, although we cannot exactly estimate their relative positions. We cite here recent investigations by Kim & Koo (2003), based on molecular line observations towards 16 UCHII regions. They indicate that the formation of massive stars, in general, does not take place near the surface of molecular clouds but in their interiors. In this regard, one has to take into account that already the positioning of the UCHII regions D and E behind 20 % of the total amount of molecular gas would be sufficient to explain our non-detections. On the basis of these considerations we conclude that the invisibility of the components D and E in the near- and mid-infrared is a reasonable finding.

### 3.9 Conclusions

We have performed a comprehensive set of infrared observations for the G9.62+0.19 star-forming region. Narrow-band and broad-band observations from 1 to 19  $\mu$ m provided new information about this complex of young stellar objects. In the following we summarise our results.

1.) The high resolution of our data revealed the detailed structure of the Hot Molecular Core region G9.62+0.19-F. The K band emission found by Testi et al. (1998) could be disentangled into three distinct objects. Our astrometry shows that among these three objects the

<sup>10</sup>The RRL velocity is confirmed by Lockman (1989) who gives  $v_{\text{LSR}} = (4.1 \pm 0.8) \text{ km s}^{-1}$  for the H85 $\alpha$ , H87 $\alpha$  and H88 $\alpha$  lines towards G9.62+0.19, based on observations with the NRAO 43 m telescope with a FWHM of 3 arcmin.



dominating source F1 is not coincident with the peak of the molecular line emission of the hot molecular core. Instead, it is displaced by  $\sim 1.7$  arcsecs, which translates to roughly 10000 AU on a linear scale. We estimate that the second object F2 is probably a foreground star not intrinsically related to the star-forming region. No reliable interpretation can be given for the third very faint object F3 in the HMC region, since it is only visible in the Ks and L' band.

**2.)** Very near the peak of the HMC molecular line emission and partly blended with the foreground star we find faint diffuse emission at  $2.16 \mu\text{m}$ . While the foreground star F2 quickly fades at wavelengths  $> 3 \mu\text{m}$ , this emission strongly increases in the thermal infrared and finally reveals the presence of another object, F4. We propose that object F4 is directly associated with the HMC. This presents the first detection of a hot molecular core at a wavelength as short as  $3.8 \mu\text{m}$ . We know that the HMC probably drives a molecular outflow roughly aligned with the line of sight (Hofner et al. 2001). Thus, the clearing effect of this outflow might allow us to look deeper into the infrared-emitting regions of the core environment. The results of our K band polarimetry support the interpretation that the diffuse K band emission arises from scattering of light in the outflow cone. Finally, our mid-infrared data highlight object F4 as the most luminous object within the HMC region. With the SED of F4 the range for several parameters of the HMC can be narrowed.

**3.)** The combined results of the astrometry and radiative transfer computations make it unlikely that the dominant object F1 is a direct trace of the HMC. Nevertheless, we have demonstrated that on the basis of the NIR colours and the K band spectrum the most likely explanation is a dense dust shell around a deeply embedded object of lower luminosity. This might be a hint for multiplicity of YSOs within the HMC region. In a way, G9.62+0.19-F resembles the Orion Hot Core region, where likewise the near vicinity of the HMC is populated by a variety of infrared sources.

**4.)** We evaluate the fact that the UCHIIIs D and E are not detected in our infrared data although these objects show much stronger radio emission than the HMC region F. By reexamining available high-resolution radio molecular line data we derive theoretical values for the extinction towards D and E and show that our non-detections are in agreement with these predictions.

**5.)** Using our K-narrow-band results and the imaging polarimetry we reveal within the whole G9.62+0.19 star-forming complex well-defined regions of enhanced Br $\gamma$  and H $_2$  emission as well as a sector where a large contribution comes from scattered light. This demonstrates the complex composition of such high-mass star-formation regions that would escape our views when just using simple broad-band imaging.

The results reported in this chapter have recently been published in:  
H. Linz & collaborators, *Astronomy & Astrophysics* **429**, (2005), 903.

## Chapter 4

# ***GGD 27 – A splendiferous IR reflection nebula with a pumping heart***

A certain picture of the main sources in the GGD 27 region had been established in the 1990s (see Sect. 2.1.2). Still, a final conclusion about the nature of GGD 27–ILL could not be drawn yet. Nevertheless, there are a few (indirect) points that make GGD 27–ILL a promising candidate for a massive YSO featuring a circumstellar disk. Thus, with the new generation of IR cameras, millimetre bolometer arrays, and the *VLA* 7-mm system now in full bloom, revisiting GGD 27 is worthwhile and will reveal some surprising details. In Sect. 4.1 we present the results of the imaging in the wavelength range 2 – 20  $\mu\text{m}$  as well as a new 8 – 13  $\mu\text{m}$  spectrum of GGD 27–ILL. A dust model is fitted to the spectrum which gives some direction for the possible grain population in the circumstellar environment of the central source. In Sect. 4.2 we introduce the results from our *VLA* 7-mm imaging tackling the central jet-driving source which is generally assumed to be intimately related to GGD 27–ILL. In Sect. 4.3 we report the presence of new millimetre cores in the farther environment of GGD 27 and the correlation of previously found X-ray sources with sources seen in our NIR imaging. In the discussion section 4.4 we mainly elaborate on the infrared results toward GGD 27–ILL by means of a simple radiative transfer model and considerations about the luminosity of this source. Finally, in Sect. 4.5 we summarise our results.

### **Prelude**

As first, a note about the commonly adopted distance of 1.7 kpc for GGD 27. This value was found by Rodríguez et al. (1980) by comparing the systemic CO velocities of GGD 27 with a Schmidt (1965) model rotation curve of the Galaxy. This distance estimate has propagated basically through **almost all**<sup>1</sup> of the following publications regarding GGD 27/HH80–81. However, the Schmidt models used 10 kpc as the galactocentric distance of the Sun and a circular orbit velocity of 250 km/s for the Sun. With the currently accepted values (8.5 kpc, 220 km/s) and an empirical rotation curve based on the work of Brand (1986), we derive a distance to GGD 27 ranging from 1.9 kpc (when using the 11.0 km/s from the above mentioned CO measurements) to 2.0 kpc (when using 12.1 km/s as given by Gómez et al. (2003)

---

<sup>1</sup>The sole exception we are aware of is the paper of Hunter et al. (2000) which uses 1.9 kpc.

for the SO  $5_5 - 4_4$  observations towards the central source GGD 27–ILL). Thus, derived parameters that depend quadratically on the distance (like dust masses or luminosities) might be too small by a factor of up to 1.4 when using 1.7 kpc. Throughout this chapter we will adopt a distance of 2.0 kpc.

## 4.1 Infrared results

The GGD 27 region has been covered by several investigations in the infrared in the 1980's and 1990's, performed with telescopes of the 2 – 4 metre class. Already back then, the wealthy IR structure of the GGD 27 region has been emphasised. In the current investigation, we shall concentrate on the central source, GGD 27–ILL itself. Therefore, we put aside a detailed discussion of the nature of other well-known infrared sources of GGD 27 (in particular IRS1, IRS7, IRS8, and IRS9). However, we will briefly report some new findings for these sources in passing.

### 4.1.1 K narrow-band imaging

The most impressive feature of GGD 27 in the near-infrared is a large-scale reflection nebula with roughly the same orientation (north-northeast to south-southwest) as the well-known radio jet (P.A.  $17^\circ - 20^\circ$ ). The general morphology is bipolar, however, the northern wing appears more structured and dense. Earlier studies described it as wishbone-like. Our ISAAC data with a resolution of around 0.5 arcseconds reveal many new details and subcondensations (see Fig. 4.1). These structures are probably formed by the interaction of a large and powerful molecular outflow (Yamashita et al. 1989, Benedettini et al. 2004) with the remnants of several cloud cores (Yamashita et al. 1991, Gómez et al. 2003, see also the right panel of Fig. 2.2) in the vicinity of the central sources GGD 27 IRS2/ILL. Nevertheless, several weak point sources are found to be immersed within the diffuse emission.

The diffuse emission is known to be highly polarised in the near-infrared (Yamashita et al. 1987, Tamura et al. 1991, Aspin et al. 1991) revealing its nature as a reflection nebula. The illuminating source, named GGD 27–ILL by Aspin et al. (1991), lies very near to the central bright source of Fig. 4.1 (IRS2) but is not directly visible in the K band. A dark lane cuts through this area, spanning from the northwest of GGD 27–ILL (which is located roughly at the reference position in the images) more than 10 arcseconds down and finally leading into a generally more extinguished region to the southeast of IRS2 (best seen in Figs. 4.1 and 4.12). The whole configuration of GGD 27 (bipolar reflection nebula with intersecting dark lane) bears some similarities to another famous and massive young stellar object, namely S106 IRS4.<sup>2</sup>

Within the reflection nebula itself we do not find large areas with strong excess line emission in Bry or H<sub>2</sub>(1–0)S1. This indicates that we mainly see reflected continuum light. However,

<sup>2</sup>Still the nicest visual impression of S106 IRS4 one can get from a press release of the Subaru Telescope (operated by the Japanese NAOJ) from 2001: <http://www.naoj.org/Pressrelease/2001/02/>

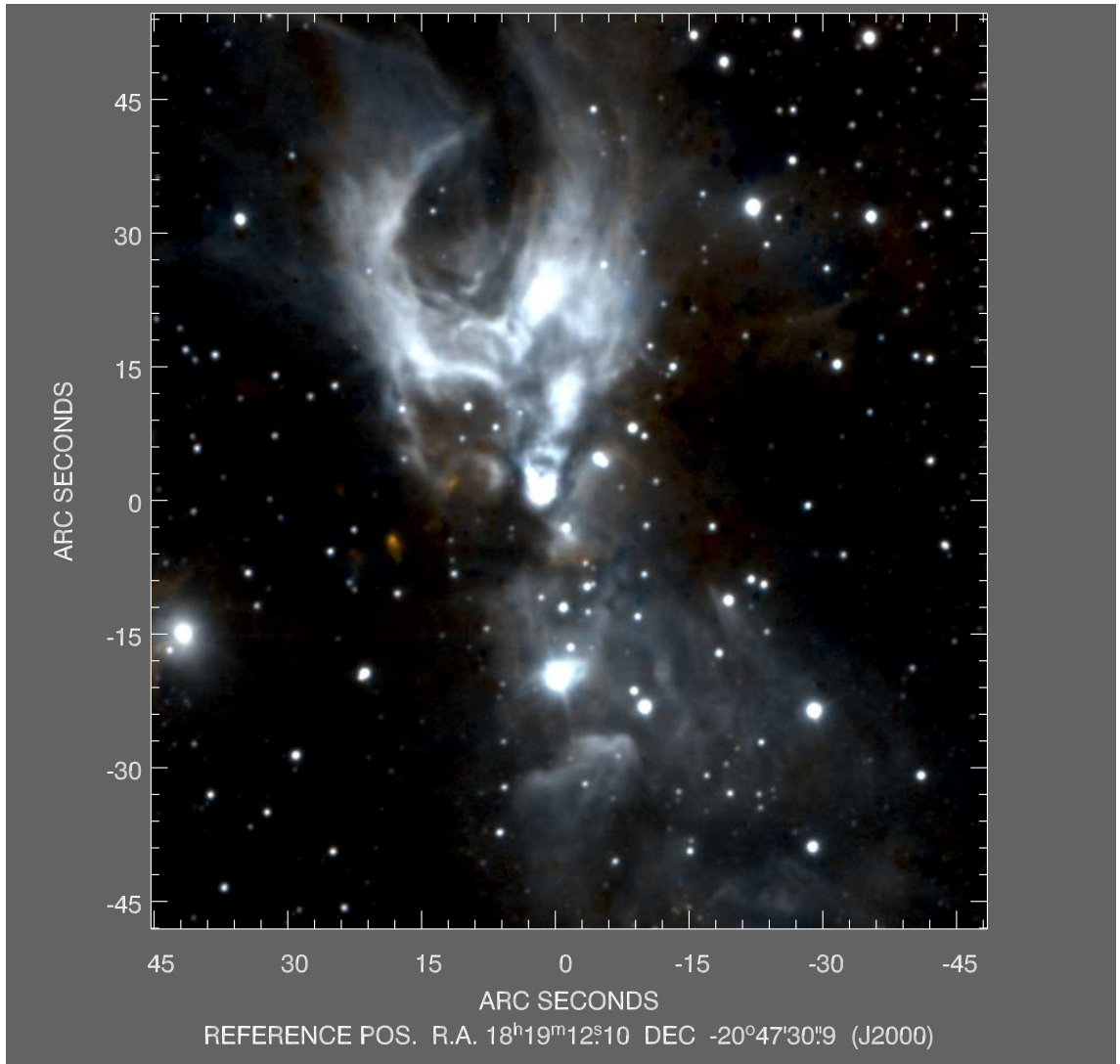


**Figure 4.1:** K narrow-band colour composite of the entire GGD 27 region. Bry emission is coded in blue, while  $\text{H}_2(1-0)\text{S}1$  emission is coded in red. In order not to disturb the beauty of the picture, we abstain from including further labelling of sources here. We refer to Fig. 4.2 for source denotations.

we find local blobs of  $\text{H}_2$  emission in the region east of IRS 2, surprisingly not aligned with, but almost perpendicular to the radio jet axis. The strongest  $\text{H}_2$  feature has the coordinates:  $\alpha_{2000} = 18^{\text{h}}19^{\text{m}}13^{\text{s}}.41$ ,  $\delta_{2000} = -20^{\circ}47'35''.6$ . It can be found in Fig. 4.1 at the offset coordinates (+19, -5). Together with some weaker  $\text{H}_2$  features, it spans an almost straight line between the vicinity of IRS3 – the strong IR source at the offset coordinates (+42, -15) in Fig. 4.1 – and the region containing the radio source VLA3 and its associated  $\text{H}_2\text{O}$  maser (Gómez et al. 1995) roughly at the offset coordinates (+6, +6) in the same figure. We know from the SMA  $850 \mu\text{m}$  observations of Su et al. (2004b) that this VLA3 region is also associated with submillimetre dust emission – the secondary contour peak to the northeast in our Fig. 4.10 shows this finding. With the available data we cannot prove a connection, but we can speculate that also in the VLA3 region star formation is ongoing. Outflow and jet activity, independent from the main source GGD 27–ILL, might exist there which gives rise to these aligned  $\text{H}_2$  features.

## 4.1.2 Thermal infrared imaging

### Plain L' and nb\_M band imaging

As in the case of G9.62+0.19 (Sect. 3.2), the imaging in the thermal infrared also turns out to be particularly useful for revealing the detailed structure of the central region of GGD 27. The interplay of wavelength-dependent extinction and the intrinsic SED of the embedded sources leads to fundamental changes in appearance of the GGD 27 IRS2/ILL region when going from 2.15  $\mu\text{m}$  to 4.66  $\mu\text{m}$ . The illuminator of the region (GGD 27–ILL) is not directly visible at 2.15  $\mu\text{m}$  also for our *ISAAC* imaging, and IRS2 is dominating at that wavelength. As we go to the L' band we reveal a source at the position of GGD 27–ILL that finally dominates in the nb\_M band (Figs. 4.2 and 4.3). While emission from GGD 27–ILL has been reported at 4.7  $\mu\text{m}$  already (Aspin et al. 1994), this is the first time that the illuminator is detected at a wavelength as low as 3.8  $\mu\text{m}$ . Furthermore, for the first time morphological details of this source can be studied at all. In Fig. 4.2 we show 42''  $\times$  42'' regions of the GGD 27 centre area and give important IR source annotations. In Fig. 4.3 we choose a smaller cutout and overlay the contours of *VLA* D-array observations at 7 mm that have a spatial resolution of ca. 2''. These 7-mm continuum data have been obtained in the same observing run as the 44-GHz Methanol maser data reported in Kurtz, Hofner & Vargas Álvarez (2004). A future publication (Hofner, Araya, Linz, et al., in preparation) will further analyse these data. Here we just use them to demonstrate the positional relation of the infrared source GGD 27–ILL and the central source of the radio jet that is traced by the *VLA* observations<sup>3</sup>.

### Results of the image deconvolution

Already from the plain *ISAAC* L' and nb\_M band images we learn that GGD 27–ILL is not a simple unresolved point source but possesses a lot of structure. To further investigate this, we applied a Richardson–Lucy deconvolution to the images. Choosing the optimal parameters for such a deconvolution is always a difficult task. We emphasise that it is not our goal to perform the “best” deconvolution possible but just to moderately increase the spatial resolution of the images.

We refrained from using the standard star images as basis for the deconvolution kernel. All our L' and nb\_M band data have been obtained in service mode with the standard calibration plan, and hence such standard star data are often taken with relaxed constraints for field stabilisation during the observations. Indeed, from checking by eye the standard star PSF looks peculiar and does not really resemble the star shapes in the science data.

Instead, we used an iterative approach to generate a PSF from the science data itself which is possible if enough unresolved point sources are contained in the image. Ten iterations in total have been used to create the PSF and to deconvolve the raw data. The same deconvolution approach has also been used for treating the narrow-band K images, and hence we can compare in Fig. 4.4 the deconvolution results for all three wavelengths.

<sup>3</sup>It turned out to be rather difficult to use our own *VLA* 7-mm data (reported in Sect. 4.2) for this kind of contour plot shown in Fig. 4.3 since the spatial resolution of our B array data (0''.2) is too high to give a meaningful impression on this scale.

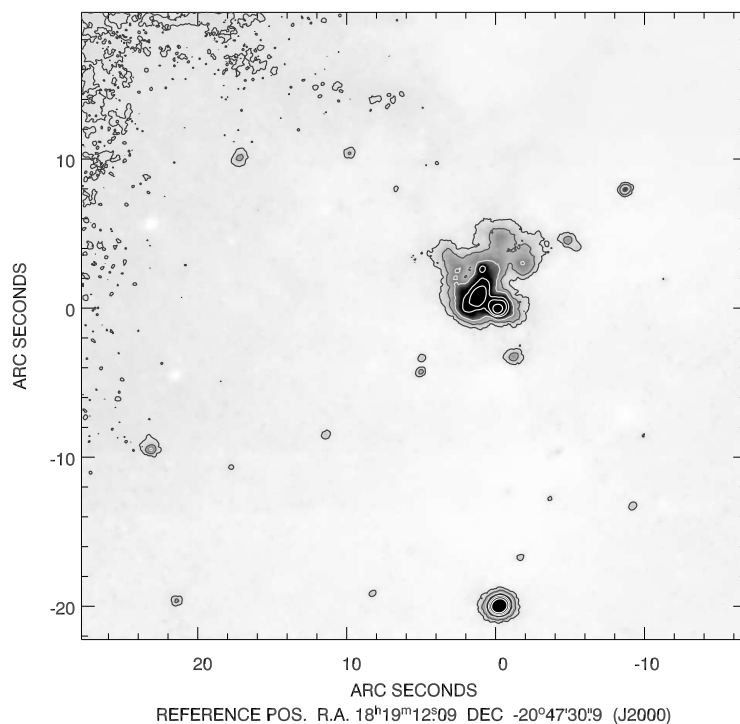
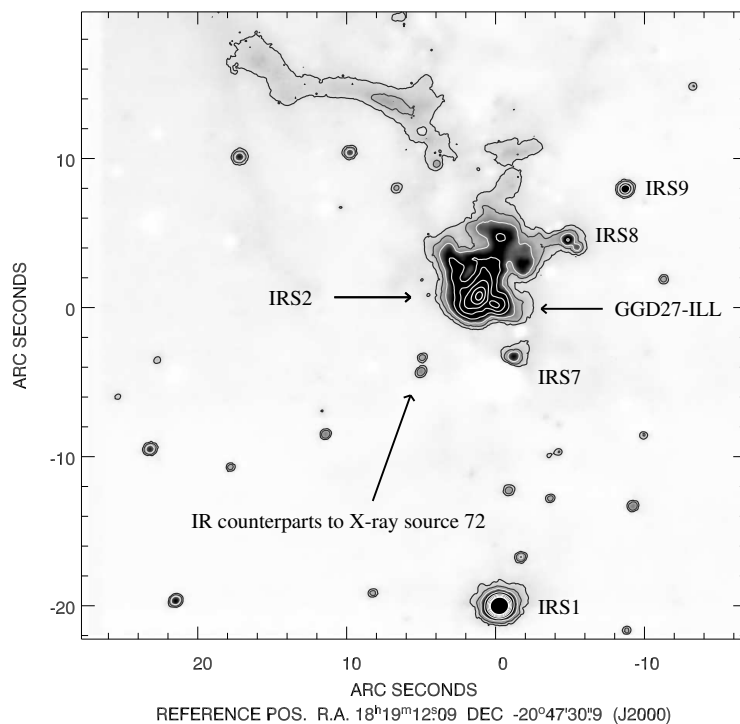


**Figure 4.2:** The central source of GGD 27 and its vicinity covered by our L' band (upper panel) and nb\_M band (lower panel) imagery. The contour levels are (5, 10, 30, 50, 70, 100, 200, 250) times the rms noise in the L' band image, and (3, 5, 8, 20, 40, 75) times the rms noise in the nb\_M band image. Prominent infrared sources (following the nomenclature of Tamura et al. (1991)) are marked in the L' band image to keep track of the sources mentioned in the text.

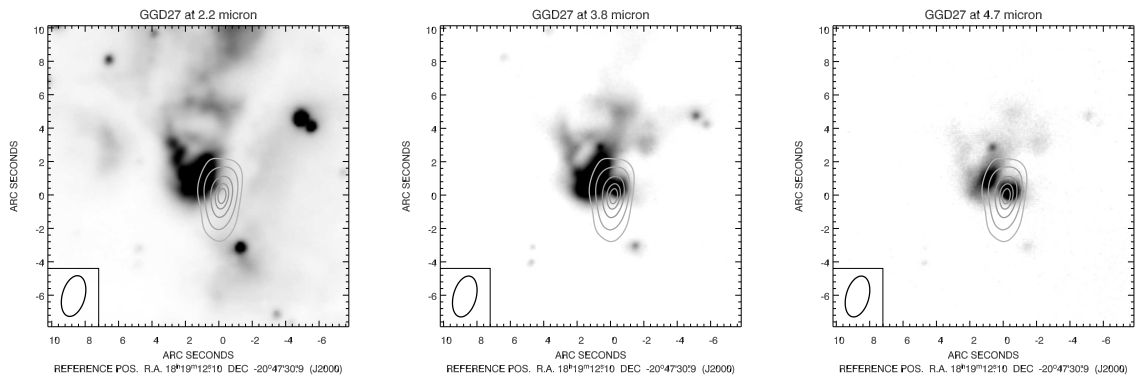


**Figure 4.3:** The vicinity of GGD 27–IRS2/ILL. The contours denote *VLA* 7-mm continuum data taken in the D array configuration. The synthesized beam size is indicated in the lower left corner. The radio source roughly coincides with IR source GGD 27–ILL.

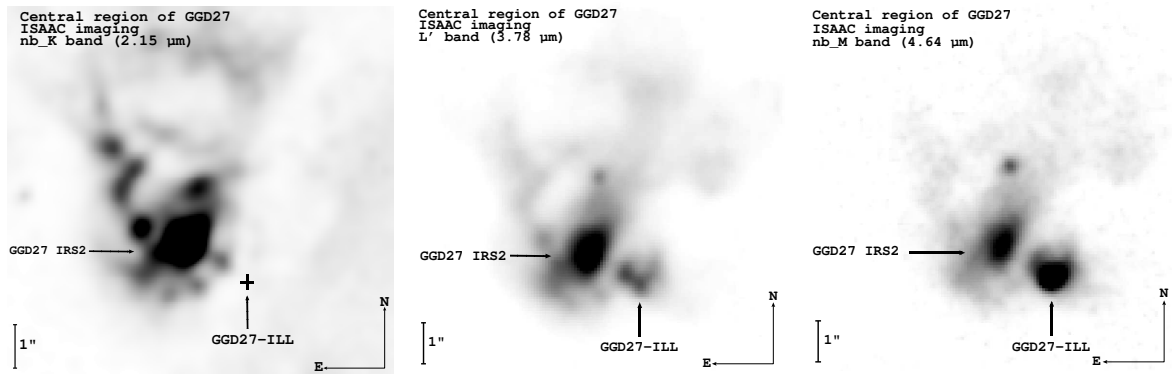


**Figure 4.4:** Immediate vicinity of GGD 27–ILL in the nb\_K band (left), L' band (middle), and nb\_M band (right), based on our *ISAAC* images. To reveal the fine structure of the sources, the images have been deconvolved with a PSF that has been generated iteratively from sources within the full *ISAAC* 27 images (see text).

First, we see in the deconvolved nb\_K band  $2.15\ \mu\text{m}$  image that the southwest border of IRS2 is not as smooth as seen in the plain images. Several compact brightness enhancements are noticeable, the strongest one is only  $0''.5$  away from the marked position of GGD 27–ILL which we here have taken as the position of the central *VLA* radio jet source (see Sect. 4.2 and Table 4.3). An infrared source is not visible at that particular position at  $2.15\ \mu\text{m}$ . It is still buried under a large slab of extinguishing material that passes through the central region from northwest towards southeast. In the L' band, the detected source at the position of GGD 27–ILL shows an inner structure. Whether this indicates the presence of two pointlike sources embedded within extended emission or just the presence of one elongated source that has a central cut (due to additional extinction) cannot be told with certainty. In the nb\_M band image, the southwestern part of the elongated structure has immensely increased in intensity and is even brighter than IRS2. This is probably a combined result of the steeply rising SED of the contained source together with wavelength–dependent optical depth effects that arise from the immediate circumstellar material as well as from the medium–scale dark lane mentioned in Sect. 4.1.1.

Here, we definitely reach the limits of conventional imaging, even if the data have been obtained under very good seeing conditions with 8-m class telescopes and have been further enhanced by deconvolution techniques. This is a prime example where adaptive optics observations in the L' and nb\_M band are desperately needed in order to clarify the situation and to prove (or disprove) the existence of several point sources with different SEDs within the elongated L' band structure associated with GGD 27-ILL.

### N-band imaging

TIMMI2 images have been obtained toward GGD 27-ILL at 8.7, 9.8, 11.7, and 18.75  $\mu\text{m}$ . We use these data mainly for assessing the mid-infrared fluxes (given in Table 4.1) of GGD 27-ILL which is the dominant source at these longer wavelengths (cf. Stecklum et al. 1997). Already in these measurements with intermediate-band filters we realise the deep depression in the mid-infrared SED around 9.7 micrometre that is caused by strong Silicate absorption. The N-band spectrum of GGD 27-ILL that we will discuss in the following Sect. 4.1.3 will (impressively) confirm this finding. The spatial resolution of the TIMMI2 data, however, is clearly lower than for the ISAAC data. Nevertheless, also here GGD 27-ILL is not pointlike but partly resolved mainly in the northeast direction.

In order to investigate further this MIR morphology, we used the opportunity to obtain imaging data with MIDI (Leinert et al. 2003), the two-element mid-infrared interferometer at the VLTI, operated by ESO on Mt. Paranal. The observations were part of a GTO observing run (PI M. Feldt, MPIA) in June, 2004. The original plan was to obtain fringes for GGD 27-ILL, but the object turned out to be too weak for interferometry at the current state of operation. A new attempt will be made as soon as the external fringe tracker FINITO is available. Nevertheless, we show here the MIDI acquisition image of GGD 27-ILL in the 12.8  $\mu\text{m}$  narrow-band filter with one of the 8.2-m Unit Telescopes and the comparison with an unresolved standard star (HD 169916) in Fig. 4.5. The images are of good quality and are diffraction limited ( $0''.39$ ) since a low-order adaptive optics correction (conveyed by the so-called STRAP Units) is applied – a feature not common for 10 micron imaging. GGD 27-ILL is clearly resolved. A bright and slightly elongated core is found in the southwest of the brightness distribution that is extended into a more shallow and conical structure toward the northeast. The general appearance resembles that of a funnel whose orientation is roughly aligned with the radio jet direction ( $17^\circ - 20^\circ$ ). We mention again, that also the L' band image (middle panel in Fig. 4.4) shows an elongated structure roughly in this direction for GGD 27-ILL. Remember that the nature of this elongated L' band structure is not clarified yet, the structure might contain a second weak IR point source (see discussion above). However, the SED of that potential secondary source seems to decline toward mid-infrared wavelengths, thus in the MIDI image we probably see just the extended emission wherein this source is immersed.



**Table 4.1:** Measured IR fluxes, corresponding magnitudes, and derived extinction for GGD 27–ILL

Filter name	L'	nb_M	N1	N2	N4	[NeII] <sup>a</sup>	Q2 <sup>b</sup>
$\lambda_{\text{cen}}$	3.78 $\mu\text{m}$	4.66 $\mu\text{m}$	8.7 $\mu\text{m}$	9.8 $\mu\text{m}$	11.7 $\mu\text{m}$	12.8 $\mu\text{m}$	18.75 $\mu\text{m}$
Flux in Jy	$1.58 \times 10^{-1}$	$5.08 \times 10^{-1}$	$0.32 \times 10^1$	$0.12 \times 10^1$	$0.73 \times 10^1$	$0.80 \times 10^1$	$6.20 \times 10^1$
Magnitude	8.01	6.28	2.99	3.57	1.48	1.20	-1.84
Extinction <sup>c</sup> [mag]	4.65	3.87	5.83	8.09	4.43	3.09	2.96

<sup>a</sup> To prevent confusion we mention that this is not a line flux measurement but just a *MIDI* narrow-band continuum filter roughly centred at the [NeII] transition wavelength.

<sup>b</sup> Contrary to the Q2 observations of G9.62+0.19–F (see Chapter 3.3), the Q2 observations for GGD 27 were conducted at a different night (though during the same observing run) when the sky conditions for Q band observations were decent.

<sup>c</sup> The extinction  $A_\lambda$  has been derived based on the results of our N–band spectrum fit and an extinction model by Weingartner & Draine (2001). We refer to Sect. 4.4.1 and to Fig. 4.7.

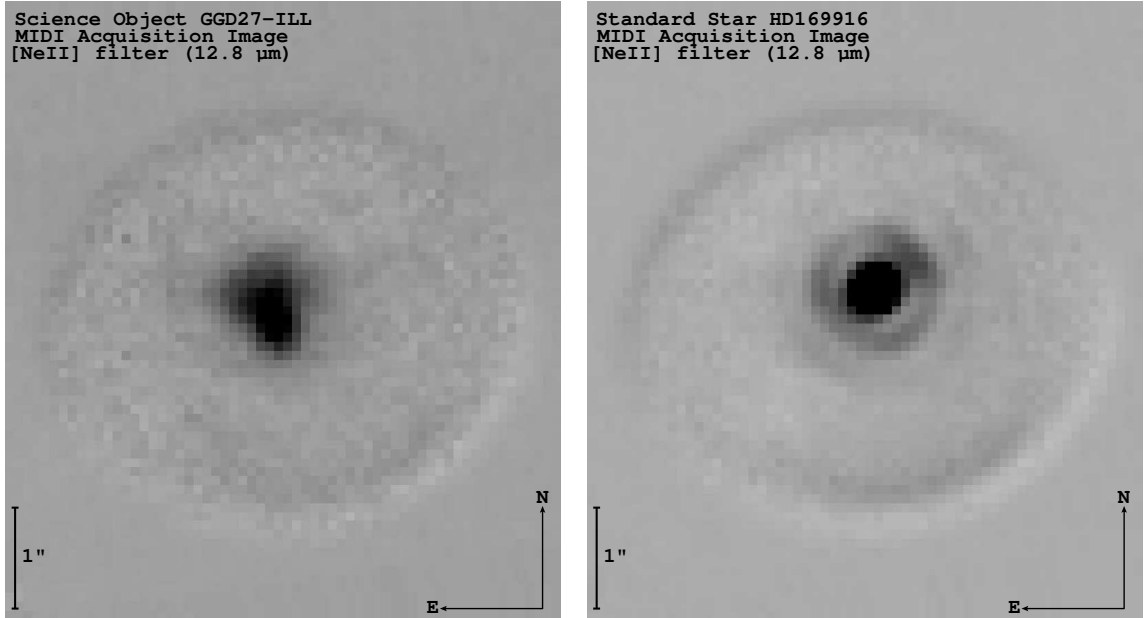


**Figure 4.5:** MIDI acquisition images of GGD 27–ILL (left) and the standard star HD 169916 (right) in the [NeII] 12.8  $\mu\text{m}$  narrow-band filter.

### 4.1.3 N–band spectrum

The *TIMMI2* N–band spectrum of GGD 27–ILL is shown in Fig. 4.6. Its main characteristic is a broad and deep Silicate absorption feature. A weak emission feature is seen at around 9.45  $\mu\text{m}$ , but it remains unidentified. This is probably an artefact caused by an imperfect cancellation of atmospheric features due to a slight wavelength mismatch between science object and calibrator. Furthermore, we report the tentative detection of the [NeII] (12.81  $\mu\text{m}$ )

line<sup>4</sup> showing a line flux of  $(1.36 \pm 0.56) \times 10^{-15}$  W/m<sup>2</sup>. Other strong lines, in particular, the common ionic N–band lines for [ArIII] (8.99  $\mu$ m) and [SiV] (10.51  $\mu$ m) are not detected. The absence of these lines in the spectrum shows that relatively weak excitation conditions are at work. The standard way to interpret the strength of these ionic lines works within the framework of (ultra–)compact HII regions (e.g., Martín–Hernandez et al. 2003, Pascucci et al. 2004). However, it is known that the central radio source coincident with GGD 27 can not be interpreted as a normal UCHII region, but as a thermal radio jet (e.g., Martí et al. 1999) which complicates the situation. At this point, we will not further investigate respective jet models and their predicted MIR line fluxes which would require extensive modelling beyond applying more or less simple formulas.

We use the spectrum to obtain a more reliable extinction estimate for the line of sight toward GGD 27–ILL. We follow the approach described in Pascucci et al. (2004). Therein, a simple model is used where the actual source of optically thick mid–infrared emission is taken as a black body of temperature  $T_d$ . This emission is then extinguished by a screen of cold dust in the foreground.<sup>5</sup> The observed flux density can be expressed as:

$$F_\nu = \Theta^2 B_\nu(T_d) \exp(-\tau_\nu). \quad (4.1)$$

Herein,  $\Theta$  is the angular diameter of the source and  $\tau_\nu$  is the optical depth of the cold extinction dust layer which is proportional to the line–of–sight column density  $N_{(\text{H}+\text{H}_2)}$ . Several authors have investigated a variety of dust extinction laws (e.g., Mathis (1990) and references therein). We use more recent synthetic extinction curves based on dust models provided by Weingartner & Draine (2001). We consider several extinction laws for which extinction coefficients are available<sup>6</sup>. Here, the assumed ratio of selective to absolute extinction  $R_V$  (see our Equ. 3.9) and the fraction of all C atoms that are built into PAHs are further characteristics of the dust models. The formally best fit for the GGD 27–ILL MIR spectrum was obtained with an Milky Way  $R_V = 5.5$  model with 30 parts per million C atoms collected in PAHs. (We use dust from their model class B where the grain volumes are kept fixed and hence do not change with varying  $R_V$ .) A list of best–fit parameters to the N–band spectrum with their formal fitting errors can be found in Table 4.2.

The total column density reported in Table 4.2 is based on the  $A_V/N_{(\text{H}+\text{H}_2)}$  calibration derived in Weingartner & Draine (2001). As a cross check we take the fitted  $\tau_{9.7\mu\text{m}}$  value, then we directly convert this into an extinction value  $A_V$ . To do this, we use an extrapolated conversion factor (CF, see Sect. 3.8) adapted to the  $R_V = 5.5$  extinction law; Cardelli et al. (1989) give simple formulas to extrapolate  $CF$  to arbitrary extinction laws. We get a visible extinction  $A_V = 116.5$  mag. Then by using our relation (3.10) for  $A_V/N_{(\text{H}+\text{H}_2)}$  we arrive at  $N_{(\text{H}+\text{H}_2)} = 1.44 \times 10^{23}$  cm<sup>−2</sup> in good agreement with the value reported above.

<sup>4</sup>When consulting the ISO archive we realised that GGD 27 has not been observed in the SWS03 setting that would have covered appropriately the 12.8 micron region although the source has been observed with several other SWS and LWS settings. So no easy comparison is possible.

<sup>5</sup>We do not distinguish between cold dust further out in the interstellar medium and that in the molecular cloud itself.

<sup>6</sup>They can be obtained from Bruce Draine’s homepage <http://www.astro.princeton.edu/~draine/>.

**Table 4.2:** Best fit parameters for the N-band spectrum of GGD 27–ILL

Parameter		Unit	Value
Temperature of emitting dust	$T_d$	K	$376.6 \pm 13.9$
Total column density	$N_{(\text{H}+\text{H}_2)}$	$\text{cm}^{-2}$	$(1.38 \pm 0.07) \times 10^{23}$
Apparent source diameter	$\Theta$	milli-arcsec	$88 \pm 3$
Estimated total luminosity <sup>a</sup>	$L_{\text{tot}}$	$L_{\odot}$	$6519 \pm 770$
Line flux [Ne II] (observed)	$F_{12.8\mu\text{m}}$	$\text{W m}^{-2}$	$(1.36 \pm 0.56) \times 10^{-15}$
Line flux [Ne II] (extinction corrected)	$F_{12.8\mu\text{m}}^0$	$\text{W m}^{-2}$	$(2.38 \pm 1.04) \times 10^{-14}$
Optical depth in the Silicate feature	$\tau_{9.7\mu\text{m}}$	–	$7.45 \pm 0.30$
Derived visible extinction <sup>b</sup>	$A_V$	mag	$116.5 \pm 4.7$

<sup>a</sup> This quantity is estimated with the simple formula  $L_{\text{tot}} = 4\pi R^2 \sigma T_d^4$  by assuming a distance of 2.0 kpc (to derive the source radius  $R$  from  $\Theta$ ) and a spherically symmetric source geometry. It has to be taken as a rough estimate.

<sup>b</sup> Based on  $\tau_{9.7\mu\text{m}}$  and a  $R_V = 5.5$  conversion factor taken from Cardelli et al. (1989)

The value of 116.5 mag in the visible can be compared to other estimates. For instance, Aspin et al. (1991) gave a lower limit of  $> 80$  mag for the visible extinction toward the GGD 27–ILL/IRS2 region, based on NIR observations and the original Rieke & Lebofsky (1985) extinction law. Furthermore, Pravdo, Tsuboi & Maeda (2004) estimate, based on X-ray observations, a column density of  $\sim 2 \times 10^{23} \text{cm}^{-2}$  for a region roughly 5 arcseconds (i.e., 10000 AU) away from GGD 27 ILL (see Sect. 4.3.1). They convert this column density to a visible extinction of 90 mag, but they do not mention explicitly the extinction law they used for this conversion.<sup>7</sup> When using our relations mentioned above and  $R_V = 5.5$ , a column density of  $\sim 2 \times 10^{23} \text{cm}^{-2}$  corresponds to  $A_V = 161$  mag.

Nevertheless, all results speak in favour of a region of high extinction that appears to be extended over a few arcseconds and is the cause of the southeast–to–northwest dark belt most prominent in the K narrow–band images (see centre of Figs. 4.1 and 4.12 or the leftmost panel in Fig. 4.3).

We find the fact, that the Weingartner & Draine (2001)  $R_V = 5.5$  model describes best our data, noteworthy for the following reason. While most authors have concluded that the wavelength dependence of interstellar extinction  $A_\lambda$  can be described by a single power law ( $A_\lambda \sim \lambda^{-\beta}$ ,  $\beta = 1.6 \dots 1.8$ ) in the wavelength range between 1 and 4  $\mu\text{m}$  (e.g., Mathis 1990, Draine 2003), the situation is not that conclusive between 4 and 9  $\mu\text{m}$ . Lutz et al. (1996) presented extinction studies based on ISO recombination line studies toward the Galactic centre that show a strong flattening of  $A_\lambda$  in the latter wavelength range, and Draine (2003) already mentioned that such a flattening also occurs for the  $R_V = 5.5$  model dust of Weingartner & Draine (2001) (most obvious in the model class B, see above). Very recently, first results of an extinction study toward two other lines of sight (Galactic longitudes  $l = 42^\circ$  and  $l = 284^\circ$ )

<sup>7</sup>After fiddling with the numbers we find that our Equ. (3.10) together with the standard interstellar extinction law  $R_V = 3.1$  gives  $A_V \approx 90$  mag.

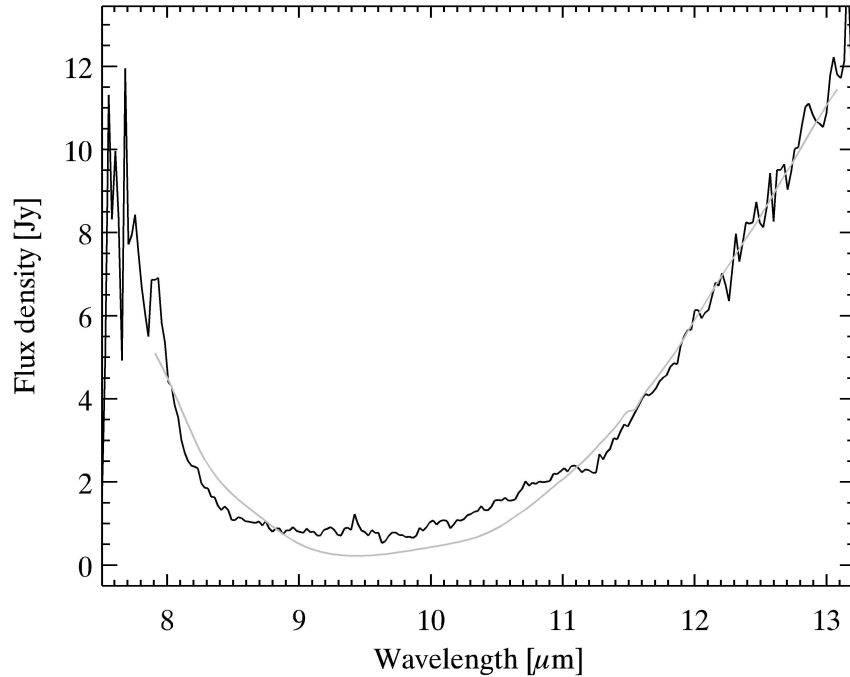


**Figure 4.6:** The *TIMMI2* spectrum of GGD 27–ILL (black line) with the best fitting dust model indicated (grey line).

based on *Spitzer* data have been published (Indebetouw et al. 2005) that are in rough agreement with the results of Lutz et al. (1996) and hence further highlight the importance of the  $R_V = 5.5$  dust model for describing interstellar extinction (see Fig. 4.7). Now, our N–band spectrum of GGD 27–ILL and the subsequent dust model fitting demonstrate that this dust model should also be considered for explaining the circumstellar extinction very close to (massive) young stellar objects.

## 4.2 Results of the VLA 7-mm imaging

We imaged the GGD 27 centre region at 7-mm with the *VLA* by applying the maser cross-calibration method as explained in Sect. 2.3 and in more detail in Appendix D. This technique not only gives a map of the central source in the 7-mm continuum. It provides us in addition with an interferometric map of the 44-GHz Methanol masers with a spectral resolution corresponding to 0.33 km/s free of charge.

### The 7-mm continuum source

The prime result of the continuum mapping is shown in Fig. 4.8 and a larger map is used in Fig. 4.10. The synthesised beam width is  $0''.27 \times 0''.14$  when using natural weighting. We find one point source at the coordinates  $\alpha_{2000} = 18^{\text{h}}19^{\text{m}}12^{\text{s}}.092$ ,  $\delta_{2000} = -20^{\circ}47'30''.95$ . This is in good agreement (see Table 4.3) with the position of the central jet–driving source as

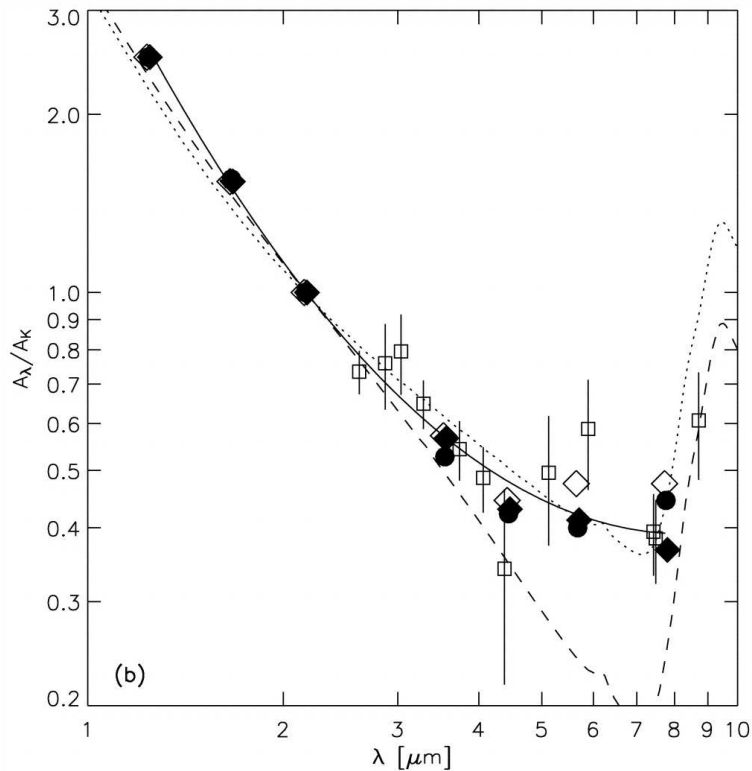


**Figure 4.7:** Measurements and models of the relative extinction in the infrared, taken from the recent publication by Indebetouw et al. (2005) – their Fig. 6b. Solid circles, solid diamonds, and open diamonds denote the values based on their *Spitzer* measurements and 2MASS data toward three lines of sight, the solid line shows a fit to these data. The *ISO* results toward the Galactic centre by Lutz et al. (1996) are added as open squares with error bars. The broken lines show the theoretical curves from Weingartner & Draine (2001) for  $R_V = 5.5$  – their case A is shown by a dashed line, their case B (i.e., the model that fits best our N-band spectrum of GGD 27-ILL) is shown by a dotted line.

reported by Martí et al. (1999) and this is also roughly ( $\pm 0''.5$ ) the expected position for GGD 27-ILL. We find a total flux of  $(9.8 \pm 0.4)$  mJy for this 7-mm source. No other sources have been detected, although the rms noise in the final natural-weighted image is as low as 0.16 mJy/beam.

The 7-mm source appears unresolved when using natural weighting. To increase the resolution of the map we applied several different weighting schemes (ROBUST weighting, Briggs 1995) for the uv data. This decreases somewhat the sensitivity, but improves the poor beam shape with respect to a natural-weighted map. While ROBUST = +5 is comparable to natural weighting, one can lower this value to more and more affect the beam. With extreme weighting (ROBUST = -5) we can reach synthesised beam sizes of  $0''.19 \times 0''.10$ . We can now attempt to measure the deconvolved source size (by deconvolving with the synthesised beam) utilising the *AIPS* routine *JMFIT*. With a one-component fit we come to the following conclusions. The synthesised beam orientation is almost north in all the cases ( $-2.67^\circ$  for natural weighting,  $-0.62^\circ$  for ROBUST = -5). However, the deconvolved source orientation angle changes noticeably ( $-9.2^\circ$  for natural weighting,  $-19.6^\circ$  for ROBUST = -3, and finally  $-26.5^\circ$  for ROBUST = -5). Thus, the more we get susceptible to finer spatial scales the more

the source orientation turns out to be inclined with respect to the orientation of the ionised jet which is  $+17^\circ$  (compare the left and right panel of Fig. 4.8). We see in this figure that the 1.3 cm emission appears to be dominated by the ionised jet. (We mention that these 1.3 cm data have the same spatial resolution as our 7-mm data treated with ROBUST = -5.) The rotation of the deconvolved source position angle indicates that at 7 mm a second structure within the central source might contribute to the total signal. A potential collimating structure for the ionised radio jet can be expected to be strongly inclined to the jet axis.

It turns out that it is difficult to make this change of source orientation, or any source structure at all, visible in the plain undeconvolved maps. We encounter a certain limit for what can be done with the uv data. The resulting maps turned out to be quite sensitive to parameters like the total map size or the cellsize used for the imaging. Furthermore, our attempts failed to make a two-component Gaussian fit, where one component is kept fixed oriented along the jet axis and one component is free to vary in orientation and strength. No meaningful stable solutions could be found. However, we mention that the change of the deconvolved source position angle in the one-component fit remains a robust result.

The question arises if we indeed have detected a contribution from dust emission. We have to consider that the free-free emission from an ionised collimated jet can have a spectral index  $\geq 0.6$  (Reynolds 1986). Martí et al. (1999) find for our jet-driving source the relation  $S_\nu \propto \nu^{0.8 \pm 0.1}$ . From their 1.3 cm observations (left panel of Fig. 4.8) they derive  $S_{1.3\text{cm}} = 4.8 \pm 0.2$  mJy. By extrapolating this flux density with the given power law we expect  $(8.3 \pm 0.9)$  mJy as contribution from free-free emission for our 7-mm data. A comparison with our measured 7-mm flux of 9.8 mJy does not allow for a large dust contribution. However, we should mention that Gómez et al. (2003) reported a total flux of 14 mJy based on their VLA C-array 7-mm observations (beam size  $\sim 0.5$  arcseconds), and in our D-array 7-mm data (Hofner, Araya, Linz, et al. in preparation, but see Fig. 4.3) which have a beam size of around 2 arcseconds we find almost 20 mJy as total flux. This might indicate that a considerable fraction of the signal is contained in structures for which we are not sensitive enough in extended array configurations. Nevertheless, we cannot exclude that the general flux calibration is affected. Note, for instance, that for our observations, the total CH<sub>3</sub>OH maser emission (see next paragraph) integrated over the entire maser area is just 74.1 Jy in the strongest channel (see also the right panel of Fig. 4.9), while Kurtz, Hofner & Vargas Álvarez (2004) report 154.02 Jy. A suspicious factor of 2 appears to be present. We have re-checked our data reduction, but no obvious error could be found. As the bottom line, we conclude that at this stage no reliable value for the dust emission contribution for GGD 27 can be given. It might be as small as 1 mJy, but it is not unlikely that the dust contribution is clearly higher.

### The 44-GHz Methanol masers

The existence of 44 GHz methanol maser emission near to the centre of GGD 27 has already been reported in the single dish survey of Kalenskii et al. (1992) and by Slysh et al. (1999, hereafter S99). Our new VLA data are comparable in resolution to the S99 data which pre-

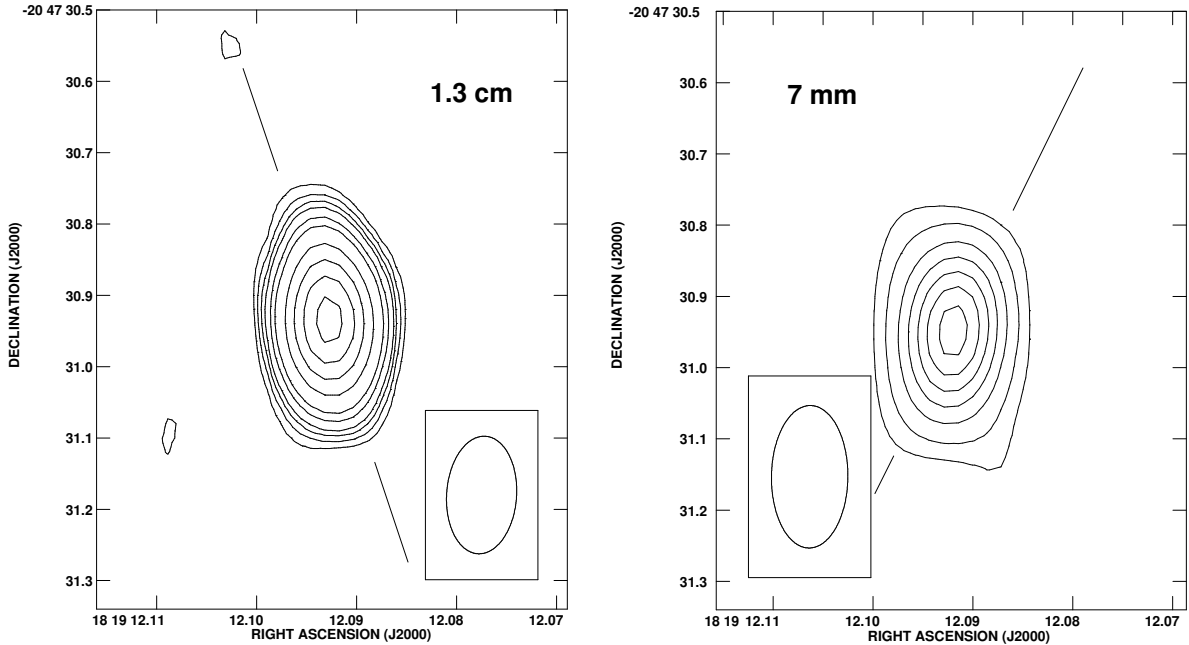


**Figure 4.8:** The comparison between our VLA 7-mm B-array observations and the VLA 1.3-cm A-array observations of Martí et al (1999). The size and orientation of the synthesised beams are shown in the insets. The deconvolved position angles are indicated as lines. While in case of the 1.3 cm map, the PA is roughly aligned with the orientation of the radio jet ( $17^\circ$ ), the deconvolved PA in the 7-mm case (derived from the ROBUST= $-5$  map) is clearly inclined with respect to the jet orientation and attains  $-26.5^\circ$ .

sented snapshot observations using 11 VLA antennas. However, due to the setup of our cross correlation measurements we have a quasi-continuous hour-angle coverage over more than 3 hours with 24 antennas, effectively (after flagging bad antennas). This might explain the differences between our results. S99 present one strong maser spot which they resolve into two spots when applying superresolution with a 50 milliarcsec restoring beam. We reveal a small cluster of at least 10 maser spots mainly arranged in a bow shape and showing a distinct velocity structure (Fig. 4.9). Furthermore, S99 reported a quite rough estimation of the maser position with several arcsecs of uncertainty which was probably caused by the limitations of the approach to determine the absolute positions from the observed fringe rates. Let us for a moment consider the theoretical possibility that proper motion of the maser spots might cause the positional difference of ca.  $2''.8$ . The S99 observations were performed 5.5 years before our observations. Assuming a distance of 1.7 kpc to GGD 27 (in order to compare the velocities with values from the literature), the proper motion velocity must be  $\gtrsim 4000$  km/s to account for the positional difference, a very high value. For comparison, Martí et al. (1995, 1998) give a velocity of roughly 500 km/s for the HH 80/81 radio jet and give a projected proper motion of  $(60 \pm 15)$  mas/yr for the youngest (i.e., younger than 1990) ionised condensations within the jet. We admit, however, that outer (older) jet condensations

show proper motions of up to 180 mas/yr (Martí et al. 1995).

Nevertheless, to ensure an accurate astrometry for our data we independently checked it in two ways<sup>8</sup>. Before the actual cross calibration observations we did 3 minutes of fast switching between the maser field and the nearby calibrator 1820–254 whose position is known with high precision. The bootstrapped position of the strongest feature in these snapshots is in very good agreement with the maser positions from the cross calibration observations. Furthermore, as explained in Sect. 2.3, we externally calibrated the maser data in phase using the source 1733–130 before we finally applied the selfcalibration. Also in this intermediate step the maser positions were consistent with the final selfcalibration astrometry. We estimate our astrometric accuracy to be in the order of 30 milliarcsecs. As a main result, the maser cluster is not coincident with the position of IRS2, which was still assumed in S99. In contrary, the masers are just 1 – 2 arcsecs away from the mm continuum source CS3 detected by Yamashita et al. (1991) at 2.6 mm (CS3 was confirmed by Gómez et al. (2003) at 1.4 mm.). This continuum source is associated with the central ammonia core C (Gómez et al. 2003, see Fig. 2.2). Thus, certain parts of the ionised jet (and potential material entrained by it) probably hit the gas of the resting molecular core, and these shocks give rise to the CH<sub>3</sub>OH maser emission. It is interesting to note that the LSR velocities of the maser emission (12 – 15 km/s) is not much different from the systemic velocities of the normal molecular emission in the GGD 27 region (11 – 13 km/s), contrary to the far blue-shifted velocity of the neighbouring H<sub>2</sub>O maser found by Gómez et al. (1995) that attains –58.4 km/s.

The strongest Methanol maser spot, found at the J2000 position: RA 18<sup>h</sup>19<sup>m</sup>12<sup>s</sup>.410, Dec –20°47′22″.73, coincides with a weak near-infrared source. This source is already seen in the plain K narrow-band images and becomes obvious as a point source when deconvolving the images following the approach mentioned in Sect. 4.1.2 for the L' and nb\_M band images. The object does not seem to possess a strong H<sub>2</sub> or Brackett  $\gamma$  excess, but rather appears to be a continuum object embedded within a small halo of extended emission.

## 4.3 Additional sources in the GGD 27 vicinity

### 4.3.1 The X-ray sources in GGD 27 and their IR counterparts

Recently, Pravdo, Tsuboi & Maeda (2004) published their results about X-ray observations toward the GGD 27 / HH80–81 complex. They used the ACIS–S detector system on the *Chandra* X-ray satellite observatory. Although their main focus was to reveal X-ray emission of the Herbig–Haro objects HH80–81 they also covered the central region of GGD 27 including the jet-driving source. However, since this central field was situated on the edge of one of the detector chips  $\sim 5'$  off-axis, the resulting PSF for this area is more extended and asymmetric. We show one of their results in our Fig. 4.11. Hereby, green contours denote

<sup>8</sup>Controlling the absolute astrometry is especially important when applying selfcalibration.



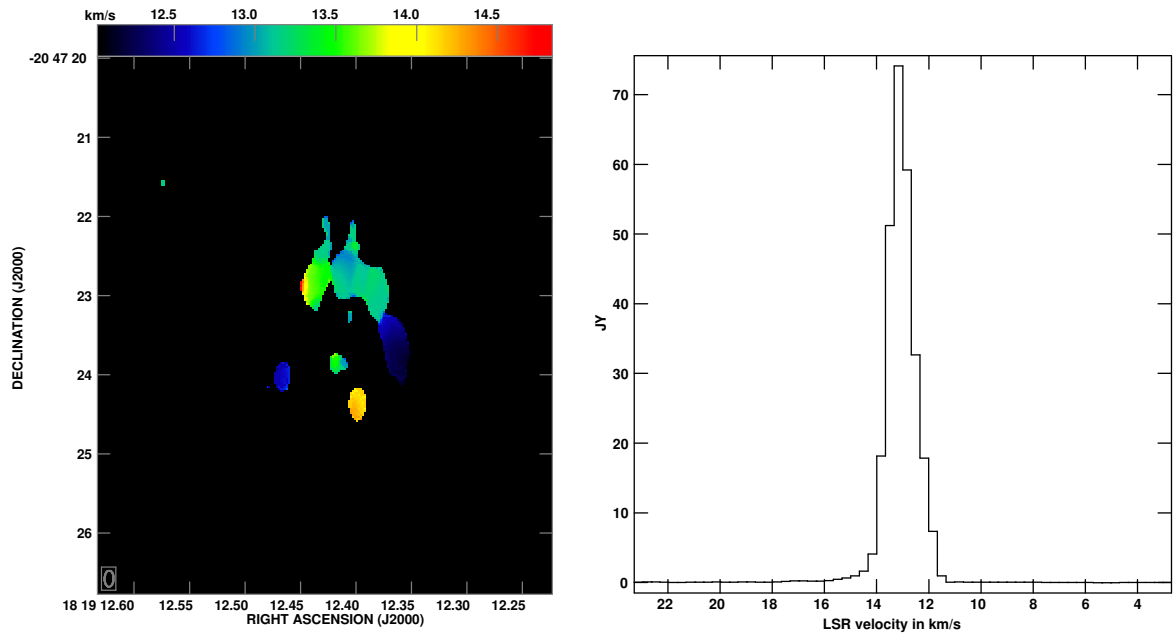


**Figure 4.9:** The main cluster of 44 GHz methanol masers to the northeast of the central jet source. **Left:** The maser map colour-coded using the velocities occurring in the maser cluster. **Right:** The integrated spectrum of the entire 44 GHz maser region.

X-ray sources, red squares show the position of *VLA* radio sources according to Martí et al. (1993) while black circles indicate prominent IR sources (Stecklum et al. 1997). In Fig. 4.12 we plot the X-ray positions of all *Chandra* sources found within the field-of-view of our *ISAAC* K narrow-band imaging. In Table 4.4 we list these 11 X-ray sources and give the coordinates of potential IR counterparts we find in our K narrow-band imagery. Since the *Chandra* PSF and astrometry might be slightly degraded we allow for a maximum distance of 2'' (4000 AU) to identify X-ray with IR sources. Using this criterium, all of these 11 X-ray sources might be associated with IR point sources. For 9 of the 11 sources, already the 2MASS catalogue provides potential candidates. Our *ISAAC* images, however, have a higher spatial resolution ( $\sim 0''.45$ ) than 2MASS images and often reveal two sources near the X-ray position. Consequently, we list both IR sources in these cases.

Furthermore, our *ISAAC* data reveal a very faint IR counterpart for source No 69 (source 181912.0–204703 in Fig. 4.11). It is hard to distinguish this faint IR source from the strong extended IR emission arising from the northern part of the wishbone-shaped IR reflection nebula. No point source is visible at this position in our L'- and nb\_M band images.

The X-ray source No 72 (source 181912.4–204733), which is located near to the jet-driving source (marked as MRR 14 in Fig. 4.11), is of special interest since it is strong, but without a previously known IR counterpart. We will discuss it here in some more detail.

### The source CXOPTM J181912.4–204733 (No 72)

This relatively strong and hard X-ray source is found near to, but not coincident with MRR14. The authors state that the astrometric accuracy is degraded to  $> 1''$  near the chip edges, but the found offset of  $> 4''$  is significant. The X-ray spectrum of this source is un-

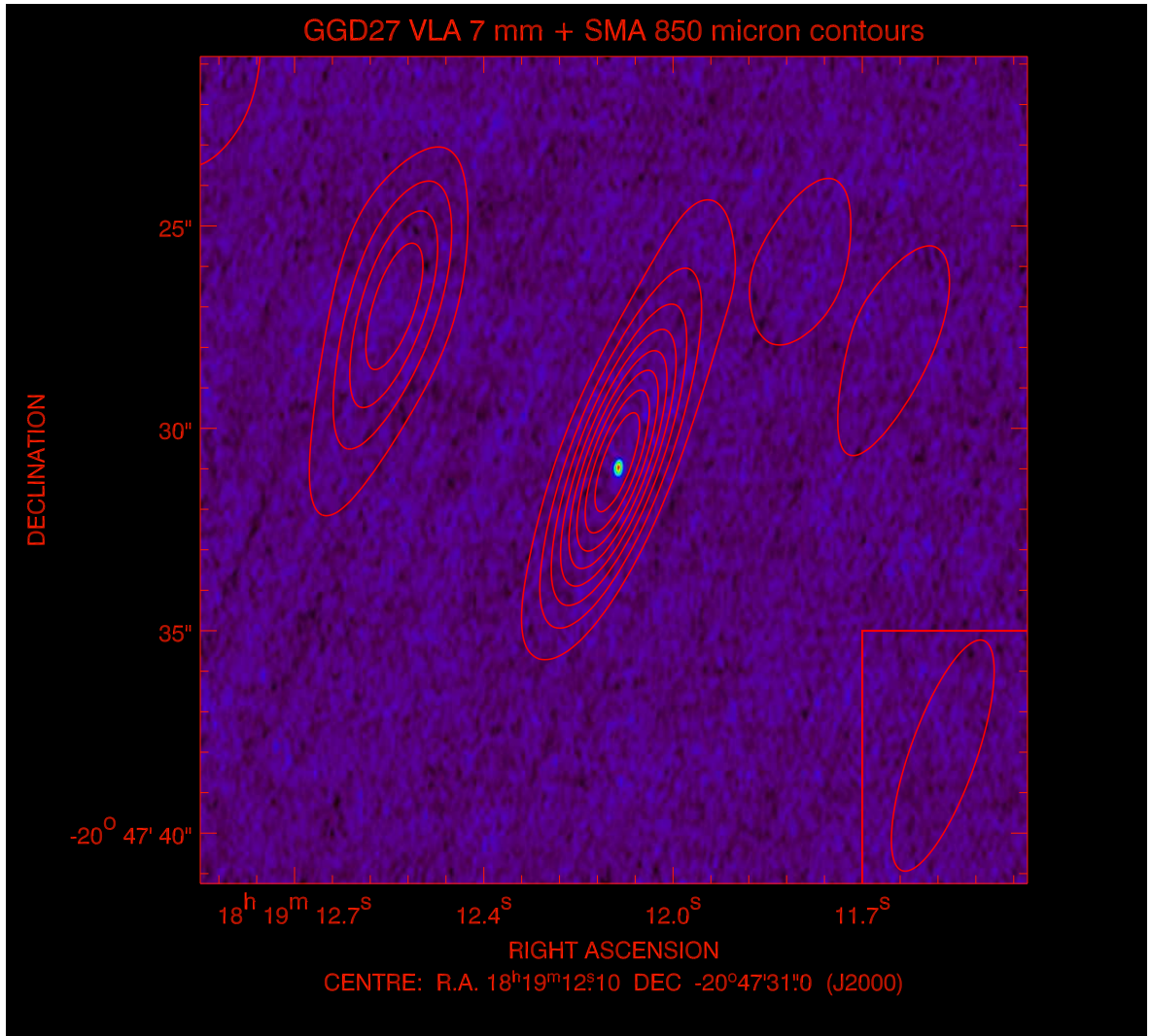


**Figure 4.10:** Our B-array VLA 7-mm observations of GGD 27, overlaid with contours derived from interferometric SMA 850 micron observations, courtesy of N.-Y. Su (see Su 2004). The synthesized beam of the VLA observations is very small ( $\sim 0''.2$ ) and is not drawn here. The size of the SMA synthesized beam ( $6''.0 \times 1''.6$ ) is indicated in the lower right corner. The second 850 micron source to the northeast of the central source coincides with the region containing the weak cm radio source VLA3 and the associated  $\text{H}_2\text{O}$  maser (Gómez et al. 1995, see also Table 4.3).

usual, highly absorbed by X-ray standards. Pravdo et al. (2004) derive a column density of  $\sim 2 \times 10^{23}$  H atoms  $\text{cm}^{-2}$ , corresponding to an extinction of roughly  $A_V = 90$  mag. They propose two alternative scenarios. The X-ray emission might come from shocks near the base of the jet driving source. Alternatively, the emission might be caused by an extincted pre-main sequence star.

Although our infrared data do not allow to draw a final conclusion, they strongly lend support to an interpretation involving one or more extincted (PMS) stars. In our K narrow-band data we find two faint star-like sources near the X-ray position, roughly oriented north-south (separation  $1''.0$ ). The northern of the two source is nearer to the nominal X-ray source position and is located in only 0.6 arcseconds projected distance to it. These two sources are

**Table 4.3:** Compilation of positions of features in the GGD 27 region

Feature	RA(J2000) (h m s)	DEC(J2000) (d m s)	Reference
HH 80 <sup>(1)</sup>	18 19 06.09	−20 51 49.1	Reipurth & Graham (1988)
HH 81 <sup>(1)</sup>	18 19 06.67	−20 51 06.0	Reipurth & Graham (1988)
HH 80 N	18 19 19.74	−20 41 34.9	Martí et al. (1993)
HH 80 N NH <sub>3</sub> (1,1)	18 19 18.60	−20 40 53.2	Girart et al. (1994)
IRAS 18163–2042	18 19 20.09	−20 40 57.0	IRAS catalogue
IRAS 18162–2048	18 19 11.90	−20 47 34.0	IRAS catalogue
radio jet central source <sup>(2)</sup>	18 19 12.09	−20 47 30.9	Martí et al. (1999)
southeast CO(1–0) peak	18 19 19.30	−20 48 00.1	Benedettini et al. (2004)
CXOPTM J181912.4–204733	18 19 12.43	−20 47 33.7	Pravdo, Tsuboi & Maeda (2004)
H <sub>2</sub> O maser	18 19 12.51	−20 47 27.4	Gómez et al. (1995)
VLA 3	18 19 12.48	−20 47 27.4	Gómez et al. (1995)
1.4-mm BIMA main peak	18 19 12.13	−20 47 30.6	Gómez et al. (2003)
1.4-mm BIMA secondary peak	18 19 12.49	−20 47 23.3	Gómez et al. (2003)
NH <sub>3</sub> (2,2) Central	18 19 12.55	−20 47 25.4	Gómez et al. (2003)
NH <sub>3</sub> (1,1) South	18 19 11.94	−20 48 29.3	Gómez et al. (2003)

<sup>(1)</sup> By means of Hubble WFPC2 images Heathcote et al. (1998) reveal a wealthy substructure within HH 80–81. Since we compare these positions just with the low resolution SIMBA data (beam size 24 arcsecs), we only report these mean positions of the HH–blobs for comparison.

<sup>(2)</sup> This source is generally assumed to be associated with GGD 27–ILL.

neither listed in the 2MASS catalogue nor visible in previous NIR images of GGD 27 in the literature because of their faintness. (Due to the cut levels and the slight smoothing effect of the wavelet filtering applied to the images, the two stars are also “dissolved” in Fig. 4.3.) However, also our L’ and nb\_M images clearly show both sources (see Fig 4.2). Interestingly, the flux ratio changes with increasing wavelength. While at 2.15 micron the northern source is stronger than the southern one by a factor of  $\geq 1.5$ , this ratio is finally reversed, with the southern source being stronger by a factor of 1.5 at 3.78  $\mu\text{m}$  and by a factor of 1.8 at 4.66  $\mu\text{m}$ . In addition, the southern source appears slightly more extended than the northern source at longer wavelengths.

Based on their extinction estimate, Pravdo, Tsuboi & Maeda (2004) find an unabsorbed X–ray luminosity of  $\sim 2 \times 10^{32} \text{ erg s}^{-1} = 2 \times 10^{25} \text{ W} \cong 5.2 \times 10^{-2} L_{\odot}$ . They mention that low– and intermediate–mass PMS stars have an  $L_X/L_{\text{bol}}$  ratio typically of a few  $10^{-4}$ , while for young high–mass stars the ratio can drop down to values of  $10^{-6} \dots 10^{-7}$  (see also Feigelson et al. 2002). If we assume that indeed a hidden massive star is associated with the X–ray emission, its total luminosity would be  $\geq 5.2 \times 10^4 L_{\odot}$ . Hence, there should be an obvious imprint of this source in the SED of the central region of GGD 27. However, we do not

**Table 4.4:** X–ray sources found by Pravdo, Tsuboi & Maeda (2004) within the ISAAC FOV

Number <sup>1</sup>	X–ray position		Remarks <sup>2</sup>	IR position(s)	
	RA(J2000) (h m s)	DEC(J2000) (d m s)		RA(J2000) (h m s)	DEC(J2000) (d m s)
59	18 19 09.19	–20 47 16.4	2MASS	18 19 09.21	–20 47 14.7
				18 19 09.09	–20 47 15.0
62	18 19 10.49	–20 46 58.1	IRS 4 <sup>3</sup>	18 19 10.51	–20 46 57.8
63	18 19 10.83	–20 47 48.5	2MASS	18 19 10.79	–20 47 48.2
66	18 19 11.76	–20 47 27.2	IRS 8 <sup>4</sup>	18 19 11.76	–20 47 26.2
				18 19 11.71	–20 47 26.7
67	18 19 11.78	–20 48 03.6	2MASS	18 19 11.87	–20 48 03.0
68	18 19 11.86	–20 47 40.6	2MASS	18 19 11.85	–20 47 40.7
				18 19 11.80	–20 47 40.6
69	18 19 12.03	–20 47 03.1	–	18 19 12.03	–20 47 03.6
72	18 19 12.43	–20 47 33.7	–	18 19 12.46	–20 47 34.1
				18 19 12.47	–20 47 35.1
76	18 19 13.65	–20 47 50.6	2MASS	18 19 13.64	–20 47 50.5
				18 19 13.67	–20 47 51.1
77	18 19 13.70	–20 47 51.0	2MASS	18 19 13.64	–20 47 50.5
				18 19 13.67	–20 47 51.1
81	18 19 14.90	–20 47 15.0	2MASS	18 19 14.84	–20 47 14.5
				18 19 15.00	–20 47 15.1

<sup>(1)</sup> X–ray source number in the list of Pravdo, Tsuboi & Maeda (2004)

<sup>(2)</sup> indicates previously known associated sources

<sup>(3)</sup> IRS 4 is not pointlike in the ISAAC image but slightly elongated north–south.

<sup>(4)</sup> For the first time, our IR imaging proves that IRS 8 is a double source, where the weaker southeast IR component is coincident with the optical source HL 34 (Hartigan & Lada 1985).

detect a source at this position in our data at  $\lambda \geq 5 \mu\text{m}$ . Also the interferometric maps at  $850 \mu\text{m}$  (Su 2004, see Fig. 4.10) and at 1.4 mm (see Gómez et al. 2003) lack any excess emission above the noise level at the X–ray position. We therefore conclude that the X–ray emission is probably caused by an intermediate–mass star not exceeding a few hundred solar luminosities.

### 4.3.2 New millimeter continuum clumps

In addition to the previously known millimeter continuum clumps in GGD 27 (e.g., Yamashita et al. 1991), several authors revealed the presence of clumps of dense molecular gas in the farther vicinity of GGD 27 for which a relation to dust continuum emission was not

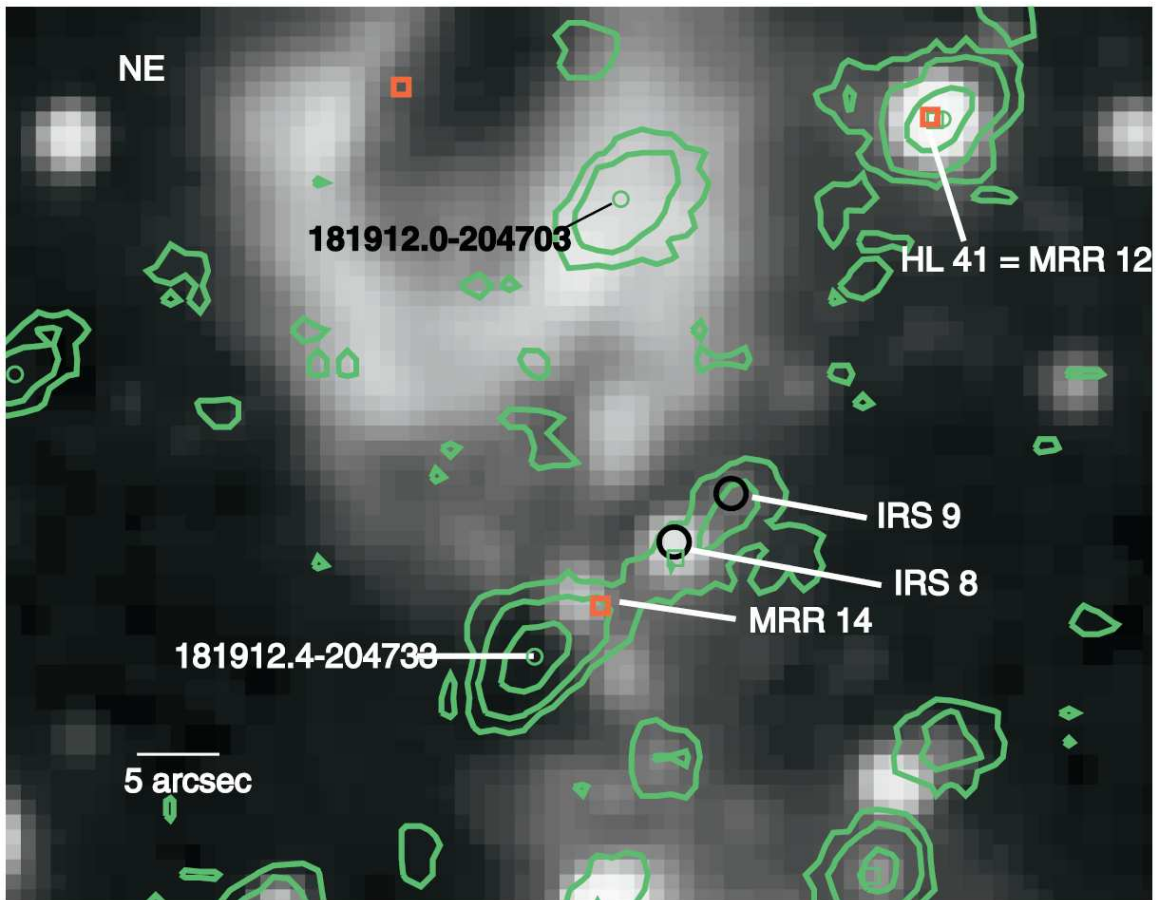


**Figure 4.11:** The Chandra X-ray data for the central region of GGD 27 (green contours) overlaid on a grey-scale 2MASS Ks band image of that region, taken from Pravdo, Tsuboi & Maeda (2004). MRR 14 is the central source position of the ionised radio jet, the neighbouring X-ray source 181912.4-204733 coincides with the position of two faint IR sources in our ISAAC images.

established up to now.

1. Girart et al. (1994) found Ammonia  $\text{NH}_3(1,1)$  emission downstream from HH 80N, even further away from the jet-driving source, but not along the jet axis. It was speculated whether this clump is associated with the weak IRAS 60 micron source 18163-2042 ( $F_{60\mu\text{m}} \approx 4.7$  Jy).
2. Gómez et al. (2003) found a core traced by  $\text{NH}_3(1,1)$  more than 1 arcmin south of GGD 27 IRS2. This clump seems not to be related to other sources previously known, although one knot of the radio jet (source VLA 13 from Marti et al. (1993)) is located nearby. Also here the question is whether the clump is just irradiated by parts of the jet.
3. Finally, Benedettini et al. (2004) found a secondary peak in their large-scale CO(1-0) maps of GGD 27 ca.  $90''$  to the southeast of GGD 27 IRS2. A red 2MASS source seems to be associated to it.

The ability of *SIMBA* to efficiently map large fields enabled us to look for continuum emission emerging from these cores. Here we report the detection of 1.2-mm continuum sources

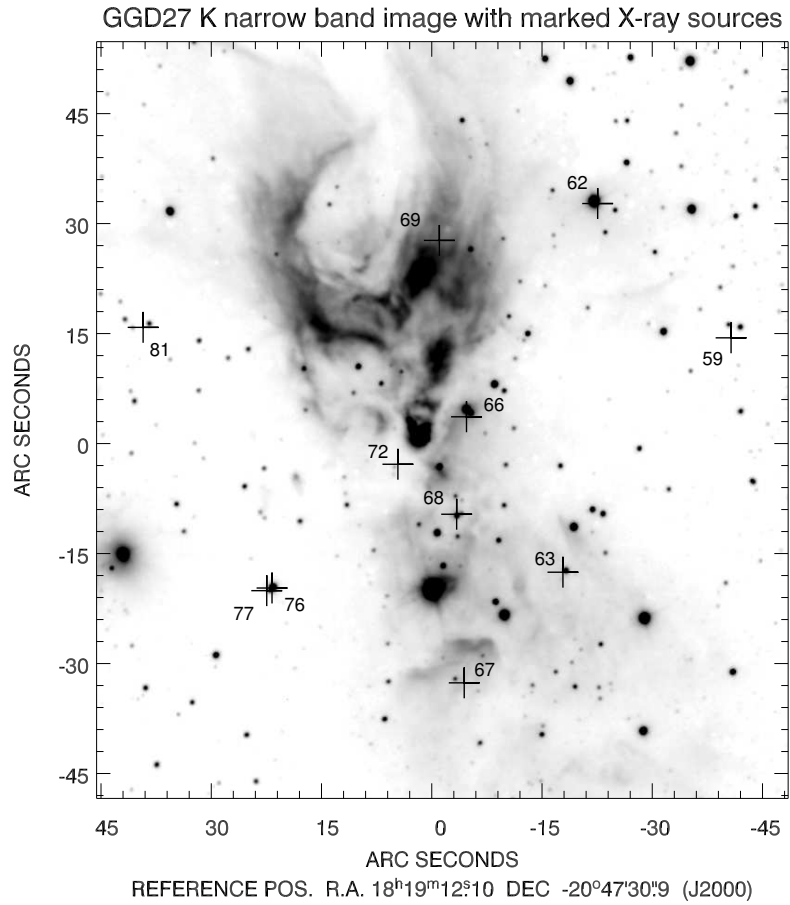


**Figure 4.12:** Our combined K narrow-band images of the GGD 27 region with marked X-ray source positions (found by Pravdo, Tsuboi & Maeda 2004) that lie within the *ISAAC* field-of-view (for the numbering see Table 4.4).

we find near to the above-mentioned molecular cores. We show our results in Fig. 4.13 where we overlay our *SIMBA* data as contours on an *MSX* mid-infrared image. The clumps are listed in Table 4.5, where we also give the measured fluxes and estimated masses for these clumps. We use the standard formula

$$M_{\text{dust}} = \frac{F_{\nu} d^2}{\kappa_{\text{m}} B_{\nu}(T_{\text{d}})}. \quad (4.2)$$

Herein  $d$  is the distance to the object (we assume 2.0 kpc for all the clumps),  $\kappa_{\text{m}}$  is the mass absorption coefficient for the dust (we adopt a value of  $1.0 \text{ cm}^2 \text{ g}^{-1}$  for  $\lambda = 1.2 \text{ mm}$  following Ossenkopf & Henning (1994)), and  $B_{\nu}(T_{\text{d}})$  is the Planck function for the (dust) temperature  $T_{\text{d}}$ . We mention that the used temperatures are rough estimates at best. In particular, for MM2 and MM3 we use the  $\text{NH}_3$  rotational temperatures reported in Girart et al. (1994) and Gómez et al. (2003). After certain corrections (described, for instance, in Walmsley et al. 1983 or Danby et al. 1988)  $\text{NH}_3$  measurements can be used as sensitive thermometers. However, it is not obvious if such corrections have been applied in our case. Hence, the reported rotational temperatures probably have to be taken as lower limits for the kinetical

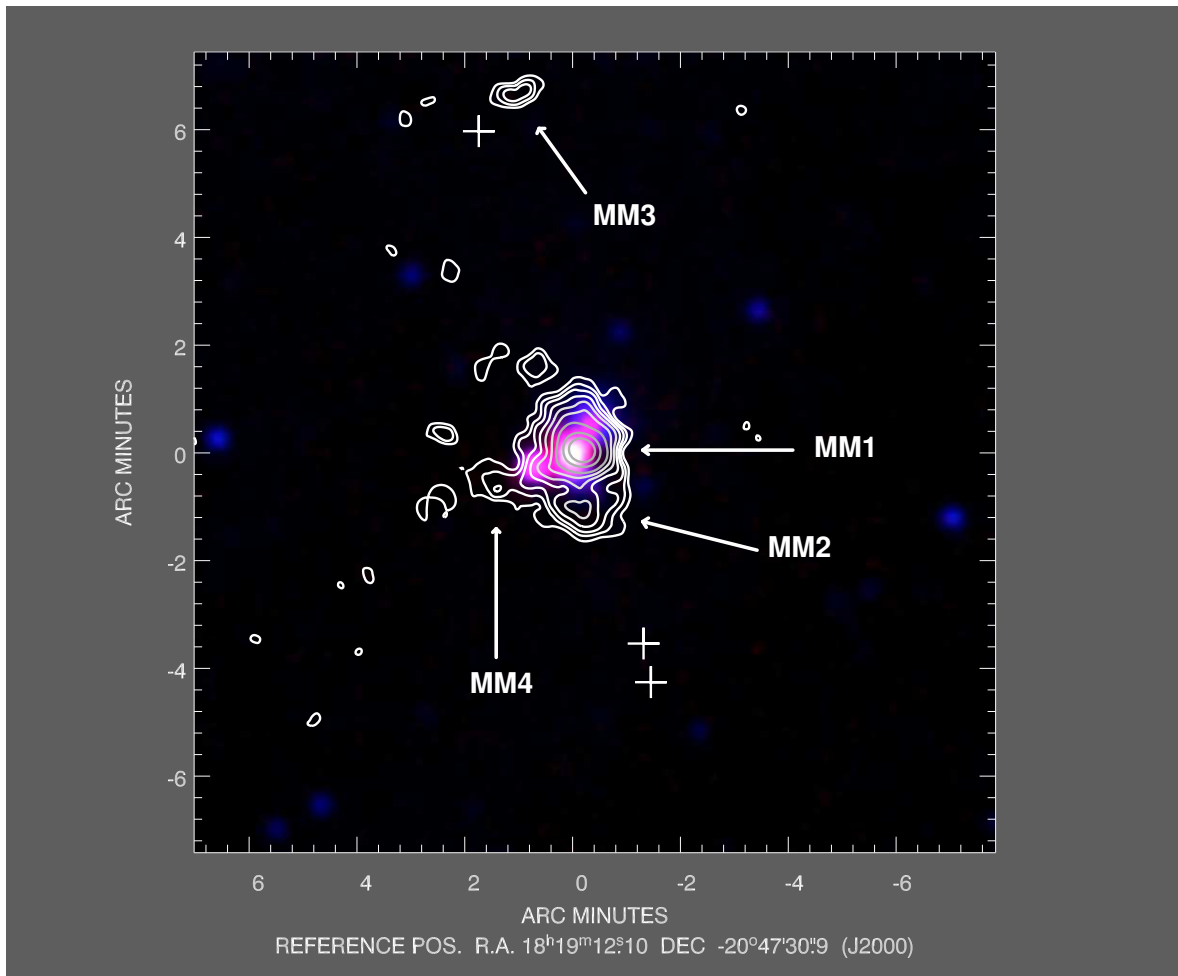


**Figure 4.13:** A three-colour composite of MSX data toward GGD 27. The coding is: blue for the A band ( $8.3 \mu\text{m}$ ), green for C + D band ( $12.1 \mu\text{m}$  and  $14.7 \mu\text{m}$ ), and red for the E band ( $21.3 \mu\text{m}$ ). As contours the 1.2 mm data of our *SIMBA* mapping are shown. The plus signs denote the position of the Herbig–Haro objects HH 80, 81, and 80N (cf. Table 4.3). The arrows point to the millimetre clumps we also list in Table 4.5.

gas temperature and hence for the dust temperature.<sup>9</sup> Consequently, the dust masses at least for MM2 and MM3, as listed in Table 4.5, are probably overestimated by 10 - 50 %.

## 4.4 Discussion

### 4.4.1 The central source

#### Radiative transfer modelling and its limitations

We use a self-consistent 1D radiative transfer model (*MODUST*, see Bouwman 2001, Kemper et al. 2001) to get an idea about the energetics of GGD 27–ILL and to estimate the limitations for such a spherically symmetric model in our case.

<sup>9</sup>In dense molecular gas a coupling of kinetical gas temperature and dust temperature is expected for gas densities  $\geq 10^5 \text{ cm}^{-3}$  (e.g., Krügel & Walmsley 1984).

**Table 4.5:** Measured 1.2-mm fluxes for recognised mm features within the GGD 27 region

Source No	Related Feature	RA(J2000) <sup>(1)</sup> (h m s)	DEC(J2000) <sup>(1)</sup> (d m s)	1.2-mm Flux (Jy)	Dust Mass ( $M_{\odot}$ )	Temperature (K)
MM1	Central Region	18 19 11.37	-20 47 27.8	$6.17 \times 10^0$	$1.78 \times 10^0$	35 <sup>(2)</sup>
MM2	NH <sub>3</sub> South core	18 19 11.59	-20 48 35.0	$6.66 \times 10^{-1}$	$6.72 \times 10^{-1}$	10 <sup>(3)</sup>
MM3	HH 80-N NH <sub>3</sub>	18 19 16.46	-20 40 46.8	$2.12 \times 10^{-1}$	$1.43 \times 10^{-1}$	15 <sup>(4)</sup>
MM4	Southeast CO Peak	18 19 18.32	-20 48 10.2	$2.79 \times 10^{-1}$	$1.40 \times 10^{-1}$	20 <sup>(5)</sup>

(1) See Sect. 2.2.5 for remarks about the positional accuracy of our *SIMBA* measurements.

(2) used in the modelling of Yamashita et al. (1990)

(3) upper limit of NH<sub>3</sub>  $T_{\text{rot}}$  according to Gómez et al. (2003)

(4) NH<sub>3</sub>  $T_{\text{rot}}$  according to Girart et al. (1994)

(5) no constraints from literature, 20 Kelvin is assumed

In *MODUST*, a Kurucz (1993) model star, taken from a grid of models with  $T_{\text{eff}}$ ,  $R_*$ , and  $\log(g)$  as parameters, is placed within the center of a configuration of concentric dust shells where the dust density decreases toward the outer boundary obeying a power law. Several sorts of dust with power law size distributions can be included.

The fact that in this work we have compiled a comprehensive set of high-spatial resolution measurements of GGD 27-ILL is a major advantage. For most of the data (excluding the IRAS 60 and 100 micron points, of course) we can be sure that they reflect the properties of GGD 27-ILL itself and do not include large areas comprising other sources which would tamper our inferences. Furthermore, the data comprise a large wavelength range which sets important constraints on the modelling. These constraints become even more strict when we take the shape and flux levels of the N band spectrum into consideration.

We have varied several parameters (mainly the geometrical parameters like shell inner and outer radius, density power law), while other parameters were kept fixed or were changed only marginally (radius and  $\log(g)$  of the central star, composition and mass ratio Carbon:Silicates for the dust).

Here we give some remarks:

1.) The grain size distribution has to be chosen in a way that larger grains ( $\geq 0.25 \mu\text{m}$ ) are included and not too much very small grains ( $\leq 0.02 \mu\text{m}$ ). Otherwise, we could not even approximately reproduce the strong depth and the non-Gaussian shape of the Silicate feature at 10 micron. This is of course consistent with the conclusions we made in Sect. 4.1.3. There, the best fit to the N band spectrum alone was obtained with dust obeying an  $R_V = 5.5$  extinction law, a clearly higher value than the  $R_V = 3.1$  found in the interstellar medium. Remember that  $R_V \equiv A_V/(A_B - A_V)$  would tend toward infinity when very large grains are considered that produce grey extinction ( $A_\lambda \neq f(\lambda)$ ), while very small grains that do Rayleigh scattering ( $A_\lambda \propto \lambda^{-4}$ ) would produce very steep extinction with  $R_V \approx 0.65$ . Thus, higher  $R_V$  values are consistent with larger grains as long as we stay in the regime of compact dust particles and do not consider fractal or porous grains.



**Table 4.6:** Parameters for the radiative transfer model shown in Fig. 4.14

Parameter		Unit	Value
Effective star temperature	$T_{\text{eff}}$	K	25000
Star radius	$R_*$	$R_{\odot}$	7.5
Star surface gravity	$\lg(g)$	–	3.0
Star intrinsic luminosity	$L_*$	$L_{\odot}$	20000
Dust shell inner radius	$R_i$	$R_*$	35000
Dust shell outer radius	$R_o$	$R_*$	60000
Radial density powerlaw exponent	$\lg(d\rho / dr)$	–	–1.0
Mass ratio Silicates:Carbon <sup>a</sup>	$M_{\text{Silicates}}/M_{\text{Carbon}}$	–	9 : 1
Smallest grain radius	$a_s$	$\mu\text{m}$	0.01
Largest grain radius	$a_l$	$\mu\text{m}$	2.0
Grain size distribution exponent	$\lg(dN / da)$	–	–3.5
Total envelope mass (gas + dust) <sup>a</sup>	$M_{\text{tot}}$	$M_{\odot}$	3.0

<sup>a</sup> Like in Sect. 3.6, we used a mixture of silicates (Dorschner et al. 1995) and carbonaceous materials (Preibisch et al. 1993) as grain material.

<sup>b</sup> Assuming a canonical dust : gas mass ratio of 1 : 100.

2.) 1D models have as a common feature a steep rise in the SED in the wavelength range 3 – 20  $\mu\text{m}$  (see also Fig. 4.14). It is very difficult to reach a relatively flat slope between 3.8  $\mu\text{m}$  and 18.75  $\mu\text{m}$  like the one indicated by our observations, if at the same time the deep Silicate feature is to be fitted. Furthermore, also the relatively high 1.4-mm flux poses a problem for the modelling. We are not able to fit all three main features of the observed SED simultaneously with one and the same model. Here, we certainly reach the limits of a simple 1D modelling. In Fig. 4.14 we show a model where the N band spectrum is quite well reproduced, but the 3 – 5  $\mu\text{m}$  and 1.4 mm fluxes are not matched. We give the parameters we used for this particular model in Table 4.6.

3.) The presence of (additional) axi-symmetric dust configurations around the central star (e.g., a circumstellar disk or, more general, flattened 2D structures) can be one way to explain the excess emission at 3 – 5  $\mu\text{m}$ , since such a geometry would enable an excess heating of the inner disk surface by the central hot star. On the other hand, such a disk would also block a fraction of the star light that normally would directly reach the spherical dust shells of the envelope. Hence, these shells are less heated in these directions of the disk extension. If the observer sees the disk-envelope system edge-on, (s)he would therefore see a colder envelope and the SED peak would have been shifted towards longer wavelengths in better agreement with the IRAS points (see again Fig. 4.14). Furthermore, if a considerable fraction of the total mass is concentrated within the flattened structure, the resulting high optical depth along the disk plane would be conducive to a high millimetre flux.

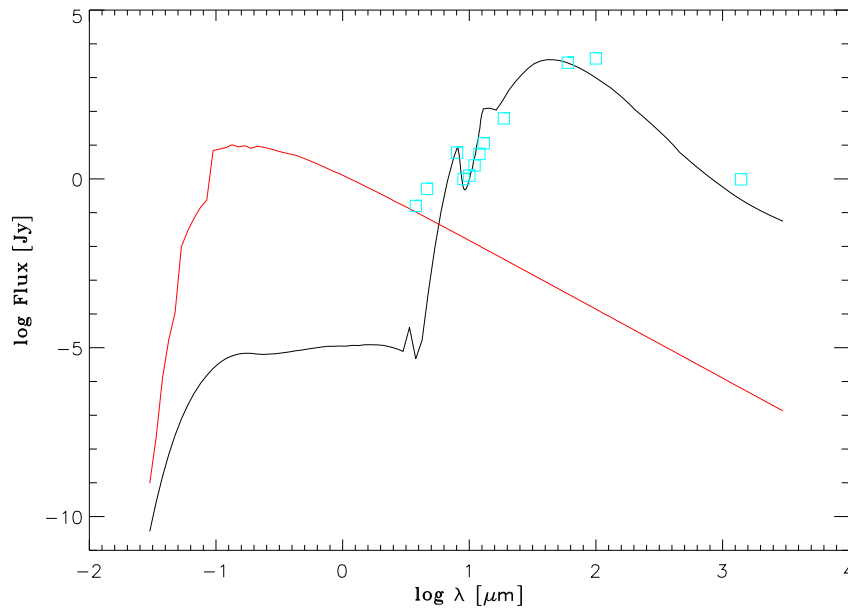


**Figure 4.14:** SED prediction of one of our simple dust shell models. The black line shows the resulting flux densities, the red line gives the intrinsic SED of the central star used in this model. The turquoise squares denote measures fluxes of GGD 27–ILL: our L', nb\_M, and Q2 band fluxes, our N-band spectrum, the 60  $\mu\text{m}$  and 100  $\mu\text{m}$  IRAS points, and the 1.4-mm BIMA measurement of Gómez et al. (2003).

4.) The total envelope mass in the model of  $3.0 M_{\odot}$  appears relatively low at first glance. However, we pass on two results derived by Gómez et al. (2003). Based on their BIMA 3.4 mm and 1.4 mm continuum data toward GGD 27–ILL they derive a total mass of  $1.8 - 3.7 M_{\odot}$  from the dust emission. Furthermore, they have detected SO ( $5_5-4_4$ ) emission associated with the central source. The data allow for a kinetic temperature of 50 – 100 Kelvin for the SO gas, and the derived total mass is  $0.7 - 3.5 M_{\odot}$ . Thus, our adopted mass of  $3.0 M_{\odot}$  is in good agreement with these findings.

### What's inside?

Concluding remarks about the luminosity of GGD 27–ILL and consequently about the intrinsic nature of the contained power source are difficult to make. Here, a comprehensive 2D modelling of the source will lead to real insights and will be a more accurate way of delimiting the real luminosity.

We learned so far that the 1D models give a poor description of the (combined) details of the SED and the N–band spectrum of GGD 27–ILL. From the spectrum we find that the circumstellar extinction along the line–of–sight toward us is very high, and the main object GGD 27–ILL remains invisible in the near–infrared, even in our VLT K narrow–band images. Nevertheless, this source is known to illuminate much of the material that lies almost perpendicular to our line–of–sight and thus gives rise to the immaculate near–infrared reflection nebula (Aspin et al. 1991, Tamura et al. 1991, our Fig. 4.1) and to the presence of scattered CO 2.3  $\mu\text{m}$  bandhead emission towards these directions (Aspin 1994). Hence, a profound asymmetry in the distribution of extinguishing material around GGD 27–ILL must

exist. Simply integrating the measured fluxes and assuming spherically symmetric emission ( $4\pi$ ) will lead to a severe underestimation of the real luminosity.

When we, nevertheless, attempt to give at least an order-of-magnitude estimate of the total luminosity, two main hurdles have to be taken.

- First, we have to correct the measured IR fluxes for the found extinction which, as we assume, mainly acts within our line of sight. Since the Weingartner & Draine (2001) case B dust model with  $R_V = 5.5$  gives the best fit to our N-band spectrum (Sect. 4.1.3), we use the extinction relations predicted by this model (see Fig. 4.7 for a visualisation). The correction is applied to the measured fluxes of GGD 27–ILL reported in Table 4.1 starting with our fit value for  $\tau_{9.7\mu\text{m}}$  of 7.45 (and  $A_{9.7\mu\text{m}} = 1.086 \times \tau_{9.7\mu\text{m}}$ ). The derived extinction magnitudes are added to Table 4.1.
- The extinction is negligible at (sub)millimetre wavelengths, the dust emission is assumed to be optically thin. However, here the general problem of observations with low spatial resolution comes to surface again. While we have a few interferometric data points at 1.4 mm (Gómez et al. 2003) and 2.6 mm (Yamashita et al. 1991, Gibb et al. 2004a) with sufficient resolution to trace GGD 27–ILL, the situation is worse for the submillimetre range. Here only single-dish measurements with beam sizes  $11'' - 15''$  can be used that probably comprise the flux from all three millimetre clumps found by Yamashita et al. (1991). Unfortunately, also the SMA  $850\ \mu\text{m}$  observations by Su et al. (2004b) cannot be used since these were early measurements with a small number of antennas, and the data severely suffer from loss of coherent flux due to the poor uv-coverage (Beuther 2005). Indeed, the flux for GGD 27–ILL in the  $850\ \mu\text{m}$  SMA map shown in our Fig. 4.10 is the same as for the BIMA 1.4 mm observations by Gómez et al. (2003) although the spectral index should be steeply rising for optically thin dust emission. A special problem in the case of GGD 27 seems to be that there is not really an agreement about the proper submillimetre fluxes of this object (see Table 4.7). This is even more surprising since all the measurements listed in this Table – with the exception of the  $350\ \mu\text{m}$  point of Hunter et al. (2000) – have been made with the same instrument (UKT14) at the same telescope (JCMT). Yamashita et al. (1990) give as total flux only the signal in a limited area not much larger than the HPBW of the instrument. We will not consider their results further. The reason for the low flux given by Vallée & Bastian (2000) remains unclear. We proceed in two ways:
  1. ) First, we take the BIMA interferometric 1.4-mm flux of 0.97 Jy as reported by Gómez et al. (2003) for GGD 27–ILL and extrapolate this flux to 1.2 mm wavelength, using the dust emission spectral index given by the same authors ( $F_{(\text{sub})\text{mm}} \propto \lambda^{-2.6}$ ). Now we find the flux ratio of our 1.2-mm SIMBA observations of our millimetre clump MM1 (which contains GGD 27–ILL) to this extrapolated flux to be  $(6.17\ \text{Jy} / 1.45\ \text{Jy}) = 4.3$ . We use the factor  $4.3^{-1}$  to correct the single dish fluxes of McCutcheon et al. (1995) for 1.1 mm and  $800\ \mu\text{m}$ , of Aspin et al. (1994) for  $450\ \mu\text{m}$ , and of Hunter et al. (2000) for  $350\ \mu\text{m}$ .

- 2.) Second, we again start with the BIMA interferometric 1.4-mm flux for GGD 27–ILL (Gómez et al. 2003) and directly extrapolate this value up to  $350 \mu\text{m}$ . However, we mention, that the dust spectral index is not well constrained by the available interferometric millimetre observations and might range from  $-2.6$  to  $-4.0$ .

The results of both approaches are also given in Table 4.7.

We integrate the resulting approximated SEDs and report here the corresponding luminosities, assuming a distance of 2.0 kpc:

- |   |                           |
|---|---------------------------|
| 1.) no IR extinction correction,<br>sub–mm fluxes reduced according to Table 4.7                                  | 9197 – 9342 $L_{\odot}$   |
| 2.) no IR extinction correction,<br>entire single–dish sub–mm fluxes (bold face in Table 4.7)                     | 33913 $L_{\odot}$         |
| 3.) IR extinction correction according to Table 4.1,<br>sub–mm fluxes reduced according to Table 4.7              | 47528 – 47673 $L_{\odot}$ |
| 4.) IR extinction correction according to Table 4.1,<br>entire single–dish sub–mm fluxes (bold face in Table 4.7) | 72244 $L_{\odot}$         |

As expected, changes in the high–frequency part of the SED (i.e., in the infrared) due to the extinction correction are much more important than the details of the flux estimation in the (sub)millimetre range.

To translate these total luminosities into (single star) spectral types, we consult the relevant publications that give up–to–date calibrations of stellar parameters for high–mass stars (e.g., Martins et al. 2005). It is evident that the luminosity given at number 4.) is the upper limit for the real luminosity of the central object GGD 27–ILL. The value of  $72244 L_{\odot}$  corresponds to a spectral type of O8.5 in case of a ZAMS star of luminosity class V. The lower luminosity limit is indicated under number 1.), such luminosities correspond to a B1 – B1.5 ZAMS star. We evaluate the situation given under number 3.) as the most likely one. Such luminosities around  $47600 L_{\odot}$  are inherent to ZAMS dwarf stars with spectral type B0 – O9.5. Such stars have a (spectroscopic) mass of  $15 - 17 M_{\odot}$ , thus clearly above the critical limit of  $8 - 10 M_{\odot}$ , where the time scales for accretion and stellar contraction are reversed (see Sect. 1.1.1).

Again, we mention that these considerations give just an order–of–magnitude estimation of the real luminosity. Some properties of young massive stars have not been taken into account, that would be far beyond the scope for this section. We just briefly remind on the fact that massive stars are known to be fast rotators. Hence, the so–called von Zeipel effect (von Zeipel 1924, Maeder 1999) that describes the dependence of the local effective temperature on the local surface gravity of a rotating star, leads to a considerable difference in  $T_{\text{eff}}$  between the poles and the equator of such a star. More than 4000 K difference have been estimated in the case of classical Be stars (e.g., Frémat et al. 2005). For GGD 27–ILL we expect that its rotational axis is roughly aligned with the radio jet axis, hence with only a small inclination to the plane of the sky (Martí et al. 1993). Thus, we probably “see” only the emission from the equatorial (i.e., cooler) regions of the central object, and even more emission is intrinsically radiated on the poles in the directions perpendicular to our line–of–sight.

**Table 4.7:** Overview of the diversity of reported sub–millimetre fluxes (given in Jy) for GGD 27

Reference	F(1100 $\mu\text{m}$ )	F(800 $\mu\text{m}$ )	F(760 $\mu\text{m}$ )	F(450 $\mu\text{m}$ )	F(350 $\mu\text{m}$ )
Aspin et al. (1994)	–	–	–	<b>150.0</b>	–
Hunter et al. (2000)	–	–	–	–	<b>320.0</b>
McCutcheon et al. (1995)	<b>7.50</b>	<b>74.3</b>	–	92.9	–
Vallée & Bastian (2000)	–	–	10.0	–	–
Yamashita et al. (1990)	3.20	7.2	–	45.0	95.0
correction factor $(4.3)^{-1}$ applied <sup>(a)</sup>	1.74	17.3	–	34.9	74.4
extrapolation with dust SI= $-2.6$	1.82	4.2	4.7	18.6	35.7
extrapolation with dust SI= $-4.0$	2.55	9.1	11.2	90.9	248.3

<sup>(a)</sup> The correction factor is applied to the flux values marked in **bold face** in the upper rows.

#### 4.4.2 A complex environment

Our *SIMBA* mapping shows that also the further environment of GGD 27 is populated with several dense clumps of material. The clump MM4 is located perpendicular to the radio jet axis and a direct relation to this jet and to the associated molecular outflow is not obvious.

The situation is different for MM2 and MM3, since the related gas clumps have been known to lie near to Herbig–Haro objects and knots within the radio jet. For instance, Molinari et al. (2001) propose, based on their FIR spectroscopy of HH 80/81, a simple model. The far–ultraviolet radiation arising from the ionised material in the recombination regions of the jet and the Herbig–Haro objects induce the formation of a photon–dominating region (PDR) in the surrounding medium. Are the  $\text{NH}_3$  clumps associated with MM2 and MM3 just irradiated regions where the ammonia emission can therefore be strongly enhanced while the material is not particularly dense? In this case, the assumption of a standard  $\text{NH}_3$ –to– $\text{H}_2$  ratio would mimick a much higher total mass than is actually present in the clumps.

We have for the first time detected 1.2-mm continuum emission for MM2 and MM3, that is obviously caused by cold dust (since both clumps are not a source of centimetre radio emission that would indicate a contribution from free–free or Synchrotron emission). We mention a region of several tens of arcseconds in diameter, centred on both clumps, respectively, that are completely devoid of optically visible and 2MASS stars. This suggests the presence of strongly extinguishing dense material in these clumps. We do not find MSX emission sources there (cf. Fig. 4.13), not even in the longest wavelength band (21.3  $\mu\text{m}$ ). On the other hand, the MSX images of these regions do not show indications for the presence of typical infrared dark clouds (Egan et al. 1998). This is of course simple to explain, since in order to recognise an IRDC one has to rely on the presence of a strong and diffuse mid–infrared emission background (probably caused by PAHs), where the IRDCs are seen as dark silhouettes. This diffuse MIR background is mainly concentrated towards the midplane of the Galactic disk and dilutes more and more toward larger Galactic latitudes. GGD 27 is located at a Galactic latitude of  $b = -2.59^\circ$  where this dilution effect is clearly at work. Furthermore, the PAH material has to be excited by energetic UV radiation, preferentially due to O stars in the near

vicinity. Although several well-known bright infrared sources exist in the GGD 27 complex, probably none of them has the energy characteristics of an O star.

Although covered by the *Chandra* X-ray observations of Pravdo, Tsuboi & Maeda (2004), no X-ray emission has been reported toward the NH<sub>3</sub> clumps of Girart et al. (1994) and Gómez et al. (2003) that are detected in our 1.2-mm maps. This does not exclude that X-ray emission might be present intrinsically<sup>10</sup>, but probably the related column densities are high enough to strongly attenuate weak X-ray fluxes below the detection limits of *Chandra*. Gómez et al. (2003), for instance, report  $N(\text{H}_2) = 4.9 \times 10^{23} \text{cm}^{-2}$  for their ammonia core associated with MM2.

Still, from the continuum measurements alone we cannot tell whether these clumps are quiescent clumps or whether indeed star formation in a very early stage is going on. To answer this further molecular line observations are necessary. The previous NH<sub>3</sub> measurements just reveal narrow line widths ( $\sim 1$  km/s) indicative of low levels of turbulence. However, Girart et al. (2001) report indications for outflow activity toward MM3 based on HCO<sup>+</sup> follow-up observations which support the idea that star formation has begun in MM3. For MM2, the situation is not yet explored further. In case the clumps are able to form stars, the mass reservoirs of  $\leq 14 - 67 M_{\odot}$ , respectively, are sufficient to form low- or intermediate-mass stars. Taking into account that the given masses are upper limits and considering the fact that not all of the initial mass is finally collected into stars during star formation, it is not sure whether at least the clump MM2 can give rise to another high-mass star in the GGD 27 region.

## 4.5 Conclusions

Based on an extensive infrared observing campaign and additional millimetre observations toward the central source of the massive star-forming region GGD 27, we analysed the energetics and morphology of this object in detail. We give here our conclusions.

1.) For the first time, the central object GGD 27-ILL could be detected at a wavelength as short as 3.8 micrometre. A spatial resolution better than 0.5 arcseconds could be achieved. Its brightness increases strongly when going to longer wavelengths, and this object turns out to be dominating in the mid-infrared. However, GGD 27-ILL is not detected at 2.15  $\mu\text{m}$  but remains hidden behind a high column density of dust which is caused by circumstellar extinction and by a medium-scale dusty lane that is cutting through the centre region of GGD 27.

2.) Our near- and thermal infrared imaging from 2.15  $\mu\text{m}$  to 4.66  $\mu\text{m}$  demonstrate that a small-scale structure associated with GGD 27-ILL (linear extension  $\leq 1000$  AU) exists roughly oriented along the axis of the radio jet. The structure morphology changes dras-

<sup>10</sup>However, the reported line widths of  $\sim 1$  km/s of the ammonia measurements do not indicate perturbations by fast shocks that could cause the X-ray emission.

tically over this wavelength range. This finding is supported by the results of an image deconvolution that has been applied to the near- and thermal infrared *ISAAC* images. We mention the possibility that a second faint IR source might exist in a few hundred AU projected distance to the main object GGD 27-ILL. Such a source could perhaps partly explain the long-periodic wiggling ( $\sim 5300$  years) that has been found in the well-collimated radio jet (Martí et al. 1993). However, also wavelength-dependent optical depth effects are probably important for the interpretation of the L' band structure.

3.) We prove that asymmetries in the extinguishing circumstellar material around GGD 27-ILL must exist. Also for this object, selfconsistent radiative transfer models based on a spherically symmetric geometry cannot explain all the observational results within one coherent model. A flattened axisymmetric distribution of the circumstellar material is the trend indicated by the models. We probably see along a line-of-sight that features a high column density of dust, thus we might see the equatorial region of the flattened structure. The spectral type of the central star is probably between O9.5 and B0.5.

4.) The shape and depth of the N-band spectrum toward GGD 27-ILL and the successful fit of the  $R_V = 5.5$  case B dust model of Weingartner & Draine (2001) to these data confirm the high extinction due to circumstellar material and indicate the presence of a considerable fraction of larger dust grains ( $a \geq 0.25\mu\text{m}$ ) in the circumstellar environment around GGD 27-ILL.

5.) For the first time, we could demonstrate the viability of the cross-calibration method with 44-GHz Methanol masers for VLA 7-mm continuum observations. The target, GGD 27-ILL, is not directly resolved even with a spatial resolution as low as 0.1 arcseconds. However, there are indications for an intrinsic structure for the radio emission that is noticeably inclined with respect to the orientation of the radio jet. While free-free emission appears to dominate, there is certainly a contribution from dust emission to the total 7-mm signal. However, its fraction can not be determined with certainty on the basis of our data.

6.) The 1.2-mm mapping with *SIMBA* revealed the presence of several dust cores in the farther vicinity of GGD 27-ILL with total masses smaller than  $100 M_\odot$  each. All these cores can be related to known molecular clumps.

7.) Within our *ISAAC* field-of-view, we could associate all X-ray sources reported by Pravdo, Tsuboi & Maeda (2004) with near-infrared sources. This is similar to other X-ray investigations of massive star-forming regions (e.g., Feigelson et al. 2002, Hofner et al. 2002). In contrast to the case of the W3 observations of Hofner et al. (2002) where several O stars with their UCHII regions are in the field of view of *Chandra* that have shown X-ray counterparts, no O stars (perhaps with the exception of GGD 27-ILL itself) are known in GGD 27. Nevertheless, all 11 X-ray sources in the central region of GGD 27 detected

by Pravdo, Tsuboi & Maeda (2004) can probably be related to compact NIR sources found in our *ISAAC* imaging that are of lower luminosity than the central object. For the X-ray source near to the central object our imaging data reveal the presence of two strongly reddened sources in an area of high extinction. In principle, this finding supports the interpretation that the central X-ray emission is arising from a PMS star of lower luminosity (a few hundred  $L_{\odot}$  at maximum). Since we found two nearby sources at the X-ray position, also a case of interacting winds from two of such PMS stars seems possible. However, due to the astrometrical uncertainty of the *Chandra* data for this region, an association of this X-ray source with the nearby radio jet source should not be rashly excluded from further discussions.



## **Chapter 5**

# **Sources for VLA-7mm observations**

The two sources analysed in the previous chapters (G9.62+0.19–F and GGD 27–ILL) are contained in a sample of HMPO candidates for which a larger effort is ongoing to observe these sources with the VLA at 7 mm. The sample comprises sources mainly from two subgroups. Eight sources are taken from the list of established hot molecular cores (see also Sect. 1.1.2) as given by Kurtz et al. (2000). Almost all of these HMCs have strong UCH<sub>II</sub> regions nearby. In contrast, six sources are taken from the HMPO candidate list of Molinari et al. (1996) and feature none or only very weak centimetre free–free emission for the entire star–forming region. For all of the sources in Table 5.1, the presence of 44–GHz Methanol masers has been shown recently by Kurtz, Hofner & Vargas Álvarez (2004). Thus, they are potential sources for the application of the maser cross–calibration as described in Sect. 2.3 and Appendix D. (Although the strength of the masers and therefore the applicability of the cross–calibration technique under non–optimal observing conditions varies from source to source.)

Since a main concern of this thesis are questions about the infrared appearance of massive star–forming regions containing HMPOs we elaborate in the following what can be said in this regard for the sample members given in Table 5.1.

## **5.1 Infrared colour criteria**

Traditionally, the IRAS Point Source Catalogue served as a kind of lighthouse that guided the astronomer to identify UCH<sub>II</sub> regions (e.g., Wood & Churchwell 1989a, 1989b) or even indicated UCH<sub>II</sub> precursor candidates (e.g., Henning 1990, Palla et al. 1991, Chan et al. 1996, Molinari et al. 1996, Sridharan et al. 2002), all based on IRAS colour criteria and IRAS flux delimiters. However, the spatial resolution of IRAS is very poor (> 1 arcmin). We mentioned the observer’s dilemma already in our introduction (Sect. 1.1.1). During the previous 10 years the situation improved with the introduction of new large–scale (or even all–sky) surveys in the mid–infrared (MSX) and in the near–infrared (2MASS, DENIS).

Lumsden et al. (2002) included MSX and 2MASS data and proposed colour criteria for

**Table 5.1:** Sources of our VLA 7-mm continuum survey

Region	RA(J2000)	DEC(J2000)	HMPO	Reference
G9.62+0.19	18 06 14.88	-20 31 39.4	HMC	(2), (7), (8), (13)
G10.47+0.03	18 08 38.20	-19 51 50.2	HMC	(2), (3)
G12.21-0.10	18 12 39.65	-18 24 18.1	HMC	(9)
Mol 45	18 17 23.60	-17 22 10.0	Molinari low	(12)
Mol 50	18 19 07.50	-16 11 21.0	Molinari low	(12)
GGD 27-ILL	18 19 12.10	-20 47 31.0	mYSO	(6)
G19.61-0.23	18 27 38.05	-11 56 37.0	HMC	(4),
G29.96-0.02	18 46 03.80	-02 39 15.0	HMC	(2), (3)
G31.41+0.31	18 47 35.00	-01 12 45.0	HMC	(2), (3)
G34.15-0.26	18 53 18.40	+01 14 55.0	HMC	(5),
Mol 98	19 11 37.40	+08 46 30.0	Molinari low	(12)
W51 e2/e8	19 23 43.20	+14 30 33.0	HMC	(14)
Mol 116	20 08 30.00	+35 40 23.0	Molinari high	(12)
Mol 117	20 11 46.40	+36 49 37.0	Molinari low	(12)
DR21(OH) MM1	20 39 00.90	+42 22 47.0	HMC	(10), (11)
Mol 138	21 40 42.40	+58 16 10.0	Molinari high	(1), (12)

References: (1) Beltran et al. (2004), (2) Cesaroni et al. (1994), (3) Cesaroni et al. (1998), (4) Garay et al. (1998), (5) Gómez et al. (2000), (6) Gómez et al. (2003), (7) Hofner et al. (1994), (8) Hofner et al. (1996), (9) Hofner & Churchwell (1996), (10) Mangum et al. (1991), (11) Mangum et al. (1992), (12) Molinari et al. (1996), (13) Testi et al. (2000), (14) Zhang et al. (1998)

these catalogues in order to identify massive YSOs in a precursor stage to an UCH<sub>II</sub> region. Remember that MSX provides data at 8.3  $\mu\text{m}$  (Band A), 12.1  $\mu\text{m}$  (Band C), 14.7  $\mu\text{m}$  (Band D), and 21.3  $\mu\text{m}$  (Band E). The 2MASS catalogue gives fluxes of sources in the classical NIR broad bands J (1.24  $\mu\text{m}$ ), H (1.65  $\mu\text{m}$ ), and K<sub>s</sub> (2.16  $\mu\text{m}$ ). According to Lumsden et al. (2002), UCH<sub>II</sub> precursor candidates should obey the following criteria:

- $F_E > F_D > F_A$ ,
- $F_E / F_A > 2$ ,
- $F_A / F_K > 5$ ,
- $F_K / F_J > 2$ .

We have consulted the MSX and 2MASS catalogues for our sample of VLA 7-mm sources as given in Table 5.1. We learn that almost all of our regions unambiguously follow these rules (at least for the first two criteria exclusively dealing with MSX fluxes). Furthermore, for most of the HMCs in our sample, MSX images have already been collected (Crowther &

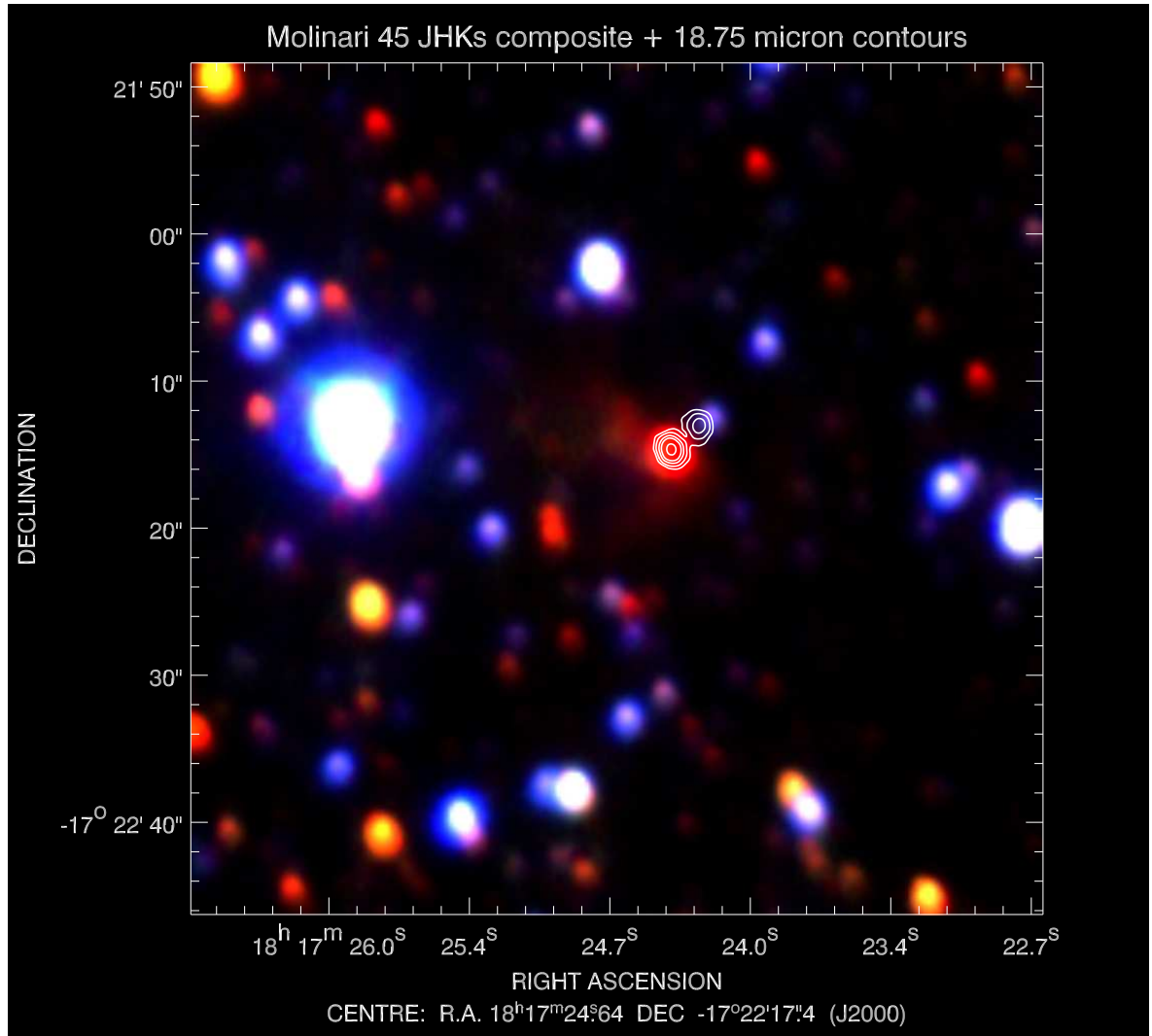


**Figure 5.1:** JHKs colour composite of the centre of the Molinari 45 region with overlaid contours from our *TIMM12* Q2 band imaging.

Conti 2003) that confirm the red MSX colours for this subsample.

The situation is not always straightforward in the near-infrared. The vast majority of the HMCs have adjacent UCH<sub>II</sub> regions within a few arcseconds distance. Depending on the geometrical circumstances and the age of such an UCH<sub>II</sub> region, it can be visible in the near-infrared as a red 2MASS source. This is the case for instance for G19.61–0.23 and G29.96–0.02.

A different case are sources like G9.62+0.19, GGD 27–ILL, Mol45, Mol 116, Mol 117, and Mol 138, where red NIR sources near to the HMPO candidates do not arise from an UCH<sub>II</sub> region, but from neighbouring sources that are for instance illuminated blobs showing mainly scattered light (like GGD 27 IRS2) or just sources featuring a lower luminosity (like G9.62+0.19–F1). Some of the red 2MASS sources might even turn out to be emission line objects (B<sub>ry</sub> or H<sub>2</sub> emission), caused by the interaction of energetic outflows and jets from the embedded massive objects with their environment.

Thus, the Lumsden criteria might work in most of the cases, but they work based on the

fortunate circumstances that the actual UCH<sub>II</sub> precursors (which often do not show up in the near-infrared at all) are mostly accompanied by nearby sources that are less affected by extinction, and have perhaps a different SED. These neighbouring sources leave then the right trace in the 2MASS catalogue.

We will and can not extend this chapter in order to give an in-depth treatment of all the sources of our VLA 7-mm mapping campaign (Table 5.1). A thoroughful data reduction of the VLA 7-mm data is currently ongoing, and final results will be published in a future paper (Hofner, Araya, Linz, et al., in preparation). However, we briefly introduce the source Molinari 45. This source is part of our VLA 7-mm sample, but its classification differs from G9.62+0.19–F (HMC) as well as from GGD 27–ILL (mYSO) since it is taken from the sample of UCH<sub>II</sub> precursor candidates by Molinari et al. (1996). However, we demonstrate with help of a few observational IR and millimetre results we have obtained already that this source fits in the main trend we have worked out for G9.62+0.19 and GGD 27–ILL in the previous two chapters: the thermal infrared data are the discriminator that can distinguish between the actual sources of interest (UCH<sub>II</sub> precursors or HMPOs) and sources (sometimes of lower luminosity, sometimes already UCH<sub>II</sub> regions) that “accompany” them.

## 5.2 Molinari 45 – An exemplary case?

The region Molinari 45 (in the following Mol 45) is associated with IRAS 18144–1723. This source was included in the Palla sample<sup>1</sup> of candidate regions for massive star formation (Palla et al. 1991). The region was classified as a “low” source based on its IRAS colours (i.e.,  $\lg(F_{25} / F_{12}) < 0.57$ ), although one has to keep in mind that the IRAS 12- $\mu$ m flux of Mol 45 was an upper limit<sup>2</sup>.

The group of Molinari and collaborators used the Palla sample for further radio studies (Molinari et al. 1996, 1998, 2000). First, observations with the Effelsberg 100-m telescope (HPBW  $\approx 40''$ ) proved Mol 45 to be a strong emitter in the NH<sub>3</sub> (1,1) and (2,2) transitions (Molinari et al. 1996). While the kinetic temperature derived from these single-dish measurements is rather low (23.6 K) when compared to other sources in the sample, Mol 45 shows the highest NH<sub>3</sub> column density among all Molinari sources ( $2.60 \times 10^{15} \text{ cm}^{-2}$ ). Furthermore, from the ammonia spectra, a kinematic distance of 4.33 kpc was derived.

While single-dish (sub)millimeter observations with SCUBA at 450  $\mu$ m, 850  $\mu$ m, and 1100  $\mu$ m revealed a strong source near the IRAS coordinates (Molinari et al. 2000), VLA observations at 2 cm and 6 cm could not discover centimeter emission above the 3-sigma limit from the region around Mol 45 (Molinari et al. 1998). Regarding molecular line observations for Mol 45, only single-dish observations of NH<sub>3</sub> (Molinari et al. 1996) and CO (Jaffe et al. 1982, Molinari 2004) seem to exist beside the new VLA methanol observations of Kurtz,

<sup>1</sup>The discriminator for this sample was a 60- $\mu$ m flux  $> 100 \text{ Jy}$ .

<sup>2</sup>This is a fact that excluded this source from the catalogue of massive YSOs compiled by Chan et al. (1996).

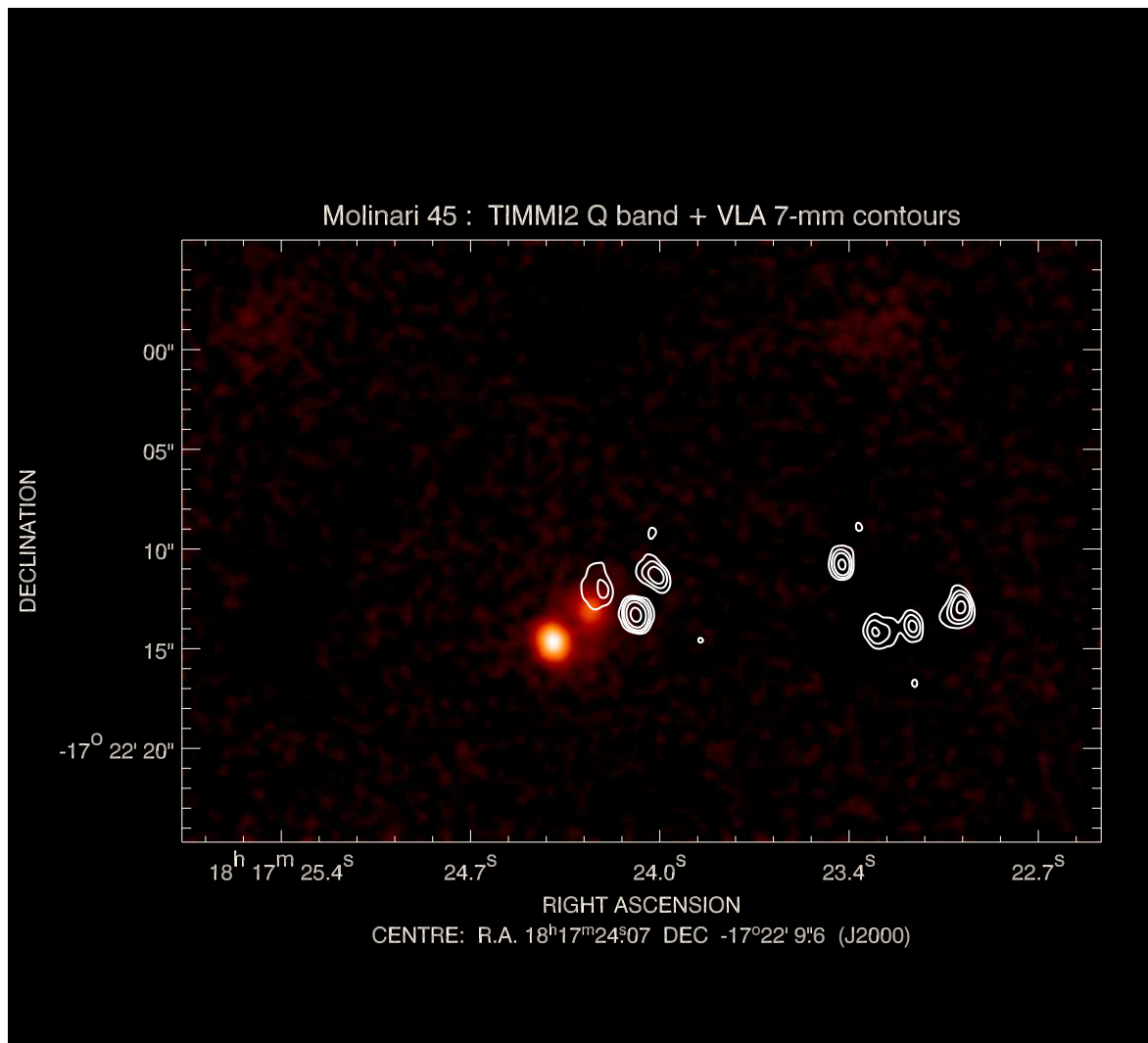


**Figure 5.2:** The centre of the Molinari 45 region exhibits two sources at  $18.75 \mu\text{m}$ . Superimposed are the contours of 44 GHz methanol masers found by Kurtz, Hofner & Vargas Álvarez (2004). Note that some of the methanol emission spots probably contain a certain fraction of thermal line emission.

Hofner & Vargas Álvarez (2004). There are no clear-cut indications for a molecular outflow (Molinari 2004).

We summarise in the following our findings based on IR and millimetre data:

- NIR data for Mol 45 have been retrieved from the ESO data archive. The related observations had been conducted in August 2000 within the observing programme ID 65.I-0310 (PI: S. Molinari). These are data from the infrared imager *SofI* (“Son of ISAAC”) mounted at the New Technology Telescope (*NTT*) in La Silla, Chile in the NIR broad bands J, H, and  $K_s$ , apparently taken under mediocre seeing conditions. A colour composite of these data is shown in Fig. 5.1. In the centre of the region a strongly reddened source is visible that is surrounded by extended  $K_s$  band emission mainly to the east of it. Within a diameter of roughly 10 arcseconds around that central source, only two faint bluish stars are visible.

- Our M band imaging at  $4.7\ \mu\text{m}$  with *TIMMI2* shows just the central red source, the rich field of stars still seen in the NIR has dimmed. However, a very weak extension to the northwest of the central source is visible.
- Our *TIMMI2* N4 band data at  $11.7\ \mu\text{m}$  confirm the presence of a second mid-infrared source, ca. 2.5 arcseconds to the northwest of the main source. It is still much fainter than the main source.
- At  $18.75\ \mu\text{m}$ , the brightness difference of the two MIR sources has further decreased (Fig. 5.2). Taking all the *TIMMI2* results together, we see that the SED of this second source is much more steeply rising than the SED of the main source that was already visible in the  $K_s$  band.
- A cluster of 44 GHz Methanol masers exists in the vicinity of the MIR sources (Fig. 5.2). It is noticeable that a subgroup of these masers is relatively near to the second MIR source.
- With our large-scale 1.2-mm mapping using *SIMBA* we trace the compact dust emission of the Mol 45 centre region. Furthermore, we reveal the presence of several additional millimetre cores in the farther vicinity that coincide with MSX infrared dark clouds (Fig. 5.3) and might harbour cold massive cloud cores at the verge of forming the next generation of massive stars. Further molecular line data are necessary to support this claim.

We learn from this example that many of our sample members might provide a surprise when near-infrared data from regions containing HMPOs are finally compared to data at longer wavelengths and to *VLA* data. But also here, the thermal infrared observations prove their virtue.

From all things mentioned above we can summarise that this sample of objects is certainly worthwhile regarding *VLA* 7-mm continuum observations. With GGD 27-ILL we have presented a quite complicated case for interpreting *VLA* 7-mm observations. In particular, the Molinari subsample promises some relief in this regard since no strong free-free emission caused by  $\text{UCHII}$  regions or thermal radio jets is reported at least for the Molinari “low” sources that would complicate the observations as well as the estimations of dust emission contributions.

The sample is also interesting for *VLA* 7-mm observations since it traces a different subclass of HMPOs than the recent series of *VLA* 7-mm papers by Menten and van der Tak (2004) and van der Tak & Menten (2005) that are aiming toward BN-type objects (e.g., Henning 1990). Most of these well-known objects are near-infrared bright per se, and it will be interesting to work out the differences between the several HMPO subclasses.

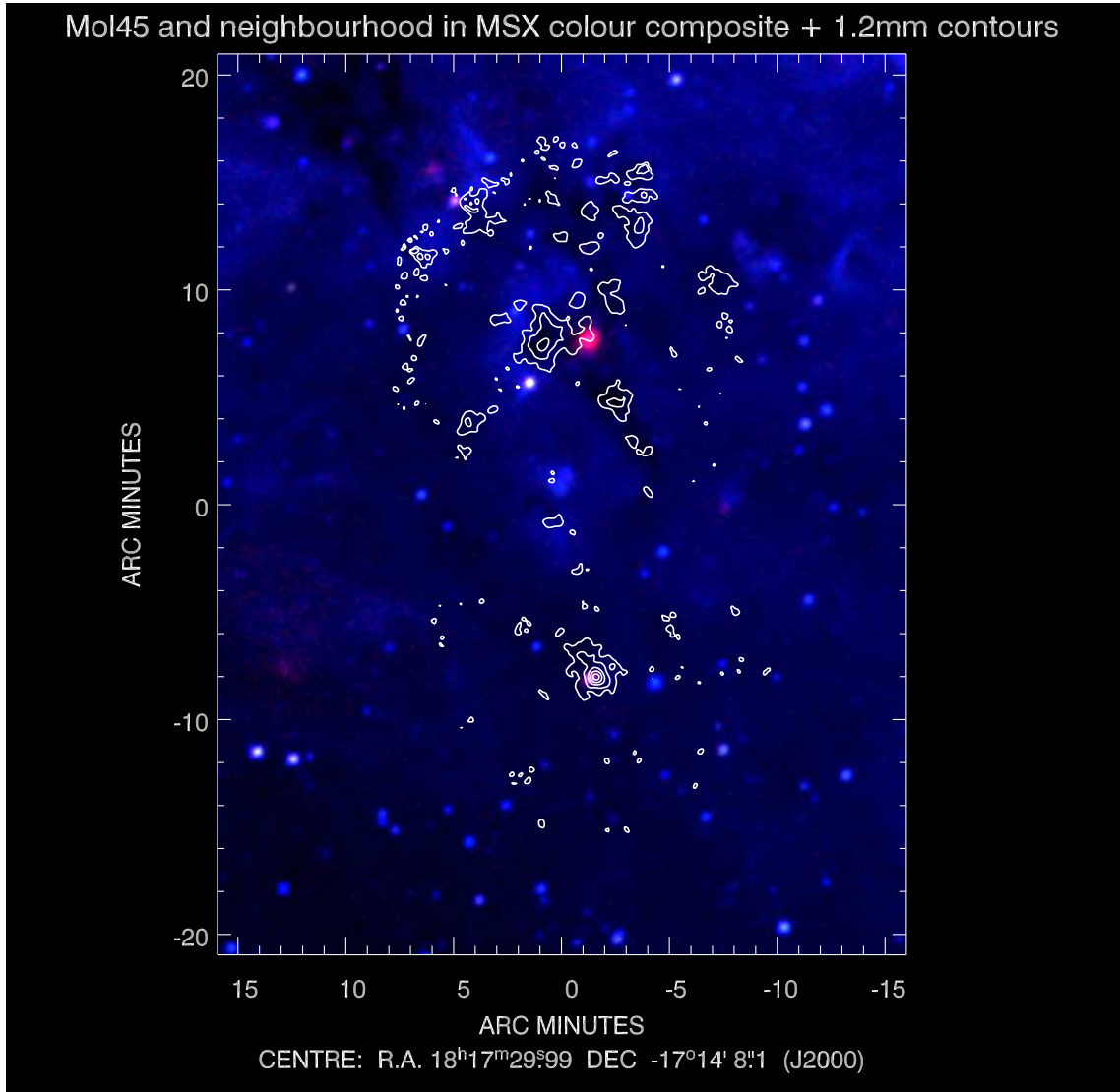


**Figure 5.3:** The usual MSX colour composite with  $8.3 \mu\text{m}$  (blue),  $12 - 14 \mu\text{m}$  (green) and  $21.3 \mu\text{m}$  (red) images combined in the same way as in the Figs. 3.2 and 4.13. Our *SIMBA* 1.2-mm observations cover a particularly large area in this case. Strong mm emission is detected for the Mol 45 centre region which is the strong millimetre source to the south at the offset coordinates  $(-2, -8)$ . The farther northern neighbourhood of the Molinari 45 is populated with several spectacular IRDCs that are also well traced by the millimetre mapping.

## **Chapter 6**

# **General Conclusions and Outlook**

This thesis has investigated the early stages of massive star formation based on a comprehensive set of observations with high spatial resolution. The observations comprised a large wavelength range from the near-infrared up to millimetre wavelengths. The emphasis, however, was given to observations in the thermal infrared.

Two regions of massive star formation have been analysed in detail. They are taken from a list of high-mass protostellar object candidates that will be investigated in a larger context by VLA 7-mm continuum observations. While detailed conclusions for the two case studies of G9.62+0.19-F and GGD 27-ILL are given in the corresponding Sections 3.9 and 4.5 we want to give some broader view in this final chapter.

As a result of our IR observations, two southern high-mass star-forming regions could be investigated in unprecedented detail. Their large degree of complexity has been revealed. We could show that the actual interesting sources remain invisible in the near-infrared due to their deep embedding in the dense gas and dust configurations of the natal molecular clouds and of the circumstellar material. Therefore, imaging in the thermal infrared turned out to be extremely useful to trace these seclusive objects.

We learned that the infrared appearance of complex star forming regions is not exclusively governed by the intrinsic spectral energy distribution of the YSOs but often dominated by the distribution and asymmetries of the extinguishing circumstellar material on several scales. The interaction of outflows from YSOs with their surroundings can lead to more complicated configurations. In particular, infrared emission associated with HMCs is detectable under certain favourable circumstances, as we demonstrated for G9.62+0.19-F.

The just mentioned interplay of wavelength-dependent extinction and the intrinsic SED of the embedded sources leads to fundamental changes in appearance of the massive star-forming regions with wavelength. These changes seem to be most dramatic in the range between 2 – 5 micrometre. Thus, imaging in the thermal infrared especially at the short wavelengths of the L' and nb\_M band (3.8 – 4.7  $\mu\text{m}$ ) is highly advisable in order to keep track of these morphologic transformations and to prevent misinterpretations.



While spatial low-resolution data, e.g., from the previous generation of IR satellites, could act as a principle guide line for investigating massive star formation, high-resolution observations are an essential tool to disentangle the objects in high-mass star-forming regions and to make any fundamental progress in that field. In this respect, an accurate astrometry is needed since it can have a strong impact on the interpretation of the data. Thus, careful and detailed investigations like the presented *ISAAC* campaign are crucial for the deeper understanding of the mechanisms of massive star formation. However, the *ISAAC* results represent only an intermediate step. Still higher resolution is required to study all the details of massive star formation – a task for powerful L' and nb\_M band Adaptive Optics systems on telescopes of the 8-m class like CONICA/NAOS.

The quest for the circumstellar disk around GGD 27-ILL will continue also after this thesis. However, we presented some indirect evidence that strengthens the hypothesis of a flattened compact structure around this massive young stellar object. In this regard, one remark might be in order that draws some parallels to another investigation.

Chini et al. (2004) reported the detection of a dark silhouette in M17 SW, seen in the NIR with an extension of roughly 20000 AU. They proposed that the entire configuration is a huge circumstellar disk around a potentially massive young (proto)star. We do not want to evaluate this claim here, and another group has already challenged this interpretation (Sako et al. 2005). We just want to show a certain similarity to our study of GGD 27-ILL. Like Chini and collaborators, we find in our infrared data a region of strong extinction covering the central area of a star-forming region. However, in our case, we can clearly separate a medium-sized slab of extinguishing material with a projected length of 10 – 15 arcseconds (20000 – 30000 AU), which dissects the central region and also covers GGD 27-ILL, from the immediate circumstellar structure that is compact in the L' and nb\_M band images ( $\leq 0.5$  arcseconds) and might harbour the actual circumstellar disk. This is supported by our VLA 7-mm imaging that sets strict limits for the size of the circumstellar structure around GGD 27-ILL to be smaller than 400 AU in diameter.

Our *SIMBA* observations at 1.2 mm have shown that large-scale mapping with the new generation of bolometer arrays is effective in tracing cold and dense dust cores in the farther vicinity of known sites of high-mass star formation. This technique will probably be extended in the near future when the new arrays *LABOCA* (at the *APEX* telescope in Chile) and *SCUBA2* (at the *JCMT* on Hawaii) come into operation. The stages prior to the HM-POs, the high-mass starless cores can be analysed in more detail. For several of these objects, star formation might already be ongoing in the interiors which might be detectable by far-infrared observations. We mention that the spectacular IRDCs shown in the northern part of our Fig. 5.3 are the target of very recently approved *Spitzer* observations with the instrument MIPS at 24  $\mu\text{m}$  and 70  $\mu\text{m}$  wavelength. For this observing proposal the author of this thesis acts as co-investigator.

We could successfully demonstrate, for the first time, the viability of the maser cross calibration method using 44 GHz Methanol masers.

First, this can be taken as a signpost for a promising future of *VLA* 7-mm work. In general, if sufficiently strong 44 GHz masers are found near to the science object, one does not rely on an external calibrator. Such calibrators are often located at large projected distances from the desired science target and hence limit the efficiency of the standard “fast switching” approach. The maser cross calibration ensures a quasi-continuous monitoring of the atmospheric phase shifts and its influence on the interferometric quantities. Under mediocre weather condition, maser cross calibration might be the only way to get results at all when operating the *VLA* at 7 mm in extended antenna configurations. We think that this technique will strongly propel 7-mm *VLA* work, first of all in the field massive star-forming regions. The recent work of Kurtz, Hofner & Vargas Álvarez (2004) has revealed that many regions containing HMPO candidates also contain 44 GHz methanol masers. A first 7-mm continuum investigation of a considerable fraction of this sample is in preparation (Hofner, Araya, Linz, et al.), and we have described some aspects about this subsample in Chapter 5. In addition, we mention as an interesting detail that also the object M8E-IR (a.k.a. IRAS 18018-2426 and Mol 37), one of the prime targets regarding our efforts to tackle massive YSOs with *MIDI* mid-infrared interferometry, is associated with 44 GHz Methanol masers (Slysh et al. 1999). These M8E-IR masers are several hundreds of Janskys strong and hence among the strongest 44 GHz Methanol masers known. These masers could enable us to observe this quite southern source (Declination  $-24.5^\circ$ ) with the *VLA* at 7-mm with high spatial resolution.

Second, the maser cross calibration method has the potential to influence interferometric work at (sub-)millimetre wavelengths and thus might turn out to be an important technique for the planned Atacama Large Millimeter Array (*ALMA*). This is also an issue since the usual calibrators for the centimetre wavelength range (mostly quasars and AGNi) are (too) weak at submillimetre wavelengths and the search for alternative, useable calibrators turns out to be a difficult business (cf. Su et al. 2004b).

## References

- Altenhoff, W., Mezger, P. G., Wendker, H., & Westerhout, G. 1960, Veröff. Sternwarte Bonn **59**, 48  
*Die Durchmusterung der Milchstraße und die Quellen-Durchmusterung bei 2.7 GHz*
- André, P., Ward-Thompson, D., & Barsony, M. 1993, ApJ **406**, 122  
*Submillimeter continuum observations of Rho Ophiuchi A – The candidate protostar VLA 1623 and prestellar clumps*
- Apai, D., Linz, H., Stecklum, B., & Henning, Th. 2005, A&A **434**, 987  
*Infrared portrait of the nearby massive star-forming region IRAS 09002-4732*
- Araya, E., Hofner, P., Churchwell, E., & Kurtz S. 2002, ApJS **138**, 63  
*Arecibo Observations of Formaldehyde and Radio Recombination Lines toward Ultracompact HII Regions*
- Aspin, C., McCaughrean, M. J., Casali, M. M., & Geballe, T. R. 1991, A&A **252**, 299  
*Near-IR imaging and spectroscopy of GGD27-IRS*
- Aspin, C., & Geballe, T. R. 1992, A&A **266**, 219  
*Mid-IR spectroscopy of GGD27-IRS: evidence for a PMS stellar cluster*
- Aspin, C. 1994, A&A **281**, L29  
*Scattered near-infrared CO emission bands in GGD 27-IRS*
- Aspin, C., Puxley, P. J., Blanco, B. R. et al. 1994, A&A **292**, L9  
*Thermal infrared imaging of GGD27-IRS. The active pre-main sequence star revealed*
- Beckert, Th., Duschl, W. J., & Mezger, P. G. 2000, A&A **356**, 1149  
*Free-free and recombination radiation from massive star-forming regions*
- Beckwith, S. V. W., & Sargent, A. I. 1991, ApJ **381**, 250  
*Particle emissivity in circumstellar disks*
- Beckwith, S. V. W., Henning, Th., & Nakagawa, Y. 2000, in Protostars & Planets IV, V. Mannings, A. Boss & S. Russel (eds.), University of Arizona Press, 533  
*Dust Properties and Assembly of Large Particles in Protoplanetary Disks*
- Beltrán, M. T., Girart, J. M., Estalella, R., & Ho, P. T. P. 2004, ApJ **426**, 941  
*The dense molecular cores in the IRAS 21391+5802 region*
- Benedettini, M., Molinari, S., Testi, L., Noriega-Crespo, A. 2004, MNRAS **347**, 295  
*Millimeter observations of the IRAS 18162-2048 outflow: evidence for cloud disruption around an intermediate-mass protostar*
- Bertero, M., Boccacci, P., & Robberto, M. 2000, PASP **112**, 1021  
*Wide-Field Imaging at Mid-Infrared Wavelengths: Reconstruction of Chopped and Nodded Data*
- Bessell, M. S., & Brett J. M. 1988, PASP **100**, 1134  
*JHKLM photometry - Standard systems, passbands, and intrinsic colors*
- Beuther, H., Schilke, P., Sridharan, T. K., et al. 2002a, A&A **383**, 892  
*Massive molecular outflows*

- Beuther, H., Schilke, P., Gueth, F., et al. 2002b, A&A **387**, 931  
*IRAS 05358+3543: Multiple outflows at the earliest stages of massive star formation*
- Beuther, H., Schilke, P., & Stanke, Th. 2003, A&A **408**, 601  
*Multiple outflows in IRAS 19410+2336*
- Beuther, H., & Shepherd, D. 2005, in: Cores to Clusters, Astrophysics and Space Science Library Series, in press (astro-ph/0502214)  
*Precursors of UCHII regions & the evolution of massive outflows*
- Beuther, H. 2005, private communication
- Bieging, J. H., Rieke, M. J., & Rieke, G. H. 2002, A&A **384**, 965  
*CO 1st overtone spectra of cool evolved stars: Diagnostics for hydrodynamic atmosphere models*
- Black, J. H., & van Dishoeck, E. F. 1987, ApJ **322**, 412  
*Fluorescent excitation of interstellar H<sub>2</sub>*
- Blumenberg, H. 2000, Suhrkamp Taschenbuch **3115**, Suhrkamp Verlag Frankfurt am Main  
*Die Vollzähligkeit der Sterne*
- Bogun, S., Lemke, D., Klaas, U., et al. 1996, A&A **315**, L71  
*First data from the ISOPHOT FIR Serendipity survey*
- Bonnarel, F., Fernique, P., Bienaymé, O., et al. 2000, A&AS **143**, 33  
*The ALADIN interactive sky atlas. A reference tool for identification of astronomical sources*
- Bonnell, I. A., Bate, M. R., & Zinnecker, H. 1998, MNRAS **298**, 93  
*On the formation of massive stars*
- Bonnell, I. A., Bate, M. R., Clarke, C. J., & Pringle, J. E. 2001a, MNRAS **323**, 785  
*Competitive accretion in embedded stellar clusters*
- Bonnell, I. A., Clarke, C. J., Bate, M. R., & Pringle, J. E. 2001b, MNRAS **324**, 573  
*Accretion in stellar clusters and the initial mass function*
- Bonnell, I. A., & Bate, M. R. 2002, MNRAS **336**, 659  
*Accretion in stellar clusters and the collisional formation of massive stars*
- Bonnell, I. A., Vine, S. G., & Bate, M. R. 2002, MNRAS **349**, 735  
*Massive stars formation: Nurture, not nature*
- Bouwman, J. 2001, PhD Thesis, Universiteit van Amsterdam  
*The processing and evolution of dust in Herbig Ae/Be systems*
- Brand, J. 1986, PhD Thesis (University of Leiden, Netherlands)  
*The velocity field of the outer galaxy*
- Briggs, D. S. 1995, PhD thesis, New Mexico Institute of Mining and Technology, Socorro  
*High Fidelity Deconvolution of Moderately Resolved Sources*
- Cardelli, J. A., Clayton, G. C., & Mathis, J. S. 1989, ApJ **345**, 245  
*The Relationship between infrared, optical, and ultraviolet extinction*
- Cesaroni, R., Churchwell, E., Hofner, P., Walmsley C. M., & Kurtz, S. 1994, A&A **288**, 903  
*Hot ammonia towards compact HII regions*
- Cesaroni, R., Hofner, P., Walmsley C. M., & Churchwell, E. 1998, A&A **331**, 709  
*Sub-arcsecond structure of hot cores in the NH<sub>3</sub> (4,4) line*
- Cesaroni, R. 2005, Ap&SS **295**, 5  
*Outflow, Infall, and Rotation in High-mass Star Forming Regions*
- Chan, S. J., Henning, Th., & Schreyer, K. 1996, A&AS **115**, 285,  
*A catalogue of massive young stellar objects*

- Chandler, C., & Wood, D. O. S. 1997, MNRAS **287**, 445  
*VLA observations of 43-GHz continuum and CS J=1–0 emission from Orion–IRc2 and the hot core*
- Chini, R., Kimeswenger, S., Hoffmeister, V., et al. 2004, Nature **429**, 155  
*The formation of a massive protostar through the disk accretion of gas*
- Churchwell, E. 1999, in *The Origin of Stars and Planetary Systems*, ed. C. Lada, & N. Kylafis, NATO Science Series, 540 (Kluwer), 515  
*Massive Star Formation*
- Crowther P. A., & Conti P. S. 2003, MNRAS **343**, 143  
*MSX Mid Infrared Imaging of Massive Star Birth Environments. I: Ultracompact HII Regions*
- Cutri, R. M., Skrutskie, M. F., van Dyk, S., et al. 2003, 2MASS All–Sky Catalog of Point Sources, VizieR On–line Data Catalog: II/246. Originally published in: University of Massachusetts and Infrared Processing and Analysis Center
- D’Alessio, P., Calvet, N., Hartmann, L. 2001, ApJ **553**, 321  
*Accretion Disks around Young Objects. III. Grain Growth*
- Danby, G., Flower, D. R., Valiron, P., Schilke, P., & Walmsley, C. M. 1988, MNRAS **235**, 229  
*A recalibration of the interstellar ammonia thermometer*
- Davis, C. J., Ray, T. P., Desroches, L., & Aspin, C. 2001, MNRAS **326**, 524  
*Near–infrared echelle spectroscopy of Class I protostars: molecular hydrogen emission–line (MHEL) regions revealed*
- De Buizer, J. M., Piña, R. K., & Telesco, C. M. 2000, ApJS **130**, 437  
*Mid–Infrared Imaging of Star–forming Regions Containing Methanol Masers*
- De Buizer, J. M., Watson, A. M., Radomski, J. T., Piña, R. K., & Telesco C. M. 2002, ApJ **564**, L101  
*Mid–Infrared Detection of a Hot Molecular Core in G29.96–0.02*
- De Buizer, J. M., Radomski, J. T., Telesco, C. M., & Pina, R. K. 2003, ApJ **598**, 1127  
*A search for mid–infrared emission from hot molecular core candidates*
- Dorschner, J., Begemann, B., Henning, T., Jäger, C., & Mutschke, H. 1995, A&A **300**, 503  
*Steps toward interstellar silicate mineralogy. II. Study of Mg–Fe–silicate glasses of variable composition*
- Dougados, C., Léna, P., Ridgway, S. T., Christou, J. C., & Probst, R. G. 1993, ApJ **406**, 112  
*Near–infrared imaging of the Becklin–Neugebauer–IRc2 region in Orion with subarcsecond resolution*
- Downes, D., Wilson, T. L., Bieging, J., & Wink J. 1980, ApJS **40**, 379  
*H110– $\alpha$  and H<sub>2</sub>CO survey of galactic radio sources*
- Draine, B. T., & Lee, H. M. 1984, ApJ **285**, 89  
*Optical properties of interstellar graphite and silicate grains*
- Draine, B. T., & Bertoldi, F. 1996, ApJ **468**, 269  
*Structure of Stationary Photodissociation Fronts*
- Draine, B. T. 2003, ARA&A **41**, 241  
*Interstellar dust grains*
- Edgar, R., & Clarke, C. 2003, MNRAS **338**, 962  
*A new algorithm for radiative feedback and its application to the formation of massive stars*
- Edgar, R., & Clarke, C. 2004, MNRAS **338**, 962  
*The effect of radiative feedback on Bondi–Hoyle flow around a massive star*
- Egan, M. P., & Price S. D. 1996, AJ **112**, 2862  
*The MSX Infrared Astometric Catalog*
- Egan, M. P., Shipman, R. F., Price, S. D., et al. 1998, ApJ **494**, L199  
*A Population of Cold Cores in the Galactic Plane*

- Evans, N. J. II, Shirley, Y. L., Mueller, K. E., & Knez, C. 2002, in: Hot Star Workshop III, P. A. Crowther (ed.), ASP Conf. Ser. **267**, 17  
*Early Phases and Initial Conditions for Massive Star Formation*
- Elmegreen, B. G. 2000, ApJ **530**, 277  
*Star Formation in a Crossing Time*
- Epchtein, N., Deul, E., Derriere S., et al. 1999, A&A **349**, 236  
*A preliminary database of DENIS point sources*
- Faúndez, S., Bronfman, L., Garay, G., et al. 2004, A&A **426**, 97  
*SIMBA survey of southern high-mass star forming regions. I. Physical parameters of the 1.2 mm/IRAS sources*
- Feigelson, E. D., Broos, P., Gaffney III, J. A., et al. 2002, ApJ **574**, 258  
*X-Ray-emitting Young Stars in the Orion Nebula*
- Feldt, M., Stecklum, B., Henning, Th., et al. 1998, A&A **339**, 759  
*The ultracompact HII region G45.45+0.06. A pearl necklace in the sky*
- Feldt, M., Stecklum, B., Henning, Th., Launhardt, R., & Hayward, T. L. 1999, A&A **346**, 243  
*High-resolution imaging of ultracompact HII regions regions. II. G5.89–0.39 revisited*
- Fernandes, A., Brand, P. W. J. L., & Burton, M. 1995, Ap&SS **233**, 45  
*H<sub>2</sub> Fluorescence in HH7 and DR21*
- Fischer, O., Henning, Th., & Yorke H. W. 1996, A&A **308**, 863  
*Simulation of polarization maps. II. The circumstellar environment of pre-main sequence objects*
- Frémat, Y., Zorec, J., Hubert, A.-M., & Floquet, M. 2005, A&A, accepted, astro-ph/0503381  
*Effects of gravitational darkening on the determination of fundamental parameters in fast rotating B-type stars*
- Garay G., Rodríguez L.F., Moran J.M., & Churchwell E., 1993, ApJ **418**, 368  
*VLA Observations of Strong IRAS Point Sources Associated with Compact HII Regions*
- Garay, G., Moran, J. M., Rodríguez, L. F., & Reid, M. J. 1998, ApJ **492**, 635  
*The G19.6–0.2 Region of Star Formation: Molecular and Ionized Environs*
- Garay, G., & Lizano, S. 1999, PASP **111**, 1049  
*Massive Stars: Their Environment and Formation*
- Gaume, R. A., Claussen, M. J., de Pree, C. G., Goss, W. M., & Mehringer, D. M. 1995, ApJ **449**, 663  
*The Sagittarius B2 Star-forming Region. I. Sensitive 1.3 Centimeter Continuum Observations*
- Gezari, D. Y., Backman, D. E., & Werner, M. W. 1998, ApJ **509**, 283  
*Mid-Infrared Imaging of Orion BN/KL. II. Luminosity Sources, Extinction Distribution, and the Nature of IRc2*
- Gezari, D. Y., Danchi, W. C., Greenhill, L. J., & Varosi, F. 2003, IAU Symp. **221**, M. G. Burton, R. Jayawardhana, & T. L. Bourke (eds.), E212  
*Mid-Infrared Imaging of Orion BN/KL with Keck I Telescope*
- Gibb, A. G., Hoare, M. G., Mundy, L. G., & Wyrowski, F. 2004a, in: Star Formation at High Angular Resolution, R. Jayawardhana, M. G. Burton & T. L. Bourke (eds.), IAU Symp. **221**, 425  
*A search for disks around massive young stellar objects*
- Gibb, A. G., Wyrowski, F., & Mundy, L. G. 2004b, ApJ **616**, 301  
*High-velocity gas toward Hot Molecular Cores: Evidence for collimated outflows from embedded sources*
- Girart, J. M., Rodríguez, L. F., Anglada, G., et al. 1994, ApJL **435**, 145  
*Ammonia downstream from HH 80 North*

- Girart, J. M., Estalella, R., Viti, S., Williams, D. A., & Ho, P. T. P. 2001, ApJL **562**, 91  
*Star Formation Signatures in the Condensation Downstream of HH 80N*
- Gómez, Y., Rodríguez, L. F., & Martí, J. 1995, ApJ **453**, 268  
*Thermal jets and H<sub>2</sub>O masers: The case of HH 80–81*
- Gómez, Y., Rodríguez–Rico, C. A., Rodríguez, L. F., & Garay, G. 2000, Rev. Mex. Astron. Astrofis. **36**, 161  
*A New Warm Molecular Clump toward the Star Forming Region G34.26+0.15*
- Gómez, Y., Rodríguez, L. F., Girart, J. M., Garay, G., & Martí, J. 2003, ApJ **597**, 414  
*VLA and BIMA observations toward the exciting source of the massive HH 80–81 outflow*
- Grady, C. A., Woodgate, B., Torres, C. A., O., et al. 2004, ApJ **608**, 809  
*The environment of the optically brightest Herbig Ae star HD 104732*
- Guibert, J. 1992, in Proceedings of the Conference on Digitised Optical Sky Surveys, H. T. MacGillivray & E. B. Thomson (eds.), Dordrecht, Kluwer, 103  
*The MAMA Facility - a Survey of Scientific Programmes*
- Gyulbudaghian, A. L., Glushkov, Yu. J., Denisyuk, E. K. 1978, ApJ **224**, L137  
*Herbig–Haro Objects*
- Hartigan, P., & Lada, C. J. 1985, ApJS **59**, 383  
*CCD images of suspected Herbig–Haro objects*
- Hartmann, L. 2002, ApJ **578**, 914  
*Flows, Fragmentation, and Star Formation. I. Low–Mass Stars in Taurus*
- Hatchell J., Thompson M. A., Millar T. J., & Macdonald G. H. 1998, A&AS **133**, 29  
*A survey of molecular line emission towards ultracompact HII regions*
- Hayward, T. L., Miles, J. W., Houck, J. R., Gull, G. E., & Schoenwald, J. 1993, Proc. SPIE **1946**, 334  
*SpectroCam-10: a 10- $\mu$ m spectrograph/camera for the Hale Telescope*
- Heathcote, S., Reipurth, B., & Raga, A. C. 1998, AJ **116**, 1940  
*Structure, Excitation, and Kinematics of the Luminous Herbig–Haro Objects 80/81*
- Henning, Th. 1990, Fundamentals of Cosmic Physics **14**, 321  
*Formation and Early Evolution of Massive Stars*
- Henning, Th., Schreyer, K., Launhardt, R., & Burkert, A. 2000, A&A **353**, 211  
*Massive young stellar objects with molecular outflows*
- Henning, Th., Launhardt, R., Stecklum, B., & Wolf, S. 2002, in: The Origins of Stars and Planets – The VLT View., J. Alves & M. McCaughrean (eds.), ESO Astrophysics Symposia, 79  
*Continuum Polarization as a Tool: A Perspective for VLT and ALMA*
- Henning, Th., Feldt, M., & Stecklum, B. 2002, in ASP Conf. Ser. **267**, Hot Star Workshop III: The earliest stages of massive star birth, P. A. Crowther (ed.), 153  
*High–Resolution Studies of Massive Star–Forming Regions*
- Hofner, P., Kurtz, S., Churchwell, E., Walmsley, C. M., & Cesaroni, R. 1994, ApJ **429**, L85  
*High–resolution observations of a new ammonia maser line in G9.62+0.19*
- Hofner, P., Kurtz, S., Churchwell, E., Walmsley, C. M., & Cesaroni, R. 1996, ApJ **460**, 359  
*Massive Star Formation in the Hot, Dense Cloud Core of G9.62+0.19*
- Hofner, P., & Churchwell, E. 1996, A&AS **120**, 283  
*A survey of water maser emission toward ultracompact HII regions*
- Hofner, P., Wiesemeyer H., & Henning, Th. 2001, ApJ **549**, 425  
*A high velocity outflow from the G9.62+0.19 star forming region*
- Hofner, P., Delgado, H., Whitney, B., Churchwell, E., & Linz, H. 2002, ApJL **579**, L95  
*X–Ray detection of the ionizing stars in ultracompact HII regions*

- Hummer, D. G., & Storey, P. J. 1987, MNRAS **224**, 801  
*Recombination–line intensities for hydrogenic ions. I – Case B calculations for H I and He II*
- Hunter, T. R., Churchwell, E., Watson, C., et al. 2000, AJ **119**, 2711  
*350  $\mu\text{m}$  images of massive star–forming regions*
- Indebetouw, R., Mathis, J. S., Babler, B. L., et al. 2005, ApJ **619**, 931  
*The wavelength dependence of interstellar extinction from 1.25 to 8.0  $\mu\text{m}$  using GLIMPSE data*
- Jaffe, D. T., Stier, M. T., & Fazio, G. G. 1982, ApJ **252**, 601,  
*A high resolution far–infrared survey of a section of the galactic plane. I. The nature of the sources*
- Kalenskii, S. V., Bachiller, R., Berulis, I. I., et al. 1992, Sov. Astron. **36**, 517  
*Search for methanol masers at 44 GHz*
- Kaufman, M. J., Hollenbach, D. J., & Tielens, A. G. G. M. 1998, ApJ **497**, 276  
*High–Temperature Molecular Cores near Massive Stars and Application to the Orion Hot Core*
- Kemper, F., Waters, L. B. F. M., de Koter, A., & Tielens, A. G. G. M. 2001, A&A **369**, 132  
*Crystallinity versus mass-loss rate in asymptotic giant branch stars*
- Keto, E. 2002, ApJ **580**, 980  
*On the Evolution of Ultracompact HII Regions*
- Keto, E. 2003, ApJ **599**, 1196  
*The formation of massive stars by accretion through trapped Hypercompact HII Regions*
- Kim, K.–T., & Koo, B.–C. 2003, ApJ **596**, 362  
*Molecular Counterparts of Ultracompact HII Regions with extended envelopes*
- Krause, O., Lemke, D., Tóth, L. V., et al. 2003, A&A **398**, 1007  
*A very young star forming region detected by the ISOPHOT Serendipity Survey*
- Krügel, E., & Walmsley, C. M. 1984, A&A **130**, 5  
*Dust and gas temperatures in dense molecular clouds*
- Kudritzki, R. P., Hummer, D. G., Pauldrich, A. W. A., et al. 1992, A&A **257**, 655  
*Radiation–driven winds of hot luminous stars. X. The determination of stellar masses, radii, and distances from terminal velocities and mass–loss rates*
- Kurtz, S. E., Churchwell, E., & Wood, D. O. S. 1994, ApJS **91**, 659  
*Ultracompact HII regions. II: New high–resolution radio images*
- Kurtz, S., Cesaroni, R., Churchwell, E., Hofner, P., & Walmsley, C. M. 2000, in Protostars & Planets IV, V. Mannings, A. Boss & S. Russel (eds.), University of Arizona Press, 299  
*Hot Molecular Cores and the Earliest Phases of High–Mass Star Formation*
- Kurtz, S. E. 2000, Rev. Mex. Astron. Astrofis. **9**, 169  
*Ultracompact HII Regions: New Challenges*
- Kurtz, S. E., Hofner, P., & Vargas Álvarez, C. 2004, ApJS **155**, 149  
*A catalog of CH<sub>3</sub>OH 7<sub>0</sub> – 6<sub>1</sub> A<sup>+</sup> maser sources in massive star–forming regions*
- Kurucz, R. 1993, Model atmospheres. CD-ROM Nos. 1–18, Cambridge, Mass.: Smithsonian Astrophysical Observatory.
- Larson, R. B., & Starrfield, S. 1971, A&A **13**, 190  
*On the Formation of Massive Stars and the Upper Limit of Stellar Masses*
- Larson, R. B. 2003, Rept. Prog. Phys. **66**, 1651  
*The physics of star formation*
- Lasker, B., Sturch, C. H., McLean, B. J., et al. 1990, AJ **99**, 2019  
*The Guide Star Catalog. I - Astronomical foundations and image processing*



- Leinert, C., Graser, U., Waters, L. B. F. M., et al. 2003, Proc. SPIE **4838**, 893  
*Ten-micron instrument MIDI: getting ready for observations on the VLT*
- Li, D., Goldsmith, P. A., & Xie, T. 1999, ApJ **522**, 897  
*A new method for determining the dust temperature distribution in star-forming regions*
- Liu, S.-Y. 2003, IAUS **221**, M. G. Burton, R. Jayawardhana, & T. L. Bourke (eds.), E233  
*OVRO Observations of Hot Molecular Cores*
- Lockman, F. J. 1989, ApJS **71**, 469  
*A survey of radio HII regions in the northern sky*
- Lumsden, S. L., Hoare, M. G., Oudmaijer, R. D., Richards, D. 2002, MNRAS **336**, 621,  
*The population of the Galactic plane as seen by MSX*
- Lutz, D., Feuchtgruber, H., Genzel, R., et al. 1996, A&A **315**, L269  
*SWS observations of the Galactic center*
- Maeder, A. 1999, A&A **347**, 185  
*Stellar evolution with rotation IV: von Zeipel's theorem and anisotropic losses of mass and angular momentum*
- Mangum, J. G., Wootten, A., & Mundy, L. G. 1991, ApJ **378**, 576  
*Synthesis imaging of the DR 21(OH) cluster. I – Dust continuum and C<sup>18</sup>O emission*
- Mangum, J. G., Wootten, A., & Mundy, L. G. 1992, ApJ **388**, 467  
*Synthesis imaging of the DR 21(OH) cluster. II – Thermal ammonia and water maser emission*
- Manske, V., & Henning, Th. 1998, A&A **337**, 85  
*Two-dimensional radiative transfer with transiently heated particles: methods and applications*
- Martí, J., Rodríguez, L. F., & Reipurth, B. 1993, ApJ **416**, 208  
*HH 80–81: A Highly Collimated Herbig–Harro Complex Powered by a Massive Young Star*
- Martí, J., Rodríguez, L. F., & Reipurth, B. 1995, ApJ **449**, 184  
*Large Proper Motions and Ejection of New Condensations in the HH 80–81 Thermal Radio Jet*
- Martí, J., Rodríguez, L. F., & Reipurth, B. 1998, ApJ **502**, 337  
*Proper Motions of the Inner Condensations in the HH 80–81 Thermal Radio Jet*
- Martí, J., Rodríguez, L. F., & Torrelles, J. M. 1999, A&A **345**, L5  
*Cross-calibrated VLA observations of H<sub>2</sub>O maser and 1.3 cm continuum emission in IRAS 18162-2048 (= HH 80–81 IRS)*
- Martín-Hernández, N. L., van der Hulst, J. M., & Tielens A. G. G. M. 2003, A&A **407**, 957,  
*A radio continuum and infrared study of Galactic HII regions*
- Martins, F. Schaerer, D., & Hillier, D. J. 2005, A&A **436**, 1049  
*A new calibration of stellar parameters of Galactic O stars*
- Mathis, J. S., Rumpl, W., & Nordsieck, K. H. 1977, ApJ **217**, 425  
*The size distribution of interstellar grains*
- Mathis, J. S. 1990, ARA&A **28**, 37  
*Interstellar dust and extinction*
- McCabe, C., Duchene, G., & Ghez, A. M. 2003, ApJ **588**, L113  
*The First Detection of Spatially Resolved Mid-Infrared Scattered Light from a Protoplanetary Disk*
- McCartney, M. S. K., Brand, P. W. J. L., Burton, M. G., & Chrysostomou, A. 1999, MNRAS **307**, 315  
*Fluorescent H<sub>2</sub> in the reflection nebula NGC 2023 - I. Recent observations*
- McCutcheon, W. H., Sato, T., Purton, C. R., Matthews, H. E., & Dewdney, P. E. 1995, AJ **110**, 1762  
*Millimeter and submillimeter wavelength continuum observations of massive young stellar objects*

- McKee, C. F., & Tan, J. C. 2003, ApJ **585**, 850  
*The Formation of Massive Stars from Turbulent Cores*
- McLaughlin, D. E., & Pudritz, R. E. 1997, ApJ **476**, 750  
*Gravitational Collapse and Star Formation in Logotropic and Nonisothermal Spheres*
- Menten, K. M., & Reid, M. J. 1995, ApJ **445**, L157  
*What is powering the Orion Kleinman–Low infrared nebula*
- Menten, K. M., & van der Tak, F. F. S. 2004, A&A **414**, 289  
*Very compact radio emission from high–mass protostars. I. CRL 2136: Continuum and water maser observations*
- Mezger, P. G., & Henderson, A. P. 1967, ApJ **147**, 471  
*Galactic H II Regions. I. Observations of Their Continuum Radiation at the Frequency 5 GHz*
- Millar, T. J. 1997, in IAU Symp. **178**: Molecules in Astrophysics, E. F. van Dishoeck (ed.), 75  
*Models of Hot Molecular Cores*
- Minchin, N. R., Hough, J. H., McCall, A., et al. 1991, MNRAS **248**, 715  
*Near–infrared imaging polarimetry of bipolar nebulae. I – The BN-KL region of OMC-1*
- Minier, V., Booth, R. S., Ellingsen, S. P., Conway, J. E., & Pestalozzi, M. R. 2001, in Proc. of the 5th EVN Symposium, J. E. Conway et al. (eds.), 178  
*Methanol masers: tracers of outflows?*
- Molinari, S., Brand, J., Cesaroni, R., & Palla, F. 1996, A&A **308**, 573,  
*A search for precursors of ultracompact HII regions in a sample of luminous IRAS sources. I. Association with ammonia cores*
- Molinari, S., Brand, J., Cesaroni, R., Palla, F., & Palumbo, G. G. C. 1998, A&A **336**, 339,  
*A search for precursors of ultracompact HII regions in a sample of luminous IRAS sources. II. VLA observations*
- Molinari, S., Brand, J., Cesaroni, R., & Palla, F. 2000, A&A **355**, 617,  
*A search for precursors of ultracompact HII regions in a sample of luminous IRAS sources. III. Circumstellar dust properties*
- Molinari, S., Noriega–Crespo, A., & Spinoglio, L. 2001, ApJ **547**, 292  
*A shock–induced photodissociation region in the HH 80/81 flow: Far –infrared Spectroscopy*
- Molinari, S., Testi, L., Rodríguez, L. F., Zhang, Q. 2002, ApJ **570**, 758,  
*The formation of massive stars. I. High–resolution millimeter and radio studies of high–mass protostellar candidates*
- Molinari, S. 2004, private communication
- Moorwood, A. F. 1997, in Proc. SPIE **2871**, A. L. Ardeberg (ed.), 1146  
*ISAAC: a 1- to 5- $\mu$ m imager/spectrometer for the VLT*
- Monet, D., Bird, A., Canzian, B., et al. 1998: USNO-A V2.0, A Catalog of Astrometric Standards, U.S. Naval Observatory Flagstaff Station (USNOFS) and Universities Space Research Association (USRA) stationed at USNOFS.
- Nakano, T., Hasegawa, T., Morino, J.–I., & Yamashita, T. 2000, ApJ **534**, 976  
*Evolution of Protostars Accreting Mass at Very High Rates: Is Orion IRC2 a Huge Protostar?*
- Nielbock, M., Chini, R., & Müller, S. A. H. 2003, A&A **408**, 245,  
*The stellar content of OMC 2/3*
- Nomura, H., & Millar, T. J. 2004, A&A **414**, 409  
*The physical and chemical structure of hot molecular cores*

- Nyman, L.-Å., Lerner, M., Nielbock, M., et al. 2001, ESO Messenger **106**, 40  
*SIMBA explores the southern sky*
- Ochsenbein, F., Bauer, P., & Marcout, J. 2000, A&AS **143**, 221  
*The VizieR database of astronomical catalogues*
- Ohishi, M. 1997, in IAU Symp. **178**: Molecules in Astrophysics, E. F. van Dishoeck (ed.), 61  
*Observations of “Hot Cores”*
- Olmi L., Cesaroni R., Neri R., & Walmsley C. M. 1996, A&A **315**, 565  
*High resolution CH<sub>3</sub>CN observations towards hot cores*
- Osorio, M., Lizano, S., & D’Alessio, P. 1999, ApJ **528**, 808  
*Hot Molecular Cores and the Formation of Massive Stars*
- Ossenkopf, V., & Henning, Th. 1994, A&A **291**, 943  
*Dust opacities for protostellar cores*
- Osterbrock, D. E. 1989, Astrophysics of Gaseous Nebulae and Active Galactic Nuclei, University of Science Books, Sausalito, California
- Padoan, P., & Nordlund, Å. 2002, ApJ **576**, 870  
*The Stellar Initial Mass Function from Turbulent Fragmentation*
- Palla, F., Brand, J., Comoretto, G., Felli, M., & Cesaroni, R. 1991, A&A **246**, 249  
*Water masers associated with dense molecular clouds and ultracompact HII regions*
- Pantin E., & Starck J.-L., 1996, A&AS **118**, 575  
*Deconvolution of astronomical images using the multiscale maximum entropy method*
- Pascucci, I., Apai, D., Henning, Th., Stecklum, B., & Brandl, B. 2004, A&A **426**, 523  
*The Hot Core – Ultracompact HII Connection in G10.47+0.03*
- Peeters, E., Martín-Hernández, N. L., Damour, F., et al. 2002, A&A **381**, 571  
*ISO spectroscopy of compact HII regions in the Galaxy. I. The catalogue*
- Peeters, E., Hony, S., Van Kerckhoven, C., et al. 2002, A&A **390**, 1089  
*The rich 6 to 9  $\mu$ m spectrum of interstellar PAHs*
- Persi, P., Tapia, M., Roth, M., et al. 2003, A&A **397**, 227,  
*Near and Mid-infrared images of the massive star forming complex G9.62+0.19*
- Persson, S. E., Murphy, D. C., Krzeminski, W., Roth, M., & Rieke M. J. 1998, AJ **116**, 2475  
*A New System of Faint Near-Infrared Standard Stars*
- Phillips, C. J., Norris, R. P., Ellingsen, S. P., & McCulloch, P. M. 1998, MNRAS **300**, 1131  
*Methanol masers and their environment at high resolution*
- Pravdo, S. H., Tsuboi, Y., & Maeda, Y. 2004, ApJ, **605**, 259  
*X-Rays from HH 80, HH 81, and the Central Region*
- Preibisch, Th., Ossenkopf, V., Yorke, H. W., & Henning, Th. 1993, A&A **279**, 577  
*The influence of ice-coated grains on protostellar spectra*
- Price, N. M., & Podsiadlowski, Ph. 1995, MNRAS **273**, 1041  
*Dynamical interactions between young stellar objects and a collisional model for the origin of the stellar mass spectrum*
- Price, S. D., Egan, M. P., Carey, S. J., Mizuno, D. R., & Kuchar, Th. A. 2001, AJ **121**, 2819,  
*Midcourse Space Experiment Survey of the Galactic plane*
- Ramírez, S. V., Depoy, D. L., Frogel, J. A., Sellgren, K., & Blum, R. D. 1997, AJ **113**, 1411  
*Luminosity and Temperature from Near-Infrared Spectra of Late-Type Giant Stars*

- Reichert, L. A., Weferling, B., Esch, B., & Kreysa, E. 2001, *A&A* **379**, 735  
*The fastscanning observing technique for millimeter and submillimeter astronomy*
- Reid, M. J., & Menten, K. M. 1990, *ApJ* **360**, L51  
*A subarcsecond H<sub>2</sub>O maser shell surrounding a variable star*
- Reimann, H.-G., Linz, H., Wagner, R., et al. 2000, in Proc. SPIE **4008**, M. Iye & A. F. Moorwood (eds.), 1132  
*TIMM12: a new multimode mid-infrared instrument for the ESO 3.6-m telescope*
- Reipurth, B., & Graham, J. A. 1988, *A&A* **202**, 219  
*New Herbig–Haro objects in star-forming regions*
- Reynolds, S. P. 1986, *ApJ* **304**, 713  
*Continuum spectra of collimated, ionized stellar winds*
- Richer, J. S., Shepherd, D. S., Cabrit, S., Bachiller, R., & Churchwell, E. 2000, in *Protostars & Planets IV*, V. Mannings, A. Boss & S. Russel (eds.), University of Arizona Press, 867  
*Molecular Outflows from Young Stellar Objects*
- Rieke, G. H., & Lebofsky, M. J. 1985, *ApJ* **288**, 618  
*The interstellar extinction law from 1 to 13 microns*
- Robberto, M., Beckwith, S. V. W., Panagia, N., et al. 2005, *AJ* **129**, 1534  
*The Orion Nebula in the Mid-Infrared*
- Rodgers, S. D., & Charnley, S. B. 2001, *ApJ* **546**, 324  
*Chemical Differentiation in Regions of Massive Star Formation*
- Rodgers, S. D., & Charnley, S. B. 2003, *ApJ* **585**, 355,  
*Chemical evolution in protostellar envelopes: Cocoon chemistry*
- Rodríguez, L. F., Moran, J. M., Ho, P. T. P., & Gottlieb, E. W. 1980, *ApJ* **235**, 845  
*Radio observations of water vapor, hydroxyl, silicon monoxide, ammonia, carbon monoxide, and compact HII regions in the vicinities of suspected Herbig–Haro objects*
- Rouan, D., & Leger, A. 1984, *A&A* **132**, L1  
*Large grains in Orion are indicated by IR polarization and flux data*
- Ryter, Ch. E. 1996, *Ap&SS* **236**, 285  
*Interstellar Extinction from Infrared to X-Rays: an Overview*
- Sako, S., Yamashita, T., Kataza, H., et al. 2005, *Nature* **434**, 995  
*No high-mass protostars in the silhouette young stellar object M17–SO1*
- Schlegel, D. J., Finkbeiner, D. B., & Davis, M. 1998, *ApJ* **500**, 525  
*Maps of Dust Infrared Emission for Use in Estimation of Reddening and Cosmic Microwave Background Radiation Foregrounds*
- Schmidt, M. 1965, in: *Stars and Stellar Systems V. Galactic Structure*, A. Blaauw & M. Schmidt (eds.), University Press, Chicago, p. 513–530  
*Rotation Parameters and Distribution of Mass in the Galaxy*
- Schreyer, K., Henning, Th., Kömpe, C., & Harjunpää, P. 1996, *A&A*, 306, 267  
*NH<sub>3</sub> and HCO<sup>+</sup> towards luminous IRAS sources*
- Schreyer, K., Stecklum, B., Linz, H., & Henning, Th. 2003, *ApJ* **599**, 335  
*NGC2264 IRS1: The central engine and its cavity*
- Serkowski, K. 1962, *Advances in Astronomy and Astrophysics*, **1**, 289  
*Polarisation of starlight*
- Shepherd, D., & Churchwell, E. 1996, *ApJ* **472**, 225  
*Bipolar Molecular Outflows in Massive Star Formation Regions*

- Shu, F. H., Adams, F. C., & Lizano, S. 1987, ARA&A, **25**, 23  
*Star formation in molecular clouds - Observation and theory*
- Shuping, R. Y., Bally, J., Morris, M., & Throop, H. 2003, ApJ **587**, L109  
*Evidence for Grain Growth in the Protostellar Disks of Orion*
- Siebenmorgen, R., Krügel, E., & Spoon, H. W. W. 2004, A&A **414**, 123  
*Mid-infrared emission of galactic nuclei. TIMMI2 versus ISO observations and models*
- Simmons, J. F. L., & Stewart, B. G. 1985, A&A **142**, 100  
*Point and interval estimation of the true unbiased degree of linear polarization in the presence of low signal-to-noise ratios*
- Slysh, V. I., Val'ts, I. E., Kalenskii, S. V., & Golubev, V. V. 1999, Astron. Rep. **43**, 785 (S99)  
*Fine spatial structure of methanol masers*
- Sridharan, T. K., Beuther, H., Schilke, P., Menten, K. M., & Wyrowski, F. 2002, ApJ **566**, 931  
*High-Mass Protostellar Candidates. I. The Sample and Initial Results*
- Stahler, S. W., Palla, F., & Ho, P. T. P. 2000, in Protostars & Planets IV, V. Mannings, A. Boss & S. Russel (eds.), University of Arizona Press, 327  
*The Formation of Massive Stars*
- Stecklum, B., Feldt, M., Richichi, A., Calamai, G., & Lagage, P. O. 1997, ApJ **479**, 339  
*High-Resolution Infrared Observations of GGD 27*
- Stecklum, B., Brandl, B., Feldt, M., et al. 2002, in The Origins of Stars and Planets – The VLT View., J. Alves & M. McCaughrean (eds.), ESO Astrophysics Symposia, 225  
*Infrared Observation of Hot Cores*
- Stecklum, B., Brandl, B., Feldt, M., Henning, Th., & Pascucci, I. 2002, A&A **392**, 1025  
*High resolution mid-infrared imaging of W3(OH)*
- Stecklum, B., Feldt, M., Henning, Th., Käufel H. U., & Wolf, S. 2003, in ASP Conf. Ser. **287**, Galactic Star Formation Across the Stellar Mass Spectrum, J. De Buizer (ed.), astro-ph/0206457  
*Infrared Imaging Polarimetry of Massive Star-forming Regions*
- Stecklum, B., Henning, Th., Apai, D., & Linz, H. 2003, in Proc. SPIE **4834**, G. Guhathakurta (ed.), 337  
*VLT-ISAAC observations of massive star-forming regions*
- Su, Y.-N., Zhang, Q., & Lim, J. 2004a, ApJ **604**, 258  
*Bipolar Molecular Outflows from High-Mass Protostars*
- Su, Y.-N., Liu, S.-Y., Lim, J., et al. 2004b, ApJL **616**, 39  
*Search for Calibrators for the Submillimeter Array: I. High-Mass Star Forming Regions*
- Su, Y.-N. 2004, PhD Thesis, National Central University, Taiwan  
*A Millimeter and Sub-Millimeter Study of High-Mass Star Formation*
- Tamura, M., Gatley, I., & Joyce, R. R., et al. 1991, ApJ **378**, 611  
*Infrared polarization images of star-forming regions. I - The ubiquity of bipolar structure*
- Tenorio-Tagle, G. 1979, A&A **71**, 59  
*The gas dynamics of HII regions. I - The champagne model*
- Terebey, S., Shu, F., & Cassen, P. 1984, ApJ **286**, 529  
*The collapse of the cores of slowly rotating isothermal clouds*
- Testi, L., Felli, M., Persi, P., & Roth, M. 1998, A&A **329**, 233  
*HII and hot dust emission around young massive stars in G9.62+0.19*
- Testi, L., Hofner, P., Kurtz, S., & Rupen, M. 2000, A&A **359**, L5  
*Detection of the thermal radio continuum emission from the G9.62+0.19-F Hot Core*

- Testi, L. 2001, private communication
- Tieftrunk, A. R., Gaume, R. A., Claussen, M. J., Wilson, T. L., & Johnston, K. J. 1997, *A&A* **318**, 931  
*The HII/molecular cloud complex W3 revisited: imaging the radio continuum sources using multi-configuration, multi-frequency observations with the VLA*
- Torrelles, J. M., Gómez, J. F., Rodríguez, L. F., et al. 1996, *ApJ* **457**, L107  
*The thermal radio jet of Cepheus A HW2 and the water maser distribution at 0'.08 Scale (60 AU)*
- Urban, S. E., Corbin, T. E., & Wycoff, G. L. 1997, *The ACT Reference Catalogue*, U.S. Naval Observatory, Washington D.C.
- Vallée, J. P., & Bastien, P. 2000, *ApJ* **530**, 806  
*Magnetic orientations and energetics in interstellar clumps within small clouds*
- van der Blik, N. S., Manfroid, J., & Bouchet, P. 1996, *A&AS* **119**, 547  
*Infrared aperture photometry at ESO (1983–1994) and its future use*
- van der Tak, F. F. S., & Menten, K. M. 2005, *A&A* **437**, 947  
*Very compact radio emission from high-mass protostars. II. Dust disks and ionized accretion flows*
- von Zeipel, H. 1924, *MNRAS* **84**, 665  
*The radiative equilibrium of a rotating system of gaseous masses*
- Walmsley, C. M., & Ungerechts, H. 1983, *A&A* **122**, 164  
*Ammonia as a molecular cloud thermometer*
- Walmsley, C. M. 1995, *Rev. Mex. (Ser. de Conf.)* **1**, 137  
*Dense Cores in Molecular Clouds*
- Walsh, A. J., Burton, M. G., Hyland, A. R., & Robinson, G. 1999, *MNRAS* **309**, 905  
*Studies of ultracompact HII regions - III. Near-infrared survey of selected regions*
- Wardle, J. F. C., & Kronberg, P. P. 1974, *ApJ* **194**, 249  
*The linear polarization of quasi-stellar radio sources at 3.71 and 11.1 centimeters*
- Watson, A. M., Coil, A. L., Shepherd, D. S., Hofner, P., & Churchwell, E. 1997, *ApJ* **487**, 818  
*Direct Observations of the Ionizing Star in the Ultracompact HII Region G29.96-0.02: A Strong Constraint on the Stellar Birth Line for Massive Stars*
- Weferling, B., Reichertz, L. A., Schmid-Burgk, J., & Kreysa, E. 2002, *A&A* **383**, 1088  
*Principles of the data reduction and first results of the fastscanning method for (sub)millimeter astronomy*
- Wegner, W. 1994, *MNRAS* **270**, 229  
*Intrinsic Colour Indices of OB Supergiants Giants and Dwarfs in the UBVRIJHKLM System*
- Weingartner, J. C., & Draine, B. T. 2001, *ApJ* **548**, 296  
*Dust Grain-Size Distributions and Extinction in the Milky Way, Large Magellanic Cloud, and Small Magellanic Cloud*
- Weintraub, D. A., & Kastner, J. 1993, *ApJ* **411**, 767  
*The exciting young stellar object for the molecular outflow at the core of L1287*
- Wolf, S., Henning, Th., & Stecklum, B. 1999, *A&A* **349**, 839  
*Multidimensional self-consistent radiative transfer simulations based on the Monte-Carlo method*
- Wood, D. O. S., & Churchwell, E. 1989a, *ApJS* **69**, 831  
*The morphologies and physical properties of ultracompact HII regions*
- Wood, D. O. S., & Churchwell, E. 1989b, *ApJ* **340**, 265  
*Massive stars embedded in molecular clouds – Their population and distribution in the Galaxy*
- Yamashita, T., Sato, S., Nagata, T., et al. 1987, *A&A* **177**, 258  
*Polarimetric mapping of a new infrared reflection nebula GGD 27 IRS*

- Yamashita, T., Suzuki, H., Kaifu, N., et al. 1989, ApJ **347**, 894  
*A new CO bipolar flow and dense disk system associated with the infrared reflection nebula GGD 27 IRS*
- Yamashita, T., Sato, S., Kaifu, N., & Hayashi, S. S. 1990, ApJ **365**, 615  
*The density structure of the protostellar disk: A power-law distribution of the dust around GGD 27 IRS*
- Yamashita, T., Murata, Y., Kawabe, R., Kaifu, N., & Tamura, M. 1991, ApJ **373**, 560  
*The dense inner part of the protostellar disk: protostar candidates in GGD 27 IRS*
- Yao, Y., Hirata, N., Ishii, M., et al. 1997, ApJ **490**, 281  
*Near-Infrared Polarimetric Study of Monoceros R2 IRS*
- Yao, Y., Ishii, M., Nagata, T., Nakaya, H., & Sato, S. 2000, ApJ **542**, 392  
*Unveiling Deeply Embedded Sources by Near-Infrared Polarimetric Imaging*
- Yorke, H. W. 1980, A&A **85**, 215  
*The Evolution of Protostellar Envelopes of Masses  $3 M_{\odot}$  and  $10 M_{\odot}$*
- Yorke, H. W., & Shustov, B. M. 1981, A&A **98**, 125  
*The spectral appearance of dusty protostellar envelopes*
- Yorke, H. W. 1986, ARA&A **24**, 49  
*The dynamical evolution of HII regions - Recent theoretical developments*
- Yorke, H. W., & Bodenheimer, P. 1999, ApJ **525**, 330  
*The Formation of Protostellar Disks. III. The Influence of Gravitationally Induced Angular Momentum Transport on Disk Structure and Appearance*
- Yorke, H. W., & Sonnhalter, C. 2002, ApJ **569**, 846  
*On the Formation of Massive Stars*
- Yorke, H. W. 2004, in: Star Formation at High Angular Resolution, M. G. Burton, R. Jayawardhana, & T. L. Bourke (eds.), IAU Symp. **221**, 141  
*The formation of massive stars by accretion*
- Zhang, Q., Ho, P. T. P., & Ohashi, N. 1998, ApJ **494**, 636  
*Dynamical Collapse in W51 Massive Cores: CS (3–2) and CH<sub>3</sub>CN Observations*
- Zinchenko, I. 2005, private communication
- Zinnecker, H., & Mathieu, R. 2000, The Formation of Binary Stars, Proceedings of IAU Symposium 200, H. Zinnecker & R. Mathieu (eds.), published by Astronomical Society of the Pacific

This research has made extensive use of the *SIMBAD* database, the *ALADIN* interactive sky atlas (Bonnarel et al. 2000), and the *VIZIER* catalogues (Ochsenbein et al. 2000), all provided by *CDS*, Strasbourg, France. Furthermore, we used NASA's Astrophysics Data System (ADS) for accessing most of the literature listed in the references.

This research made use of data products from the Midcourse Space Experiment (*MSX*) and of the NASA/IPAC Infrared Science Archive, which is operated by the Jet Propulsion Laboratory, California Institute of Technology, under contract with the National Aeronautics and Space Administration.

## Appendix A

### **NIR Astrometry for G9.62+0.19**

Special care was taken to establish an accurate astrometry for the *VLT* NIR data. Two approaches were used:

First, we extracted an I-band image from the *ALADIN* interactive sky atlas (Bonnarel et al. 2000) that contained the region of interest. The image we used had been constructed by digital scanning of a *SERC-I* photo plate, using the *MAMA/CAI* scanning facility (Guibert 1992). Such an image has – in comparison to *DSS1* and *DSS2* images – a finer pixel scale ( $0''.67/\text{px}$ ). Within this ( $11''.5 \times 11''.5$ ) subimage we found three useful stars also included in the *ACT* reference catalogue (Urban et al. 1997). We calibrated the I-band image with help of these *ACT* stars and used this image now as an astrometric reference to adjust the *VLT*- $K_s$  image. This could be done straightforward since many stars in the central region of the I-band image were also present in the *VLT* image.

The second way was more direct without an intermediate step. By applying the *ALADIN* tool we identified more than ten stars in our *VLT* image also included in the *USNO-A2.0* catalogue (Monet et al. 1998)<sup>1</sup>. We then used these catalogued stellar positions to directly calibrate the *VLT* image. Nevertheless, one has to be careful when choosing these stars. Some objects which, due to the lower resolution, seem to be star-like on the optical photo plate images and are therefore included in star catalogues like *USNO-A2.0*, turn out to be stars with associated nebulosity or clusters of stars when imaged with high resolution. Hence, we controlled our selection of stars by examining publicly available digitised images of the region. Only positions which appeared to be clearly associated with one single object in both, the optical and the NIR images, have been used for the calibration.

Both methods gave almost identical results. A comparison of several object positions resulted in deviations of  $\leq 0''.25$  between the two methods.

After applying these astrometrical calibrations the “red” compact object F1 is still 1.7 arcsec away from the position of radio component F – a discrepancy which we find to be significant regarding the high resolution of the data. Furthermore, we should mention that

---

<sup>1</sup> We used the *USNO-A2.0* catalogue because it is more or less directly tied to the *HIPPARCOS* reference frame. In the meantime, we also checked the astrometry for the G9.62+0.19 region according to the *2MASS All Sky Survey* (Cutri et al. 2003). An offset of around 0.3 arcseconds seems to exist between both catalogues for G9.62+0.19. We can and will not evaluate here which catalogue is more accurate. We just mention that the *2MASS* astrometry places our object F4 even closer ( $0''.15$ ) to the peak of the *HMC* molecular line emission (see Fig. 3.5)



the positional difference between our astrometry and the one in Testi et al. (1998) is obvious, but not large. On the other hand, there is a substantial astrometric disagreement between our newly derived positions and the ones given in Walsh et al. (1999) for their K band image of the G9.62+0.19 region.

Persi et al. (2003) use for their investigations of G9.62+0.19 the (preliminary) first *DENIS* point source catalogue (Epchtein et al. 1999) as astrometric reference. This choice is problematic since this catalogue itself uses the old (pre-*HIPPARCOS*) Guide Star Catalog GSC 1 (Lasker et al. 1990) for calibration. As a test, we looked for stars in our VLT images which are included in USNO2 as well as in *DENIS*. Simple marking of the coordinates given in the catalogues reveals that all *DENIS* positions seem to be systematically shifted  $\approx 2.5$  arcsec to the north-northwest. From that spot check we cannot assert a global problem for the astrometry of the *DENIS* catalogue. But it is obvious that the particular stripe of the *DENIS* release data which contains the G9.62+0.19 region suffers from an unprecise astrometry and should not be used for calibrating high-resolution data.

## Appendix B

# **Correct position of the compact MIR source in G9.62+0.19–F**

De Buizer et al. (2000) had first reported on this MIR feature. They used previous 23 GHz continuum data (Cesaroni et al. 1994) to correlate their MIR data. These radio data did not yet reveal the presence of the weak 1.3 cm radio emission arising from component F, but only showed the peak belonging to component D (cf. the overlaid contours in Fig. 3.6). They then assumed that this radio continuum peak for D should be coincident with the MIR peak. However, more recent investigations could already show that the compact mid-IR source does not coincide with radio component D (see Stecklum et al. 2002a, Persi et al. 2003). Both groups placed the emission within the HMC region G9.62+0.19–F. The astrometry was mainly based on the comparison of centroids of the extended emission (component B) from the science data and from the (coarser) 12.1  $\mu\text{m}$  *MSX* images showing the same field. Still, the error of such a method is around 2'' and does not allow to decide to which of the objects in the HMC region the MIR compact emission is related. Finally, De Buizer et al. (2003) presented new 11.7  $\mu\text{m}$  data that seem to show that the MIR emission is neither associated with component D nor with component F but is displaced from both by roughly 2 – 3 arcseconds. Their new astrometry is based on a correlation between MIR features and a 3.5 cm ATCA interferometric radio map taken from Phillips et al. (1998).

In an attempt to clarify the situation, we observed G9.62+0.19 at 8.7  $\mu\text{m}$  (N1 filter), using *TIMMI2*. The smaller wavelength (compared to 11.7  $\mu\text{m}$ ) and the larger field of view (compared to *SpectroCam-10*) should facilitate the search for compact reference objects in the field. The result is shown in Fig. 3.7, where we overlay the *TIMMI2* data on our NIR data. In the north, we found a bright star, that is also visible in the  $K_s$ ,  $L'$ , and M band, suitable for attaching the *TIMMI2* astrometry to the VLT astrometry. The small rotation misalignment of the *TIMMI2* chip with respect to the sky coordinate system could be estimated independently, because during the observing run we also observed other regions that showed several sources with 2MASS counterparts in the field of view (Grady et al. 2004). The positional uncertainty is around 0.4 arcsecs in RA and DEC (i.e., 2 pixels in each direction). We cannot confirm the astrometric result of De Buizer et al. (2003). We find, that the compact MIR emission is indeed located in the direct vicinity of the HMC. Our astrom-

etry speaks against a straight identification of the compact MIR emission with object F1, but rather suggests that the peak of the MIR emission is more towards object F4. In comparison to the  $11.7\ \mu\text{m}$  data, the MIR emission blob is not pointlike. We therefore deconvolved this part of the image with the standard star HD 169916 acting as PSF reference (this star is used as unresolved calibration star even for *MIDI* interferometric measurements). The result (cf. in Fig. 3.5) is an elongated structure with a similar position angle ( $55^\circ \pm 6^\circ$ ) as the F1–F4 object pair ( $51.5^\circ \pm 2^\circ$ ). This further strengthens our diagnosis that also at  $8.7\ \mu\text{m}$  we see the objects F4 and F1 that seem to merge to one object due to the lower spatial resolution of the *TIMMI2* data. The relative strengths of the contributions of both objects is governed by the very different spectral energy distributions of F1 and F4 (see Fig. 3.10).

We should finally mention that one fraction of the astrometrical disagreement between De Buizer et al. (2003) and our result disappears when agreeing on the exact radio reference position for the HMC! We note that they use the J2000 position  $18^{\text{h}}06^{\text{m}}14^{\text{s}}.82$  (RA),  $-20^\circ31'38''.4$  (DEC) as HMC reference position (cf. their Table 1 and their Fig. 2). But this corresponds neither to the peak of the  $\text{NH}_3(5,5)$  emission nor to the position of the faint 3.6 cm continuum of the HMC (see our Table 3.1 or consult the respective references therein). The difference between the 3.6 cm peak position, which we use as HMC position throughout this thesis and which is the most accurate position for this hot core to date, and the De Buizer values is ca. 0.85 arcsec in RA and ca. 1.0 arcsec in DEC, the total displacement is hence around 1.3 arcsec. Taking this into account the disagreement between De Buizer’s and our estimation still does not vanish completely, but has shrunk considerably.

## Appendix C

### **MIR image restoration**

If one has, due to the necessary chopping and nodding in the MIR, the positive and negative beams in the final image, the usual way to treat the data is to perform a kind of shift and add. But in principle, it is possible to deconvolve the image using a matrix multiplication procedure. We refer to Bertero et al. (2000; hereafter BBR) for details of this so-called projected Landweber method. The basic idea is that within the final multi-beam image several points at different sky positions contribute to the signal contained in one pixel of the detector array. Assuming that the chopping and nodding throws are colinear along the vertical orientation of the detector chip one can describe the multi-beam image  $\mathbf{g}$  as result of a multiplication of the actually mapped larger rectangular field  $\mathbf{f}$  with a simple imaging matrix  $\mathbf{A}$ , populated just with natural numbers (see BBR):

$$\mathbf{g} = \mathbf{A} \mathbf{f} . \quad (3.1)$$

The projected Landweber method deals with this inversion problem in order to restore the original field  $\mathbf{f}$ . The following iterative ansatz is used:

$$\mathbf{f}^{(k+1)} = \mathbf{P}_+ \left[ \mathbf{f}^{(k)} + \tau \left( \mathbf{A}^T \mathbf{g} - \mathbf{A}^T \mathbf{A} \mathbf{f}^{(k)} \right) \right] . \quad (3.2)$$

Hereby  $\mathbf{P}_+$  is the projection onto the positive subset of iterative solutions,  $\mathbf{A}^T$  means the transposed matrix, and  $\tau$  is a relaxation parameter which is related to the largest singular value of the matrix  $\mathbf{A}$ . As starting point  $\mathbf{f}^{(0)} = \mathbf{0}$  is chosen.

Applying this method, some effects can influence the quality of the restoration. This contains the appearance of ghost images of the restored objects at distances being multiples of the chopping/ nodding throws. Such artefacts are inherent in the method itself and can be understood mathematically. The BBR article deals with techniques to reduce/remove several kinds of artifacts that may appear.

Since we used for our observations a chop-nod pattern different from the one used in the BBR approach (chopping perpendicular to nodding vs. chopping parallel to nodding), we had to adapt the original version of their program. Due to the loss of colinearity the problem is now really a two-dimensional one; thus, one imaging matrix alone is not sufficient. The new imaging equation reads now with two imaging matrices  $\mathbf{A}$  and  $\mathbf{B}$ :

$$\mathbf{g} = \mathbf{A} \mathbf{f} \mathbf{B} . \quad (3.3)$$

The iteration equation evolves to the new key formula:

$$f^{(k+1)} = P_+ \left[ f^{(k)} + \tau \left( A^T g B^T - A^T A f^{(k)} B B^T \right) \right]. \quad (3.4)$$

In principle, there is good reason to apply such a kind of restoration method. First, one can easily disentangle the regions in the multi-beam image where positive and negative components overlap when imaging crowded fields. In this regard, our approach has already proven to be effective for the case of TIMMI2 imaging of NGC2264 IRS1 (Schreyer et al. 2003). Second, one gains a larger field of view, because the reconstructed image covers the areas of both, the on-beams and the off-beams. This is of course an advantage when one tries to map extended objects with the medium-sized (not to say small) MIR detector arrays available nowadays. In addition, within a larger field it might also be easier to find other objects that could serve as astrometric reference points.

## Appendix D

# **Maser Cross Calibration for VLA data**

In the following, we describe in more detail the procedure we used for the maser cross calibration of the VLA 7-mm data for GGD 27 (see Sect. 4.2). Due to the lack of space we cannot further explain the basic terminology here. However, everybody working with VLA data and with the standard interferometry reduction package *AIPS* will certainly recognise and understand the typical jargon.

As a general setup, the 4 IF spectral line mode is used (see also VLA observational status summary at <http://www.vla.nrao.edu/astro/guides/vlas/current/> for details). This allows to observe two different frequencies (within a 500 MHz range) at two different bandwidths, simultaneously.

The data taken with maser cross-calibration consist of four files:

- (1) narrow band CH0: average of the inner 75% of the channels of file (2)
- (2) narrow band spectral line: centred on the maser frequency,  
e.g., 63 channels  $\times$  48.8 kHz
- (3) wide band CH0: average of the inner 75% of the channels of file (4)
- (4) wide band spectral line: for the quasi-continuum, shifted from the maser frequency,  
e.g., 7 channels  $\times$  3.125 MHz

If the VLA observations are set up in spectral line mode, the CH0 data files (1) and (3) are being produced automatically by the VLA online data system.

The algorithm works as follows:

1. Begin with the normal calibration of file (1) using the high frequency recipe for VLA data reduction (see <http://www.vla.nrao.edu/astro/guides/highfreq/>), taking into account potential decorrelation of the flux calibrator and the flux calibrator structure. (For extended array configurations, probably a source model based on CLEAN components has to be used.) This should result in a calibration table [CL3]<sub>n</sub> which is subsequently copied to the narrow band line data (2). Remember that the secondary calibrator observations are widely spaced in time (45 – 60 min), so unless the weather was excellent and/or the maser was very strong, the maser will not be detected at this stage.
2. Image the spectral line data (2). (A band pass calibration is usually not necessary due

to narrow band). Do this by applying  $[CL3]_n$  from the narrow band calibration above. This will remove electronic phase and amplitude differences in first order. Identify the channel with strong maser emission suitable for selfcalibration. If the maser can be imaged at this stage we can measure its position via normal phase referencing, which is important when controlling the absolute astrometry in the following stages after the selfcalibration. If it is not possible to image the maser, a position has to be assumed based on other/previous observations. (Hence, it is advisable to do a short independent fast-switching run to check the maser astrometry.)

3. Carry out the selfcalibration on the strongest maser channel. This will produce a number of solution tables (e.g.,  $[SN3]_n - [SN6]_n$ ) containing solutions of both phase only and phase & amplitude, with solution intervals as short as possible to reliably track the variability of the atmosphere (probably 10 seconds).
4. For the wide band CH 0 data (3), carry out the normal calibration using the high frequency recipe as above under 1.). Copy the resulting calibration table  $[CL3]_w$  (different from the one mentioned under item 1.) to the wide band line data (4).
5. Calculate a band pass correction (table  $[BP1]_w$ ) for the line data and decide by looking at the calibrator data which channels are good (in particular, check the band pass edges).
6. SPLIT the wide-band line data applying  $[CL3]_w$  (external calibration based on wide band CH 0), and  $[BP1]_w$ . Let the output file name be: `wbline.split`. This is essentially applying the regular calibration with phase and amplitude correction derived from the secondary calibrator (i.e., a strong quasar observed approx. every 45 minutes). This will correct for phase and amplitude changes due to the electronics.
7. Copy  $[SN3]_n$  from the maser selfcalibration process (item 3.) to `wbline.split`. This SN table probably contains only phase corrections and will give the largest improvement, as it hopefully tracks the atmospheric phase at intervals of 10 seconds.
8. Run SPLIT again, using as input `wbline.split` and apply  $[SN3]_n$ ; let the output file name be: `wbline.split-3`.
9. Image the resulting `wbline.split-3` file and see if it works....
10. To apply further iteration of the maser selfcalibration, now copy  $[SN4]_n$  to `wbline.split-3` and SPLIT again: The result is `wbline.split-4` that can again be imaged.
11. Finally, when all SN tables from the maser selfcalibration have been applied, run AVSPC to sum up all the 7 channels in the `wbline.split-x` file. This will form the final 1-channel uv database, that can be imaged to give the final result.

We mention again, that we used the spectral line mode as the general setup for the cross calibration measurements. In the case of VLA data, the performance is still limited by the abilities of the VLA correlator. The bandwidth of the two broadband IFs is limited to 25 MHz each which is, generally spoken, rather small. Also in comparison to the continuum mode where in principle  $4 \times 50$  MHz are available. This situation will change with the introduction of the expanded VLA (eVLA) and the new more flexible correlator.

## Appendix E

### **Used Acronyms**

In this short list we collect some acronyms and abbreviations used in this thesis.

---

---

Acronym	Meaning
BIMA	Berkeley–Illinois–Maryland Array
GGD	Catalogue of Herbig–Haro objects by Gyulbudaghian et al. (1978)
FIR	Far–Infrared
HMC	Hot Molecular Core
HMPO	High–Mass Protostellar Object
HMSC	High–Mass Starless Core
IDL	Interactive Data Language
ISO	Infrared Space Observatory
IRAS	Infrared Astronomical Satellite (and the respective source catalogue)
IRDC	Infrared Dark Cloud
JCMT	James–Clerk–Maxwell Telescope
KAO	Kuiper Airborne Observatory
MIDAS	Munich Image Data Analysis System
MIR	Mid–Infrared
Mol	Catalogue of HMPO candidates by Molinari et al. (1996)
MSX	Midcourse Space Experiment
mYSO	massive Young Stellar Object
NIR	Near–Infrared
OVRO	Owens Valley Radio Observatory
SED	Spectral Energy Distribution
UCH <sub>II</sub> R	Ultracompact H <sub>II</sub> Region
VLA	Very Large Array
VLT	Very Large Telescope
YSO	Young Stellar Object
ZAMS	Zero Age Main Sequence

---



# Acknowledgements

After the thesis is done, the acknowledgements are the last piece of text that is written, traditionally under pressure of time (at least in my case). What a pity! But I hope I can make my point.

I am very thankful to Prof. Thomas Henning for his supervision and advice for this thesis, and for the opportunity to carry on with my studies at the MPIA Heidelberg. I am most grateful that he had so much patience with me, and that his soft pressure finally pushed me to come to an end and finish this thesis.

I am deeply grateful to Dr. Bringfried Stecklum who started it all by proposing to me that I should come to the Tautenburg Observatory. I became immediately infected with the high-mass star formation virus in these early days. I learned all these little *IDL* tricks from him you need to get around. Mr. Stecklum had applied for the DFG grants that gave me the opportunity to explore the grandeur of this topic and to travel around the world for observations and fancy conferences. He is a real “black belt observer” (E. Churchwell), and I hope I have earned my first belt over the years. It’s still light-coloured, but well ...

It’s a pleasure to thank all the people from Tautenburg Observatory for the very nice and easy-going atmosphere in this institute. It has been a great experience, and I enjoyed it very much during the three and a half years I was there. Especially, I want to thank Prof. Artie Hatzes that he agreed to act as the third referee for this thesis. Thanks also to my Tautenburg office mate Dr. Sylvio Klose. I think we were a pretty good office team. And while I was trying to understand how high-mass stars form, he was busy around the clock to explore the gamma-ray burst farewell scream of high-mass stars. Thanks for the good time and many chats and advice, and the *SIMBA* observations in July 2003.

The visit of Prof. Peter Hofner in Jena in autumn 2000 was a turning point in my life since he announced the opportunity for a student to work with him in Puerto Rico. This student turned out to be me! So for one year I changed from the silent river Saale to the Carribean Sea. I am very thankful to him for this year and for introducing me to the wonders of radio interferometry and to the small circle of maser cross-calibrators.

In Puerto Rico I found already at the first day a very good friend in Esteban Araya. Your help in these days can not enough be praised. Those were the days when your old car named Judas (nomen est omen) was still alive and we escaped the Moloch of San Juan from time to time to visit the Arecibo Observatory. Muchissimas gracias for all this!

Thanks also to the bunch of physics students (Emilio, Rafael, Xavier, Francisco, Wanda ...) for the warm welcome to the strange gringo from Germany.

Many thanks to Ilaria Pascucci and Dániel Apai for good cooperation and especially for convincing me that a Jeep trip through the deserts around Alice Springs is worthwhile. These days and star-gazing nights in Australia were just great.

After my time in Tautenburg ended, I was following the leader to Heidelberg where I immediately found good people and new friends. Thanks to all the folks from the coffee/tea round

for chatting and silly gossip. Special thanks to Santa Nadine for good conversation and for the word “procrestinating” and to Elena (Dr. Puga) for always remembering me that I should stop doing other things and finally should focus on the thesis. Right!

I think it was good fortune for me that Sascha P. Quanz turned out to be my new office mate. Thanks for all the laughter, the revival of guitar playing, and for giving me the impression that I indeed could have some astronomical knowledge that I can pass on to the next generation of PhD students.

Thanks also to Dr. Sebastian Wolf and Dr. Jeroen Bouwman from MPIA for chatting about science and beyond and for showing me that the life continues after the PhD. Thank you for all the advice about radiative transfer, dust grains etc.

I want to thank my dear friends Katrin, Maria, Claudia and René from Jena for setting me straight from time to time and for being the point of contact to the non–astronomical life. (Yes, there is a life outside astronomy!) You are the friends for life. Enough said. Anything further I will tell you personally.

And, dear MoMorla, after this thesis, I definitely have to read the book *Momo* to learn about time management. Or perhaps I will learn that time as a concept is totally overrated, and the pressure of time is just an invention of the nasty Grey Men.

Last but not least, möchte ich meinen Eltern danken, die mich all die Jahre bei meinem Vorhaben unterstützt haben, Physik zu studieren und dann auch noch das Mammut–Projekt Promotion in Angriff zu nehmen. Ohne Euer Verständnis und das immerwährende Mut–Zusprechen wäre diese Arbeit vielleicht nicht zustande gekommen.

Salvete!

# **TABELLARISCHER LEBENS LAUF**

Hendrik Linz

## **Persönliche Angaben**

Name: HENDRIK LINZ  
Geburtsdatum: 10. JANUAR 1975  
Geburtsort: SUHL/THÜRINGEN  
Staatsbürgerschaft: DEUTSCH  
Familienstatus: LEDIG

## **Ausbildung**

08/2001 – 07/2002: Forschungsjahr an der University of Puerto Rico (USA),  
Betreuer: Prof. Dr. P. Hofner

2000 – 2005: Promotionsstudent an der FSU Jena,  
Promotionsthema: “Der stellare Gehalt heißer  
Molekülwolkenkerne”, Betreuer: Dr. B. Stecklum (TLS  
Tautenburg), Prof. Dr. Th. Henning (FSU Jena und MPIA  
Heidelberg)

11/1999: Abschluß des Studiums als Diplom-Physiker,  
Gesamtprädikat “SEHR GUT”

1998 – 1999: Erstellen der Diplomarbeit “Meßverfahren der abbildenden Po-  
larimetrie bei 0,7  $\mu\text{m}$  und 10  $\mu\text{m}$  Wellenlänge” am Astro-  
physikalischen Institut der FSU Jena,  
Betreuer: Dr. H.-G. Reimann, Prof. Dr. W. Pfau

1994 – 1999: Physik- und Astronomie-Studium an der Friedrich-Schiller-  
Universität (FSU) Jena

1990 – 1993: Besuch des 1. Staatlichen Gymnasiums Suhl, Erlangung der all-  
gemeinen Hochschulreife (“Abitur”)

1981 – 1990: Besuch der 7. Polytechnischen Oberschule Suhl, Grund- und Mit-  
telstufe

Sprachen: deutsch (Muttersprache), englisch (fließend), russisch (Grund-  
kenntnisse)



# Ehrenwörtliche Erklärungen

Ich habe die geltende Promotionsordnung der Physikalisch–Astronomischen Fakultät der Friedrich–Schiller–Universität Jena zur Kenntnis genommen.

Die eingereichte Dissertationsschrift wurde von mir selbst verfaßt. Alle von mir benutzen Quellen sind im Text zitiert und in einem ausführlichen Literaturverzeichnis dargelegt.

Bezüglich der Datenauswahl und –auswertung ist folgendes zu erwähnen:

1. Die in Abschnitt 2.2.5 erwähnten Millimeter–Beobachtungen mit *SIMBA* am *SEST* in Chile wurden (nach meiner eingehenden Vorbereitung) von Dr. S. Klose (TLS Tautenburg) durchgeführt.
2. Die Angleichung physikalischer Parameter an das N–Band–Spektrum des Objektes GGD 27–ILL (Abschnitt 4.1.3) basiert auf einem Fit–Programm, welches von Dr. B. Stecklum (TLS Tautenburg), einem der Betreuer dieser Promotionsarbeit, erstellt wurde.
3. Die *VLA*–Beobachtungen aus Abschnitt 4.2 entstanden im Rahmen einer internationalen Kooperation, wobei ich als Projektleiter agierte. Die Beobachtungen fanden an insgesamt zwei Tagen statt. Während ich zusammen mit Dr. P. Hofner (NMT Socorro, USA) die Daten des zweiten Tages analysierte, wurden die Daten des ersten Tages von Dr. L. Rodríguez and Dr. S. Kurtz (beide UNAM, Mexico) bearbeitet. Schließlich wurden beide Datensätze von mir zusammengefügt und weitergehend analysiert.
4. Das 1D–Strahlungstransportmodell für GGD 27–ILL unter Verwendung des Programms *MODUST* (Abschnitt 4.4.1) wurde in Zusammenarbeit mit Dr. J. Bouwman (MPIA Heidelberg), einem der Mitentwickler dieses Programms, erarbeitet.

Die Hilfe eines professionellen Promotionsberaters wurde nicht in Anspruch genommen. Andere Personen haben weder mittelbar noch unmittelbar von mir geldwerte Leistungen erhalten, die im Zusammenhang mit dem Inhalt der vorgelegten Dissertation stehen.

Diese Dissertation ist im Vorfeld nicht bereits als Prüfungsarbeit für eine staatliche oder andere wissenschaftliche Prüfung eingereicht worden.

Die vorgelegte Arbeit ist meine erste Dissertationsschrift. Von mir sind bisher noch keine anderen Dissertationen jeglichen Inhaltes bei dieser oder einer anderen Hochschule eingereicht worden.

Ich versichere ehrenwörtlich, daß ich nach bestem Wissen die reine Wahrheit gesagt habe und nichts verschwiegen habe.

Jena, den 09. Mai 2005

*Hendrik Linz*